SYNTHESIS AND CHARACTERIZATION OF LOADED/UNLOADED MESOPOROUS WO_3 BASED SEMICONDUCTOR NANOCOMPOSITES BY NANOCASTING ON "HARD TEMPLATE" AND "SOFT TEMPLATE" SUPPORTS

BY

OLOORE LUQMAN EKUNDAYO

A Thesis Presented to the
DEANSHIP OF GRADUATE STUDIES

KING FAHD UNIVERSITY OF PETROLEUM & MINERALS
DHAHRAN, SAUDI ARABIA

In Partial Fulfillment of the
Requirements for the Degree of

MASTER OF SCIENCE

In

PHYSICS

APRIL, 2016

KING FAHD UNIVERSITY OF PETROLEUM & MINERALS
DHAHRAN- 31261, SAUDI ARABIA
DEANSHIP OF GRADUATE STUDIES

This thesis, written by **OLOORE LUQMAN EKUNDAYO** under the direction of his thesis advisor and approved by his thesis committee, has been presented and accepted by the Dean of Graduate Studies, in partial fulfillment of the requirements for the degree of **MASTER OF SCIENCE IN PHYSICS**

Thesis Committee

M. A. Gondal

Dr. Mohammad A. Gondal
(Advisor)

Dr. Zain H. Yamani
(Member)

Haider

Dr. Muhammad B. Haider
(Member)

Dr. Abdullah A. Al-Sunaidi
Department Chairman

Dr. Salam A. Zummo
Dean of Graduate Studies

7/4/16

Date

Dedication

Dedicated to my wife *Sai'dah Abimbola Alake*

ACKNOWLEDGMENTS

I give thanks, praise and adoration to Allah for the gift of life and his protection over me since the creation of my soul. I pray he continue to guide me to the right path and make my affairs before and after death easy one.

I am grateful to my thesis advisor Dr. (distinguished prof.) Mohammed Ashraf Gondal for his guidance as well as moral, academic and fatherly support, during the research process. I express my appreciation to the committee members, Dr. Zain Hassan Abdallah Yamani, for his time and teachings towards successful and presentable thesis work, and Dr. Muhammad Baseer Haider for his words of encouragement during the process.

I express my sincere gratitude to the entire and faculty staff members of the physics department for their direct or indirect support, especially those who have taught me some courses like: Dr. M. M. Faiz, Dr. F. Z. Khiari, Dr. S. Marzoug, Dr. Z. H. Yamani, Dr. T. A. Al-Aithan, Dr. H. Bahlouli and Dr. I. M. A. Nasser. Also to the former and current chairman of the department; Dr. A. Al-Jalal and Dr. A. A. Al-Sunaidi.

My appreciation of the contribution from Mr. M. Abdulkadir Dastageer and the entire members of the laser research group cannot be over-emphasized. Mr. Rashid. G. Siddique, Dr. Omair. Baig, Mr. Y. B. Habibllah, Mr. Q. Talal and Mr. S Pillai; I thank you all.

Special thanks also goes to the entire member of the Center of Research Excellence in Nanotechnology (CENT), under the directorship of Dr. Z. H. Yamani. I appreciate contribution from CENT to the successful characterization of the samples for this thesis work. Also, I thank CENT as well as Deanship of Scientific Research for financial aid during the course of this work.

Above all, sincere acknowledgment is due to the Kingdom of Saudi Arabia and King Fahd University of Petroleum and Minerals (KFUPM) for granting me the opportunity to pursue my Masters degree with full scholarship. I am also grateful Obafemi Awolowo University (OAU), Ile-Ife, Nigeria and Department of physics and engineering physics, OAU for the study leave. I also acknowledge contribution of the Nigeria community in the Kingdom Saudi Arabia for making me fill at home.

I am always grateful to my parents and siblings for their support and care in any form from infant till date. To my wife (Saidat Alake), son (Labeeb Adigun) and little sister (Nusirat Aduke), thanks for your moral support, patience and endurance while I could not be with you because of academic pursuit. I am equally grateful to my close allies, Quadri Showunmi, Maruf Showunmi, Wasiu Showunmi and entire ‘A’ Makers crew.

TABLE OF CONTENTS

LIST OF TABLES

LIST OF FIGURES

THESIS ABSTRACT

NAME:	Oloore Luqman Ekundayo
TITLE OF STUDY:	Synthesis and characterization of loaded/unloaded mesoporous WO_3 based semiconductor nanocomposite by nanocasting on “hard template” and “soft template” supports
MAJOR FIELD:	Physics
DATE OF DEGREE:	April, 2016

This thesis focused on synthesis of nanostructured metal oxide semiconductor catalysts, with enhanced photocatalytic activities for application in reduction of CO_2 *to low carbon fuels, such as methane, methanol, and formic acid. Ordered mesoporous* In_2O_3 *semiconductor nanocatalyst was synthesized with increased specific surface area, by nanocasting on SBA-15 template. Pure* WO_3 *nanomaterials as well as* In_2O_3/WO_3 *nanocomposites were also synthesized, with varied concentrations of the constituent materials, and subjected to various characteristic analyses and photocatalytic applications. Ta-doped and Nb-doped* WO_3 *nanostructures were independently synthesized by hydrothermal process with P-123 support, and* *changes in the electro-physical and chemical properties of the WO_3 nanomaterials were investigated.*

The nanostructured metal oxide semiconductors synthesized were characterized for various properties such as morphology, crystallinity, composition, porosity, optical properties and UV/visible light characteristics using appropriate characterization techniques including FE-SEM, XRD, UV-VIS absorption, XPS, N_2 adsorption-desorption and photoluminescence.

The synthesis technique employed in this work are majorly wet chemical methods like the traditional sol-gel and nanocasting techniques as well as hydrothermal synthetic method. In the traditional sol-gel method, materials were prepared directly from the precursors by precipitation without a template. Contrarily, in nanocasting, the desired nanostructured materials were synthesized on SBA-15 "hard template" to form ordered mesoporous materials with increased specific surface areas.

The photocatalytic activities of a number of the synthesized nanomaterials were investigated by applying them as photocatalysts in laser induced photoreduction of CO_2 to methanol. Quantum and CO_2 conversion efficiencies of the applied catalysts were estimated, and this confirmed the enhancement in their properties due to method of preparation, addition of composite materials or doping.

ملخص الرسالة

الاسم: **أولورى لقمان إكونديايو**

عنوان الدراسة: **توليف وتوصيف تحميل / تفريغ WO_3 منتصف مسامية أشباه الموصلات القائمة على بمركب متناهي في الصغر من قبل** صب **على " قالب الصعب " ، وتدعم " قالب لينة "**

التخصص : **فيزياء**

تاريخ التخر : **أبريل 2016**

تهدف هذه الدراسة العلمية الى تحضير وتوصيف اكاسيد المعادن شبه الموصله ذات البنية النانوية بهدف تحسين حفزها الضوئي لتستخدم في اختزال ثاني اكسيد الكربون الى هيدروكربونات مثل الميثان، الميثانول وحمض الفورميك. اكاسيد المعادن شبه الموصله ذات البنية النانوية التي تم تحضيرها، توصيفها ودراسة حفزها الضوئي في هذه الدراسة هى أكسيد الإنديوم الثلاثي، اكسيد التنجستن، مركب أكسيد الإنديوم الثلاثي واكسيد التنجستن، اكسيد التنجستن المطعم بعنصر التنتالوم وعنصر النيوبيوم.

حضرت اكاسيد المعادن شبه الموصله ذات البنية النانوية با ستخدام طرق كيميائية وبعد ذلك تم استخدام تقنيات التوصيف المناسبة لتوصيف المواد المحضرة لدراسة تركيبها البلوري، مساميتها وخواصها الضوئية.

الحفز الضوئي للمواد المحضرة تم دراستة عن طريق استخدامها لاختزال ثاني اكسيد الكربون الى ميثانول بوجود اشعة الليزر. اثبتت هذه الدراسة زيادة كفاءة المواد المحضرة لاختزال ثاني اكسيد الكربون الى ميثانول ويعزي هذا التحسن في كفاءة الاختزال الى طريقة التحضير، التركيب الكيميائي و العناصر الكيميائية المستخدمة في التطعيم.

CHAPTER 1

INTRODUCTION

1.1 Metal oxide semiconductor nanocrystals

The important roles which metal oxides semiconductor are playing in the areas of physics, material science, chemistry and the fields of technology cannot be overemphasized. They are useful in the fabrication of sensors, piezoelectric devices, microelectronic circuits, fuel cells, coatings for protection against corrosion, and as catalysts [1-10]. Limited size and high density of corner or edge surface sites of oxide nanoparticles are special features which influence unique physical and chemical properties [1, 2, 9]. The three important groups of basic properties of materials are expected to be chiefly controlled by the particle size. First of these basic properties is the structural features which are fundamentally lattice symmetry and lattice parameters. Second is the electronic properties of the oxides. Both electronic and structural properties are the main drivers of the physical and chemical properties of solids. The third group of properties is related to change in the band gap as a result of change in particle sizes or quantum confinement [11-16]. Many bulk oxides have wide band gaps and low reactivity, but decrease in the sizes of these materials changes the magnitude of the band gap [17-20]. This evidently has notable influence on the conductivity and chemical reactivity [11]. If the size of a semiconductor nanocrystal is smaller than the size of an exciton, the charge carriers become spatially confined, which raises their energy [133]. The exciton refers an electrostatically bound electron-hole pair. The exciton has a finite size within the crystal defined by the Bohr exciton diameter (a_B), which can vary from 1 nm to more than 100 nm depending on the material [133]. Therefore, the exciton size delineates the transition between the regime of bulk crystal properties and the quantum confinement regime, in which the optical and electronic properties depend on the nanocrystal size. Nanocrystals with dimensions smaller than a_B demonstrate size-dependent absorption and fluorescence spectra with discrete electronic transitions [133]. The band gap of a semiconductor may be tuned to different energy by confining its exciton, depending on the dimensionality and degree of confinement [134]. Nanocrystals confined in three dimensions, two dimensions and one dimension are referred to as quantum dots quantum wires or rods and quantum wells or disks respectively.

1.2 Photophysics of semiconductor nanocrystals

The role of the semiconductor catalysts in the photocatalytic reduction processes is to absorb photons of sufficient energy to generate pairs of charge carriers (electron-hole) to assist in the oxidation and reduction processes [27, 28]. Though economically and environmentally favorable, the photocatalytic pathway is a complex one and several factors, which hinder or aid, the process have to be considered to obtain high efficiency. A couple of these factors are discussed in the subsequent sections.

1.2.1 Band structure

Two energy bands are utilized in the photocatalytic process. Localized orbitals overlap to form the low-energy band consisting mainly of filled orbitals, which is also known as the valence band (VB), and a set of higher energy bands of mainly delocalized orbitals called the conduction band (CB), as illustrated in Figure 1.1. Unlike in metals where these two bands overlap to form a continuum of energy states for the electrons, the two bands in a semiconductor are separated by a forbidden energy region, the band gap (E_g) characterized by quantum mechanical energy [29]. Lack of the band gap in metals results in its high electrical mobility [30, 31]. Hence, band to band transition between the filled and vacant electronic states readily occurs at room temperature in metals, which consequently results in high electrical mobility and thus conductivity in response to an electric field [30]. Meanwhile, it is difficult to achieve this in semiconductors because of the bigger energy spacing between the two bands. Redistribution of the electrons using an applied electric field is considerably more difficult to achieve since there are fewer empty states (CB) close in energy to the filled states (VB). This leads to reduced electrical conductivity [30]. However, excitation of the electrons from the valence band (VB) to the conduction band (CB) can be used to induce electrical mobility. The excitation process can be carried out by illumination with photons of energy greater than the Eg. When the photogenerated electrons from the valence band are excited to the conduction band, empty states are left in the valence band. The empty states have the attributes of positively charged particles called holes [31]. The two photogenerated charge carriers can be utilized to perform photocatalytic process and other photochemical processes alike.

Semiconductors generally exhibit two kind of band gaps characterized with two different optical properties namely; direct band gaps and indirect band gaps. A material that exhibit transition between the VB and CB in which the angular momentum of the electron is preserved is a direct band gap material. Absorption of an optical photon is sufficient for these transitions. An indirect band gap transition is accompanied by change in the electron momentum, this necessitates the need for phonon, or lattice vibration [31, 32]. In short, indirect transition requires the absorption or emission of a phonon, which is less likely to occur. This results in much smaller optical absorption coefficient for an indirect transition than that of a direct transition. [31]

1.2.2 Fermi level

The Fermi level (E_F) refers to the energy level at which the probability of finding an electron in a continuum of electronic states (at 0 K) is $\frac{1}{2}$, [29, 30] as depicted in Figure 1.1. However, since the Fermi level typically lies in the band gap (reciprocal space), where electron density is quantum mechanically forbidden for semiconductors, E_F represents the generalization to Bloch electrons of the free electron Fermi sphere. The Fermi level is related to the free energy change of the semiconductor (ΔG_{SC}) as given by Equation 1.1 [29],

$$\Delta G_{SC} = -nFE_F \tag{1.1}$$

where n represents the number of electrons, F is the Faradays constant and E_F is the Fermi energy. The Fermi level is located at the midpoint of the band gap in intrinsic semiconductors [29]. Contrarily, for extrinsic semiconductor, the Fermi level is placed slightly above the VB or slightly below the CB for p-type or n-type semiconductors respectively [29, 30].

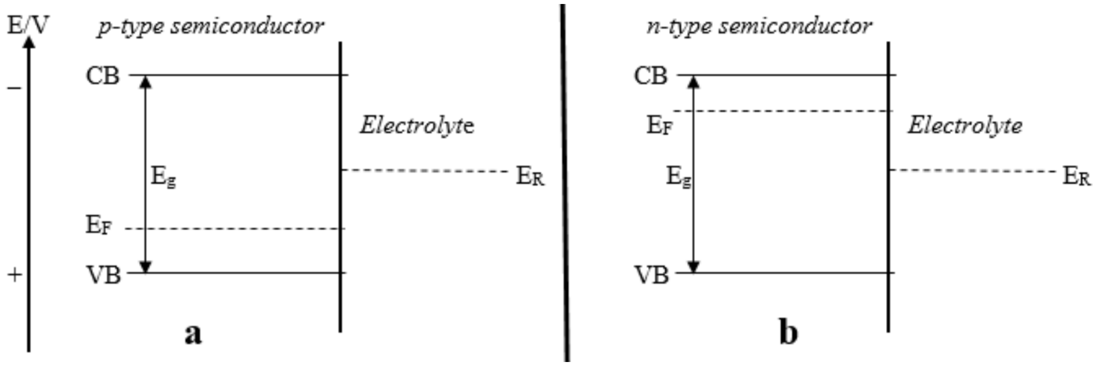

Figure 1.1: Band diagrams of p-type (a) and n-type (b) semiconductors immersed in an electrolyte with redox potential E_R before equilibrium

1.2.3 Electron-hole separation and recombination

It is highly important to stall the electron-hole recombination process so as to enable effective utilization of the photogenerated electrons and holes for CO_2 reduction process. Therefore, the electronhole pair must be separated in a manner that limits recombination, and thus promotes the transfer of the charge carriers to the redox active species at the semiconductor-electrolyte interface [29]. Electronhole pair recombination is fast in the absence of an electric field, of the order $\sim 10^{-9}$ s and it is a result of nonradiative relaxation of excited electrons to the ground state [31]. It commonly limits the electron transfer process to the semiconductor interface for subsequent oxidation or reduction reactions since it is much faster than the interfacial electron transfer processes [29, 33]. Interfacial electric fields that separate the electron-hole pair by directing the charges in opposite directions can be provided by band bending [34]. Applying an external potential to the semiconductor electrode, in the case of PEC, can further increase the band bending by controlling the Fermi level, enhancing the electron-hole pair separation, which promotes interfacial charge transfer [31].

1.2.4 Photonic efficiency

Photonic/Quantum efficiency for a semiconductor-based photochemical reaction, refers to the conversion efficiency of the incident photons to the product. Photonic efficiency is simply defined as the ratio of the number of photoelectrons that react to the number of incident photons that strike the semiconductor.

1.2.5 Band edge and effect of pH

The band edge position of a semiconductor catalyst determines the thermodynamic feasibility of a given electrochemical reaction at the interface. This is because the energies of the charge carriers remain constant at the band edge potential even if degrees of band bending and applied potentials differ. For photo-oxidation reactions, it is required for the redox potential (E_R) to be above the VB edge, whereas photoreduction reactions can proceed only when the standard reduction potential are below the CB edge. However, the band edge position can shift by -59 mV per pH, by obeying the Nernst equation [32]. This is a result of the surface hydroxylation that occurs with the continuous adsorption and desorption of H^+ and OH^- ions from the aqueous solution, which vary according to pH [32]. In the case of water splitting and CO_2 reduction reactions where the standard reduction potential involves either H^+ or OH^- ions, the Fermi level of the electrolyte can also change with pH [32]. Typically, the change in the Fermi level of the semiconductor and the change in the redox potential in solution are identical, this yields no thermodynamic advantage to changes in pH. However, the band edge positions can be maintained by coating the semiconductor with a pH-insensitive organic group [36]

1.2.6 Effect of surface states and co-catalysts

Surface states form a set of energy levels that exist exclusively at the surface of semiconductor materials and it affect the transfer of electron at the semiconductor-electrolyte interface. In this context, the ones of interest reside in the band gap. Surface states is a result of termination of the crystal lattice at the surface of the semiconducting material. There are dangling bonds from free radicals at the surface of the semiconductor, which interacts with electrolyte species, and create surface states with energy levels between the band edges [37]. Surface states often behave as loci for the photo-generated charge carriers during recombination [38, 39], as portrayed in Figure 1.2. It can also work as trapping sites for the photoelectrons or photo-holes from the conduction band or valence band, which can then be transferred to redox couples in solution with suitable potentials [40]. For example, oxygen vacancies at the surface of metal oxide semiconductors have been suggested to be the active sites for CO_2 activation, since CO_2 molecules are likely to be adsorbed at the oxygen vacancies at the surface of the semiconductor catalysts [41].

Also, introduction of co-catalysts could greatly improve the performance of a semiconductor catalyst for CO_2 reduction. The co-catalysts can help to reduce recombination and alter the selectivity of the products by acting as trapping sites for the electrons [42, 43]. Nanoparticles of metals or oxides can be added on the surface of a semiconductor catalyst to act as co-catalyst. When the Fermi level of the added metal lies above the redox potential of desired reaction and below the conduction band of the semiconductor material, the particles can act as electron reels [42].

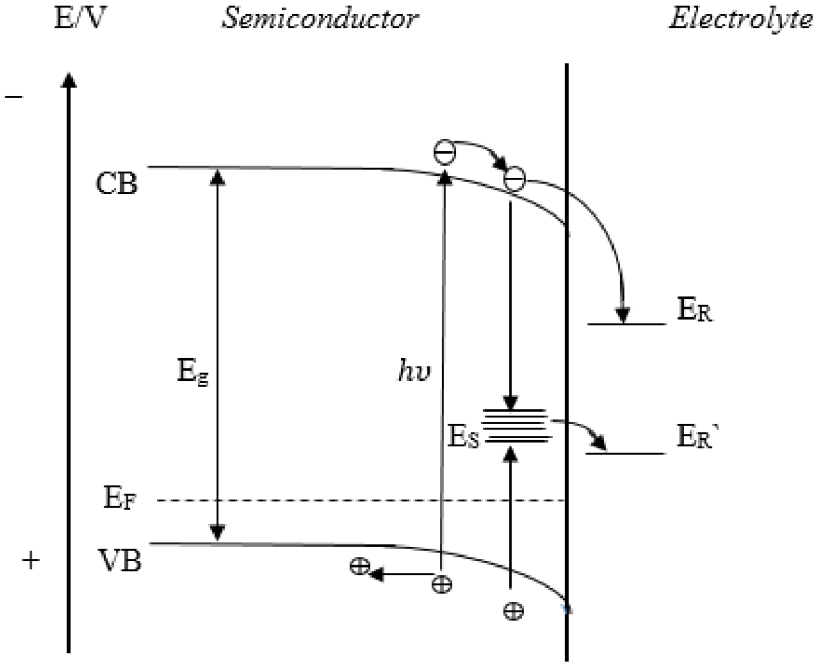

Figure 1.2: Model for recombination and charge transfer reactions involving surface states

1.2.7 Surface area to volume ratio and nanostructures of semiconductors

Increased surface area to volume ratio results in immense enhancement of the number of surface-active sites. One way of achieving this is by making the material nanostructured. Secondly, decrease in the crystal sizes minimizes the possibility of electronhole recombination because it reduces the separation between minority carrier photoformation and the charge transfer interface [44]. Thirdly, arrays of nanostructures aid scattering and secondary absorption of photons but suppresses the reflection of the incident photon, thereby effectively enhancing the light absorption coefficient of the material. One of the facile measures to engineer the band structure of materials based on quantum confinement is fabrication of the semiconductor material at the nanoscale [29]. This is due to the change in the band electronic properties of a semiconductor as its structure approaches nanoscale, which results in discrete energy levels and an increased band gap [45, 46]. For example, it was reported by Wang et al. that the conduction band of a 2.5 nm CdSe quantum dot rises by 0.7 eV, as compared to that of bulk material, when CdSe quantum dot-sensitized TiO_2 heterostructures was used for CO_2 reduction. This promotes the electron transfer from the CB of CdSe to the CB of TiO_2 [47]. The importance of enhancing surface area of the oxides has been emphasized by several reports which are solely dedicated to semiconductor photoctalysts [86, 89, 101]

Moreover, photocatalytic activities of a material can be enhanced by some exquisitely engineered nanostructures for other reasons [29, 48]. In some cases, the characteristic surface energy and surface atomic structure of the semiconductors prepared in reduced sizes also exhibited an enlarged population of a desired crystal facet possessing catalytic activity. For example, nanoplates of anatase TiO_2 possessing different ratios of {001} and {101} facets were synthesized by Yu et al. Among the series of the synthesized samples, maximum activity of CO_2 reduction to methane was observed in the one with 58% of exposed {001} facets. It was shown by the result of density function theory (DFT) that these two different facets have different CB and VB energy levels, facilitating the flow of electrons from the {001} facets to the {101} facets, while holes flow from the {101} facets to the {001} facets. Therefore, the ratio of different planes plays an important role in regulating the CO_2 reduction efficiency [48]

1.2.8 Dimensionality of nanostructured semiconductors

Different behavior may be observed in nanostructures of different dimensionalities. In the nanostructures with *zero dimension* (suspension of nanoparticles), the nanoparticles are isolated from each other. Only short distance traveling for the charge carriers on all three dimensions are allowed [49]. In *one-dimensional (1-D)* nanostructures, the dimension acts as a bypass for the majority charge carriers to migrate away from the surface, whereas the minority carriers moving in the transverse direction can easily reach the semiconductor-electrolyte interfaces [44].

This can enhance the process of charge separation. Examples of 1-D nanostructures include nanowires, nanofibers, nanotubes, nanorods and nanobelts [44]. A well-assembled 1-D nanostructure is characterized by enhanced photon absorption which results from fine scattering of incident light [51]. In *Two-dimensional (2-D)* nanomaterials, the charge carriers are less localized, unlike in 1-D systems. Example are nanosheets which can be fabricated into photoelectrodes by forming assemblies in a similar way as the 1-D nanostructures, or by depositing them as thin films [44]. *Three-dimensional (3-D)* nanostructures can be constructed from assemblies of nanostructures of smaller dimensions. It can be self-assembled or with support of a template [29]. Unlike disordered ones, unique optical effects, like slow-light effect, can be observed in 3-D ordered nanostructures [52]. Multiple scattering events, which reduces the group velocity of light, can be seen in a photonic crystal when illuminated with light. Absorption of incident photons is often enhanced by the slow light effect [44]. Photonic crystal refers to a nanostructure periodically assembled by two or more materials of different permittivity.

1.3 Application of semiconductor nanocrystals in photoreduction of CO_2

The main cause of global warming is emission of the greenhouse gases like CO_2, methane, etc. The alarming rate at which the level of CO_2 in the atmosphere is increasing has brought about need to mitigate the CO_2 emissions. Scientists, in their quest to bring down the level of CO_2 to normal, and at the same time solve the potential challenge of fuel exhaustion, have adopted the method of photoassisted catalytic reduction of the gas into substances such as carbon monoxide, acetic acid, formaldehyde and methanol. However, CO_2 is well recognized for its high stability and inertness, so it cannot be reduced under mild conditions. Thus, its conversion requires energy input or co-feeding of a high energy reactant like H_2 before it is activated.

Geological isolation and CO_2 capture followed by compression are examples of methods adopted to decrease CO_2 levels. However, these processes energetically intensive and therefore highly costly [20, 22]. This is in addition to several uncertainties in terms of long-term storage of carbon dioxide in geological formations [23].

During the process of photoreduction of CO_2 into hydrocarbon fuels, semiconductor catalysts makes use of ultraviolet (UV), visible light, or both, as the source of electron excitation, the photo-excited electrons cause CO_2 reduction using OH^- radicals from H_2O or an alkali such as NaOH on the surface of the catalyst. The product of reduction combines with OH^- to form energy-bearing products like CO, CH_4, HCOOH and CH_3OH [23-26]. Two configurations of semiconductor based systems can be adopted to achieve photoenhanced CO_2 reduction. One of the configuration is a photoelectrochemical cell (PEC). A PEC has a photoelectrode made of semiconducting material and a counter electrode. A half-cell chemical reaction takes place at the photoelectrode where charge separation is also promoted by harvesting light. In the second configuration, suspensions of semiconductor particles are used as photocatalysts in a solution with dissolved carbon IV oxide. The second configuration Figure 1.3 was adopted to test the photocatalytic activities of the synthesized oxide semiconductor materials in this work. In this, the photoreduction and photo-oxidation take place on the same semiconducting particle, but on different sites. Photocatalysts are of various sizes ranging from micro-sized particles to nanoparticles.

The photoatalytic abilities of the synthesized WO_3 nanoclusters and In_2O_3 nanocrystals and their composites in the CO_2 conversion to low carbon fuel were investigated, using water as hole scavenger and high power (266 nm or 355 nm) laser as the irradiation source. As it is generally known, numbers of reaction products like CO, methane (CH_4), formic acid, formaldehyde (HCHO) and methanol (CH_3OH), can be obtained during CO_2 photoreduction process. The pathways [27] of CO_2 photoreduction are highlighted in the Equations I-IX, with standard reduction potentials (E^{θ}_{redox}) of each reaction given relative to normal hydrogen electrode (NHE), as follows:

Activation

I $SC + h\nu \rightarrow e^- + h^+$

II $e^- + h^+ \rightarrow$ heat (electron-hole recombination, often a possibility)

Photooxidation reaction	**E^{θ}_{redox}/V vs NHE**
III $2H_2O + 4h^+ \rightarrow O_2 + 4H^+$	$+ 0.82$

Photoreduction reactions

IV	$CO_2 + 2H^+ + 2e^- \rightarrow HCOOH$	- 0.61
V	$CO_2 + 2H^+ + 2e^- \rightarrow CO + H_2O$	- 0.53
VI	$CO_2 + 4H^+ + 4e^- \rightarrow HCHO + H_2O$	- 0.48
VII	$CO_2 + 6H^+ + 6e^- \rightarrow CH_3OH + H_2O$	- 0.38
VIII	$CO_2 + 8H^+ + 8e^- \rightarrow CH_4 + 2H_2O$	- 0.24
IX	$CO_2 + 12H^+ + 12e^- \rightarrow C_2H_5OH + 3H_2O$	- 0.16

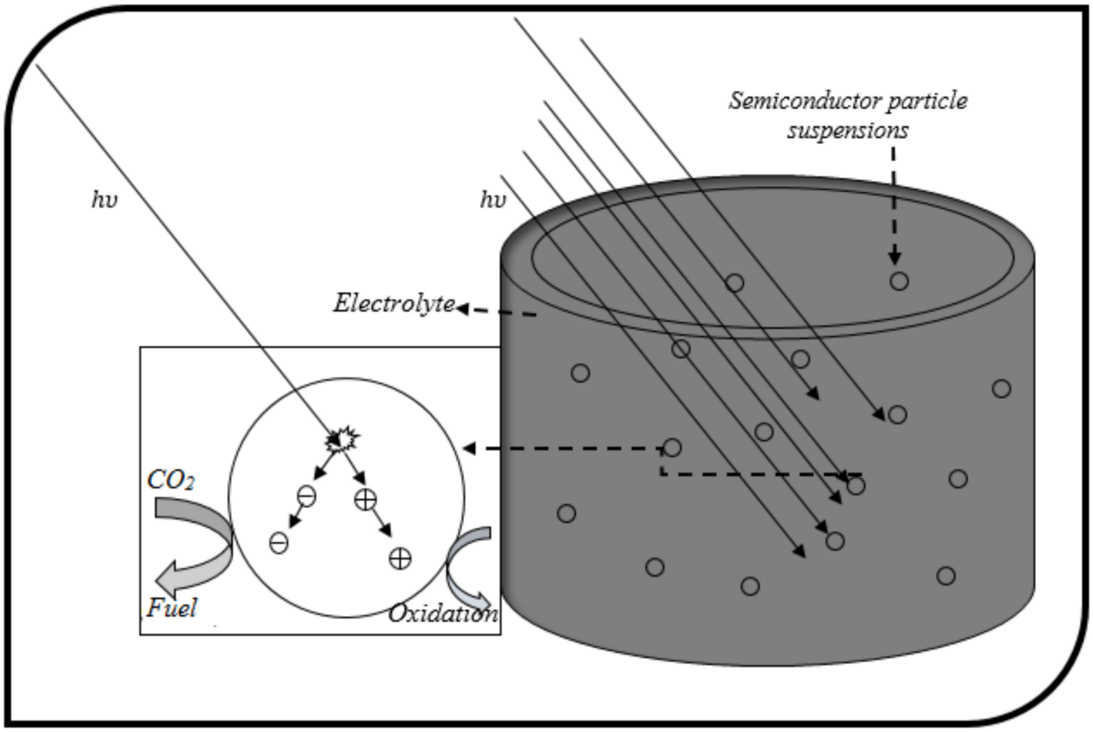

Figure 1.3: Photocatalytic particles suspended in a CO_2-containing electrolyte performing both oxidation and reduction reactions on different sites

1.4 Objectives

The major objective of this thesis work is to investigate and compare the photocatalytic properties of various as-synthesized oxide semiconductor nanocomposites. In this work the emphasis will be laid on synthesis of the nanostructured metal oxide semiconductors (doped or undoped) and improving on their various properties which make them applicable majorly in laser induced photocatalytic reduction of CO_2 to low carbon fuels. Following are the highlight of the specific objectives of the work:

- To synthesize loaded/unloaded oxide semiconductors (In_2O_3 and WO_3) by using the sol-gel methods, that is; the "soft template" support technique
- To synthesize oxide semiconductors by nanocasting technique using SBA-15 "hard template" support
- To characterize the successfully synthesized nanocomposites for morphology, crystallinity, composition, optical properties, UV-visible absorption properties and porosity
- To study the effects of dopants (metals/metal oxides) on the various properties of the synthesized material
- To study the effects of the silica support on the various properties of the oxide semiconductors synthesized on "hard template" support
- To evaluate the various characteristics, electro-physical properties and photocatalytic activities of the synthesized materials.

CHAPTER 2

LITERATURE REVIEW

Recent studies consider photocatalysis as a potential solution to the concurrent increase of energy shortage and environmental pollution. Photocatalysis has wide application in science, this includes photo-degradation of biodegradable pollutants and photocatalytic splitting of water among others [24]. Several metal oxide semiconductor catalysts have been reportedly investigated to understand their photocatalytic behaviors under UV radiation /or visible light, among them are TiO_2, ZnO, WO_3, ZrO_2, MgO and In_2O_3, and the catalysts with wide band-gaps (2.9 eV or more) are considered most suitable in terms of stability and less charge carriers recombination [53-57].

Comparatively, photocatalytic conversion has better sustainability than other methods, since there is no need for addition of extra energy. Another advantage of the method is operation under mild condition and stability of catalysts [54]. Acceptability of a catalyst to researchers depends on its stability and activity under normal operating condition. However, non-effectiveness of catalysts, selectivity and low yield constitute the barriers and difficulties facing the technology [58, 59] because of the need for highly efficient and selective catalyst to achieve effective CO_2 conversion. Another noticeable challenge is efficient design of photoreactor for production of fuel from the gas on commercial scale. There are various ways to realizing CO_2 reduction, examples of which include: thermal [60], electrochemical [61, 62] and photocatalytic [63] reduction as well as biological reduction by plants [64]. Among all these techniques, the rate at which photo-reduction is gaining attention of researchers is astonishing since it has prospect of consuming alternative forms of energy by harnessing solar energy which is naturally cheap and ecologically safe and clean, besides being abundant.

Survey of literature has shown that one of the most widely studied semiconductor metal oxides is tungsten oxide (WO_3). It has been used for various applications, most notably as photocatalyst [67-69] and gas sensor [65, 66]. It is a visible-light-driven photocatalyst with optical band gap of approximately 2.7-2.8 eV. This property allows it to absorb light in the ultraviolet to blue light (wavelength < 455 nm) ranges [70]. The smaller band gap, as compared the famous titania (TiO_2) whose band gap is around 3.0-3.2 eV, is one of the unique characteristics of WO_3 which makes it more suitable as photcatalyst and a better gas sensing material than, since it has better photoabsorption for visible-light irradiation. However, isolated WO_3 shows very weak photocatalytic activity when irradiated with visible light [14]. This called for many attempts which has been made to improve its photocatalytic activity. The work on this improvement include addition of co-catalysts, such as gold (Au), silver (Ag), palladium (Pd), platinum (Pt), which has contributed to enhancement of photodegredation ability of WO_3 [9, 11, 70, 71]. Metal oxides and metal ions as co-catalysts have also been reportedly investigated by various research groups. TiO_2, CuO, ZnO, SiO_2, Cu, Nb, Ti, etc. have been prepared as composites or dopants with WO_3. Some of these composite catalysts provide efficient photocatalysis for volatile gas decomposition [1, 36].

Pure WO_3 catalyst is characterized by lower photo-conversion efficiency when in an undoped or unloaded form; this is believed to be due to low reduction potential of its electrons because of its low conduction band edge [76]. WO_3 doped with rare earth elements are expected to exhibit high photogenerated charge separation by generating some low energy levels between the valence and conduction band of the oxides. The unoccupied f-orbit electron of the dopant act as acceptor or donor for lone pair electrons [77]; this leads to better photocatalytic activities than in the pure oxide. Example of this can be found in WO_3 doped with Eu^{3+} [77], Yb^{3+} [78] and Ce^{3+}, [79] which has reportedly contributed to the reduction of the energy of the forbidden band. Doping with transition metals, such as Mo [80] and Ti [81], has also helped improved photocatalytic activity of WO_3 by enhancing its photochemical response to light. Guest cations such as Nb^{5+} and Ta^{5+} are selected in this work because of similarity in their ionic radii and electronic structures to tungsten, this aims at making a doped oxide rather than dopant oxide cluster on our host oxide.

Indium oxide (In_2O_3) semiconductor reportedly has a wide direct band-gap ranging from 2.9 eV to 3.55 eV [27, 56, 72, 82], depending on the synthetic methods. It is a n-type semiconductor with low electrical resistivity and high optical transparency in the visible range [72, 82, 83]. In_2O_3 is described as promising semiconductor material with high sensitivity to certain gases [56, 84, 85], this application however desires In_2O_3 with large specific surface area. This is, in principle, expected to create more active sites on the material surfaces and consequently lead to change in the semiconductor surface states. Recent research activities has demonstrated that In_2O_3 nanoparticles and nanowires act as sensitive gas sensors for the likes of oxygen, CO_2, C_2H_5OH vapor and NO_2 [86], and the interest in preparation of size and shape controlled indium oxide nanoparticles continues. As seen in various research report, monodispersed spherical In_2O_3 nanoparticles and nanocubes has been synthesized with fine size control in the range 4 nm to 20 nm [83, 85-87]. These nanoparticles are characterized by formation of 2D self-assembled patterns. Different methods such as solution- and vapor-phase techniques and the use of anodic aluminum oxide membrane templates have been adopted in indium oxide synthesis processes. The former is used in making In_2O_3 octahedral nanoparticles, nanofibers, large aggregated nanostructures, etc.[56, 86, 88] while the latter is employed in fabrication of long indium oxide nanorod and nanowire arrays with length on the order of 0.1-1 μm [83, 86, 89].

For applications of the oxides as catalysts, it is a common tradition to synthesize mixed oxide materials, and silica is the most popular support and framework material among researchers, but it is not involved in the catalytic function. Therefore, it is processed with other metal oxides. However, a deliberate design of porosity and morphology of the material is often very important, this is in addition to the challenges faced in control of the homogeneity, the dispersion of the active metal species and the accessibility of the active centers, which requires deliberate positioning within the oxide matrix [42-49]. Synthesis of mesoporous-structured metal oxide semiconductors has become essential after several reports on semiconductor catalysts emphasized the importance of enhancing the specific surface area of the oxides [21-30]. Many ordered mesoporous silicas have been reportedly synthesized and characterized majorly by X-ray diffraction (XRD), Transmission electron microscopy (TEM), and N_2 adsorption-desorption during the last two decades. Mesoporous silicas include KSW-1, MCM-41, SBA-15, KIT-16, SBA-16 and FDU-12 [83]. Like P-123, these materials are employed in hard template method to prepare various mesoporous materials as a structural matrix support which is called nanocasting. A large number of microporous, mesoporous as well as macroporous crystalline oxides of transition metals (e.g Cr_2O_3, NiO, WO_3, CeO_2, MnO_3, In_2O_3, etc. [26-35]) with large active surface areas and small uniform-sized crystals have been synthesized by nanocasting technique. Successful fabrication of the porous metal oxides has established a good basis for their application in various fields.

Various techniques have been adopted to synthesize WO_3 and other metal oxide semiconductor nanoparticles, nanocrystallites or nanocomposites, including the techniques are; thermal decomposition [35], pyrolysis [52], colloidal process [53] and wet chemical process like sol-gel or nanocasting [1-4]. The wet chemical processes were usually carried out through hydrolysis of the tungstate salt precursor in acidic media. For example; Sitthisuntorn Supothina et al. [67] and K. Hayat et al. [73] have respectively synthesized WO_3 nanoparticles and nanocrystallites in their separate works by dropwise addition of nitric acid into a solution of ammonium tungstate precursors. The latter successfully used the synthesized WO_3 for laser induced photocatalytic degradation of hazardous dyes. Sitthisuntorn Supothina, in another work [66], employed similar procedure to synthesize silica-doped tungstia (SiO_2/WO_3) with ammonium paratungstate hydrate and tetraethylorthosilicate precusors. The precipitate was washed to neutral and then separated by ultrafiltration. A method of flame assisted spray pyrolysis (FASP) was adopted by Hendri Widiyandari et al. [70] to synthesize CuO/WO_3 and Pt/WO_3 nanocomposites which were reportedly efficient catalyst for pollutant degradation under visible light irradiation. M Qamar et al. [135] prepared Pt/WO_3 nanocomposite by deposition of platinum onto the surface of tungsten oxide using a photo-deposition method. The synthesized material was used as catalyst in laser induced removal of Rhodamine 6G. Nanocasting method has been employed in this research work to synthesize mesoscaled In_2O_3 materials which was used to make composites material with tungsten oxide (WO_3). In_2O_3-WO_3 nanocomposites were explored as catalyst for photoconversion of CO_2 to methanol.

We chose SBA-15 as a hard template for the preparation process. Mesoporous silica SBA-15 is characterized by hexagonally ordered pore channels with diameter of order of few nanometers [26, 83, 86, 100]. The resulting composites materials were characterized by UV-vis, XRD, XPS, PL and FESEM analysis. Nanocasting is a hard template method which makes use of an ordered mesoporous solid as a structural matrix. Unlike nanocasting, soft template method utilizes the simple and direct sol-gel technique, that applies the traditional method of synthesizing ordered mesoporous substances.

CHAPTER 3

EXPERIMENTAL TECHNIQUES AND METHODS

This chapter explains experimental details related to synthesis of pure, doped and composite oxides semiconductor nanoparticles using wet chemical methods. Various characterization techniques adopted to investigate different properties of the synthesized materials are also discussed. The experimental procedure, set-up and design to test photocatalytic activities of photoassisted reduction of CO_2 to methanol on the synthesized semiconductor catalysts are explained in detail.

3.1 Synthesis of WO_3 nanoparticles

Ammonium paratungstate $\{(NH_4)_{10}(H_2W_{12}O_{42}).4H_2O\}$ was used as the precursor during synthesis of WO_3. A predetermined amount of the salt was dissolved in deionized water and vigorously stirred at 80 ^oC, while a warm, concentrated $HNO_3$was added dropwise. The solution mixture was kept at the temperature for about 1 hour under continuous stirring after which the precipitate was left to settle for about 24 hours at room temperature. Water was added followed by stirring for about 15 minutes to wash the precipitate, the mixture was left overnight to settle down before decantation of the liquid. The washing process was carried out twice after which the precipitate was removed by ultrafiltration using a polymer membrane with 0.48 μm pore size. The precipitates were dried at 100 ^{o}C overnight and then calcined at 600 ^{o}C with ramp rate of 5 ^{o}C/min. The temperature was maintained for 2 h and then cooled to room temperature.

3.2 Synthesis of SBA-15 supported and unsupported In_2O_3 nanocrystals

SBA-15 supported indium oxide nanocrystals was prepared according to the literature [86] with slight modification. A predetermined amount of $In(NO_3)_3.xH_2O$ was dispersed in ethanol and stirred until completely dissolved. This solution was then added to a flask containing SBA-15 and stirred at room temperature for about 4 hours, the weight ratio of $In(NO_3)_3.xH_2O$ to SBA-15 was 2:1. The thoroughly mixed solution was then filtered to recover the solid, and the residue was transferred to a furnace in a crucible and dried at 45 ^{o}C overnight with temperature increment rate of 1.0 ^{o}C/min. The indium precursor/SBA-15 powder was then transferred into a quartz glass bottle where it was thermally decomposed at 600 ^{o}C with temperature increase rate of 1.0 ^{o}C/min from the room temperature.

The temperature was maintained for 4 h before it it was left to cool to the room temperature. The silica template (SBA-15) was removed by dissolving the pre-formed SBA-15/ In_2O_3 composite with 20 g NaOH in 240 mL water and etched at 75 ^oC for 24 h. The indium oxide material was washed with deionized water, recovered by centrifugation and finally dried at 60 ^oC overnight, a light yellow product was obtained and transferred to a bottle labeled In_2O_3-M.

The traditional preparation of In_2O_3 nanocrystals, for comparative study, followed similar procedure without SBA-15. The precursor was heated at the same temperature as above for the same duration and the product was labeled In_2O_3-T.

3.3 Synthesis of In_2O_3-WO_3 nanocomposites

Synthesis of In_2O_3-WO_3 (denoted as MIW) composites were carried out by direct mixing. The solid mixture was well-grinded in mortal and pestle, followed by heat-treatment in a sealed quartz glass at 750 ^oC with ramp rate of 2 ^oC/min, and the temperature was maintained for 5 h before it was left cool to the room temperature. MIW nanocomposites were prepared by mixing In_2O_3 and WO_3 in the weight ratio $1:3$, $2:3$ and $1:1$ respectively which was tagged MIW-1 MIW-2 and MIW-3 respectively for comparative study. The synthesized WO_3, MIW-1, MIW-2 and MIW-3 were kept in separate bottles for further characterization and CO_2 photo-reduction application.

3.4 Synthesis of Nb- and Ta-doped WO_3 nanostructures

The synthetic method of the niobium (Nb)- and tantalum (Ta)-doped WO_3 are identical. Description for synthesis of Nb/WO_3 is discussed as follows: 3 g of P-123 poly(ethylene glycol)-poly(propylene glycol)-poly(ethylene glycol) was dissolved in 30 mL of isopropanol and the solution was stirred until completely dissolved. In a separate beaker, 2 mL niobium ethoxide ($C_{10}H_{25}NbO_5$) was dissolved in another 30 mL isopropanol containing 2 mL acetic acid. A 3 g ammonium paratungstate $\{(NH_4)_{10}(H_2W_{12}O_{42}).4H_2O\}$ was also dissolved completely in another 30 mL isopropanol in another beaker. The P-123-isopropanol solution was then added to a 50 mL of dilute HNO_3 and the solutions of Nb-ethoxide and ammonium paratungstate were added to it simultaneously, in drops, with continuous stirring until the solutions were thoroughly mixed. The whole mixture was then transferred into a Teflon-lined autoclave for hydrothermal treatment. The sealed autoclave was placed in the furnace at 40 ^oC for 10 days. The mixture was washed with deionized water by centrifugation followed by decantation. The recovered wet powder was dried in the oven and then calcined at 600 ^oC for 24 h at 2 ^oC/min ramp rate.

In a similar way to Nb/WO_3 Ta-doped WO_3 nanomaterial was synthesized using 1.5 mL tantalum ethoxide ($C_{10}H_{25}O_5Ta$) and 2.5 g of ammonium paratungstate $\{(NH_4)_{10}(H_2W_{12}O_{42}).4H_2O\}$ as the precursors.

3.5 Material characterization

Each successfully synthesized nanomaterial was characterized to study its various properties such as morphology, crystallinity, composition, porosity, optical properties, and UV-visible characteristics.

3.5.1 X-ray diffraction (XRD)

X-Ray Diffraction (XRD) is a powerful tool used for determining the lattice type, lattice parameters, and phase identification of unknown materials. Information from XRD pattern can also be used to estimate the crystallite sizes and strain in materials. Diffraction of X-Ray from the crystal materials was solved by Bragg in 1913. He regarded a crystal being made of parallel planes of atoms which spaced with a distance (d). XRD is based on constructive interference of monochromatic X-rays by a crystalline sample (see Figure 3.1). The condition of the constructive diffraction is given by the Bragg equation

$$n\lambda = 2d \sin\theta \tag{3.1}$$

Where the integer n is the order of the diffracted beam, is the distance between the atomic planes in the crystal or simply d-spacing, θ is the angle of diffraction from the plane, and λ wavelength of the x-ray. Bragg equation can be used to calculate the d-spacing of a material if the wavelength and the angle of the incident X-Ray are known.

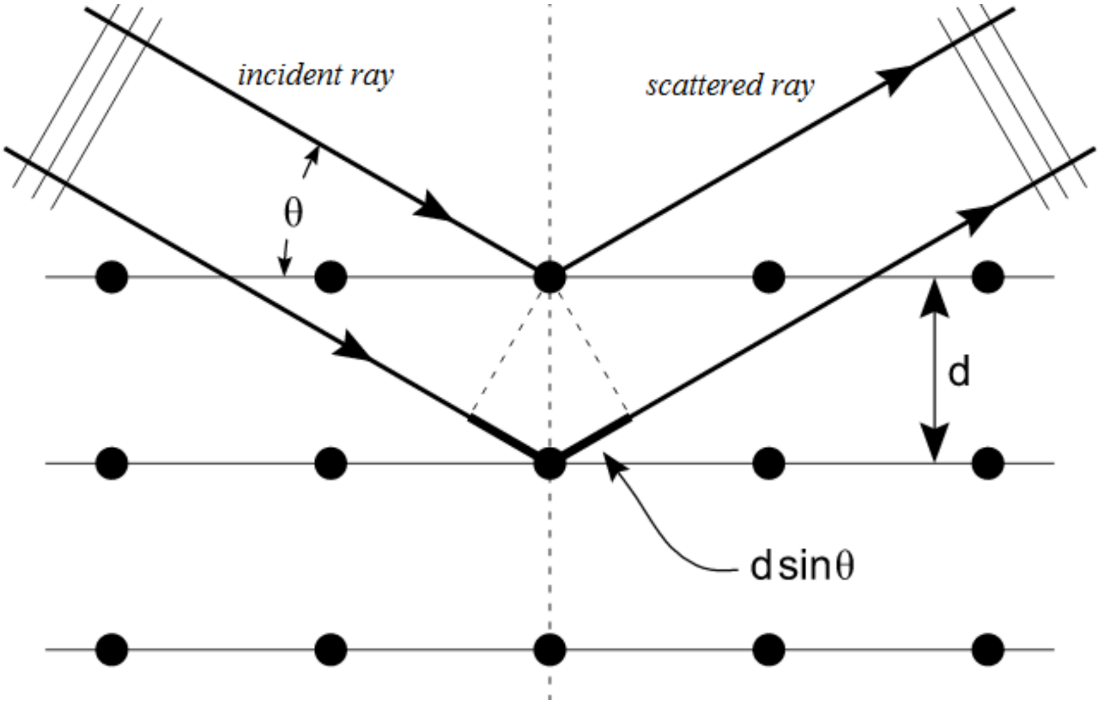

Figure 3.1: Schematic of Bragg diffraction

In a typical X-ray diffractometer, X-rays are generated within a sealed tube that is under vacuum. Electric current is applied which heats a filament within the tube thereby causing emission of electrons. The number of electrons emitted from the filament varies directly as the current applied. A high voltage, typically 15-60 kV, is applied within the tube which accelerates the electrons. The accelerated electrons then hit a target, usually made of copper where they are annihilated and produces X-rays [136, 137].

When a collimated beam of X-Ray hits a sample and is diffracted, the distances between the atomic planes of the sample can be measured by applying Equation 3.1. The intensity of the diffracted X-rays is measured as a function of the scattering angle 2θ. A series of peaks occur where each peak corresponds to x-ray diffracted from a specific set of planes in the specimen.

Reasons for peak broadening in XRD spectra include: Instrumental effects, presence of lattice strains or crystallite sizes. The smaller the crystallite size the broader the peaks. The broadening due the crystallite size is given by Equation 3.2 known as Scherrer equation. It is obtained from the derivative of Bragg's law keeping the wavelength constant and allowing the diffraction angle and the Bragg spacing to vary. Therefore the full width at half maximum (FWHM), B_c, of diffraction peak is given by:

$$B_c = \frac{k\lambda}{L\cos\theta} \tag{3.2}$$

Where λ is wavelength the X-ray, L is the crystallite size measured in a direction perpendicular to the surface of the specimen, θ is the diffraction angle, and k is the Scherrers constant of the order of unity for usual crystal.

The broadening of the peak, B_s, due to the presence of lattice strain is given by Equation 3.3 [138]:

$$B_s = \frac{2\eta}{\cot\theta} \tag{3.3}$$

where η is the elastic strain.

To estimate the instrument effect on the peak broadening, the broadening of a well-annealed powder can be calculated, where the grain size is very large as compared to Scherrer effect and the lattice strain. In this work, the synthesized materials were analyzed by X-ray powder diffraction using a Rigaku mini-XRD with CuK_α radiation source ($\lambda = 0.1540$ nm) at a scanning rate of 2^o/min within

2θ range of 2^o to 90^o. The XRD diffractometer apparatus used is available at the Center of Research Excellence in Nanotechnology (CENT).

3.5.2 Field emission scanning electron microscope (FE-SEM)

A scanning electron microscope (SEM) is a type of electron microscope that produces images of a sample by scanning it with a focused beam of electrons. The interaction of electrons with atoms in the sample results in production of various signals that contain information about the surface topography and composition of the sample. The types of signals produced by an SEM include secondary electrons (SE), back-scattered electrons (BSE), photons of characteristic X-rays and light (cathodoluminescence) (CL), absorbed current (specimen current) and transmitted electrons. Secondary electron detectors are standard equipment in all SEMs, but it is rare that a single machine would have detectors for all other possible signals. The signals result from interactions of the electron beam with atoms at various depths within the sample which is, in the most common or standard detection mode, secondary electron imaging (SEI), the secondary electrons are emitted from very close to the specimen surface. Consequently, SEM can produce very high-resolution images of a sample surface. Due to the very narrow electron beam, SEM micrographs have a large depth of field yielding a characteristic three-dimensional appearance useful for understanding the surface structure of a sample [139].

The major difference between the a typical Scanning Electron Microscope (SEM) and the Field Emission Scanning Electron Microscope (FESEM) is the type of electron emitter. SEM uses thermionic emitter while FESEM uses field emitter. Thermionic Emitters use electrical current to heat up a filament; the two most common materials used for filaments are Tungsten (W) and Lanthanun Hexaboride (LaB_6). When the heat is enough to overcome the work function of the filament material, the electrons can escape from the material itself. Thermionic sources have relatively low brightness, evaporation of cathode material and thermal drift during operation. Field Emission is one way of generating electrons that avoids these problems. A field emission Gun (FEG); also called a cold cathode field emitter, does not heat the filament. The emission is reached by placing the filament in a huge electrical potential gradient. The FEG is usually a wire of Tungsten (W) fashioned into a sharp point [140].

The morphological properties of the synthesized materials were studied by using Lyra TESCAN Field emission electron microscope (FESEM) equipped with an energy dissipative X-ray spectrometer, available at the Center of Research Excellence in Nanotechnology (CENT). Samples to be analyzed must be electrically conductive, at least at the surface, and electrically grounded to prevent the accumulation of electrostatic charge at the surface. They are therefore usually coated with an ultrathin coating of electrically conducting material, deposited on the sample either by low-vacuum sputter coating or by high-vacuum evaporation [139, 140]. Gold was the conductive material used for material coating in this work

3.5.3 Brunauer-Emmett-Teller (BET) analysis

BET analysis provides specific surface area evaluation of materials by nitrogen multilayer adsorption measured as a function of relative pressure using a fully automated analyser. The technique encompasses external area and pore area evaluations to determine the total specific surface area in m^2/g yielding important information in studying the effects of surface porosity and particle size in many applications.

Barrett-Joyner-Halanda (BJH) analysis can also be employed to determine pore area and specific pore volume using adsorption and desorption techniques. This technique characterises pore size distribution independent of external area due to particle size of the sample. Examples of informations that can be obtained from BET analysis are highlighted below [142]:

- Rapid single point and multipoint specific BET surface area determinations.
- Full BET surface area characterization of disperse, nonporous or macroporous materials pore diameter > 50 nm, identified by type II isotherms, and mesoporous materials with pore diameter between 2 nm and 50 nm, identified by type III and IV isotherms
- BET surface area characterization of microporous materials (< 2 nm, type I isotherms).

- Pore volume and pore area distributions in the mesopore and macropore ranges using BJH analysis with a full complement of adsorbate thickness models.

- BJH adsorption and desorption average pore diameter determinations

The concept of the theory is an extension of the Langmuir theory, which is a theory for monolayer molecular adsorption, to multilayer adsorption with the following hypotheses:

- gas molecules physically adsorb on a solid in layers infinitely;

- there is no interaction between each adsorption layer; and

- the Langmuir theory can be applied to each layer.

The resulting BET equation is

$$\frac{1}{v\left(\frac{p}{p_o}-1\right)} = \frac{c-1}{v_m c}\left(\frac{p}{p_o}\right) + \frac{1}{v_m c} \tag{3.4}$$

where p and p_o are the equilibrium and the saturation pressure of adsorbates at the temperature of adsorption respectively, v is the adsorbed gas quantity (for example, in volume units), and v_m is the monolayer adsorbed gas quantity. c is the BET constant. v_m and c can be obtained from the slope and intercept of isotherms of the quantity in the left hand side of Equation 3.4 plotted against the ratio $\frac{p}{p_o}$. The total surface area S_{total} and the specific surface area S_{BET} are expressed as follows

$$S_{total} = \frac{v_m N s}{V} \tag{3.5}$$

$$S_{BET} = \frac{S_{total}}{a} \tag{3.6}$$

Where N, s, V and a are Avogadro's number, the adsorption cross section of the adsorbing species, the molar volume of the adsorbate gas and the mass of the solid sample or adsorbent [141, 142].

A micromeritics accelerated surface area and porosimeter (ASAP 2020) system, available in CENT, was used in studying the porosity of the materials by carrying out nitrogen adsorption-desorption analysis of the catalysts. The system is equipped with software which uses conventional methods of calculation and analysis such as Brunauer-Emmett-Teller (BET) and Barrett-Joyner-Halanda (BJH) methods for determination of the textural properties, like specific surface area and pore size distribution respectively. The kind of porosity in a material was determined from its isotherm type. Figure 3.2 depicts sketches of different isotherm types.

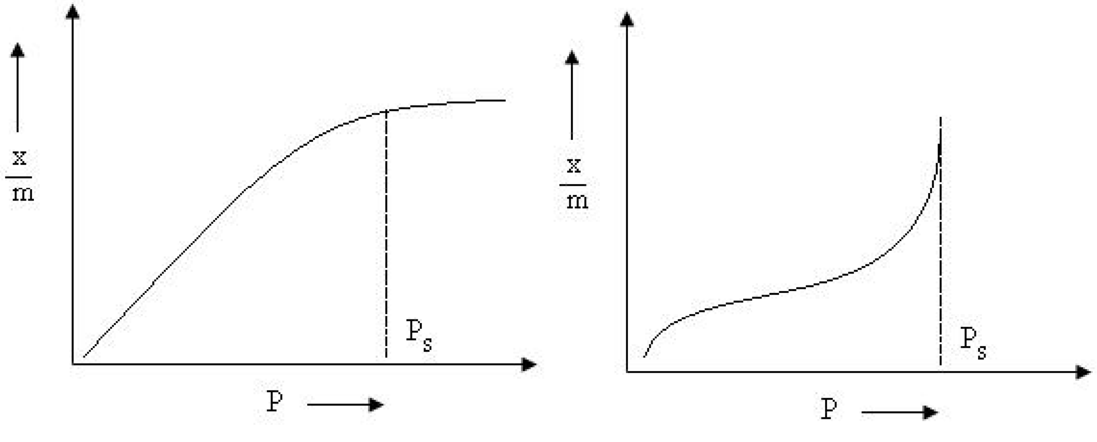

Type I Adsorption Isotherm

Type II Adsorption Isotherm

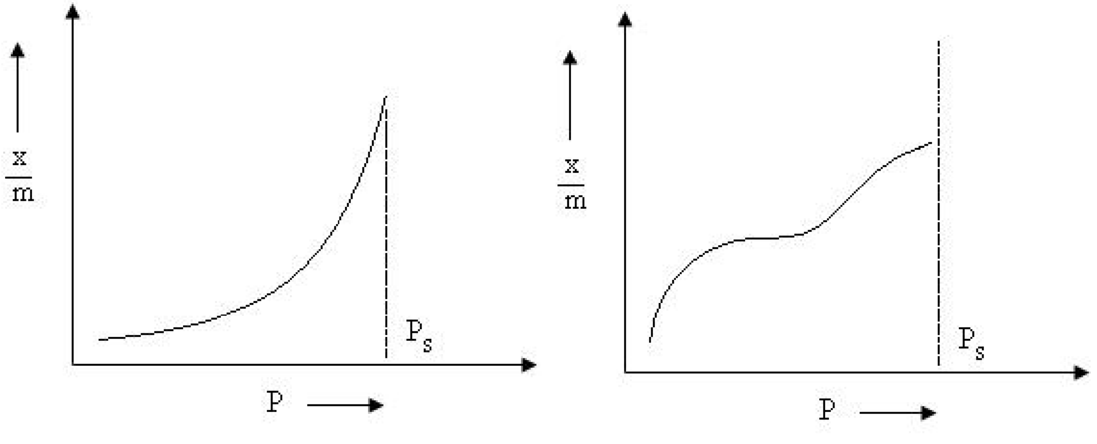

Type III Adsorption Isotherm

Type IV Adsorption Isotherm

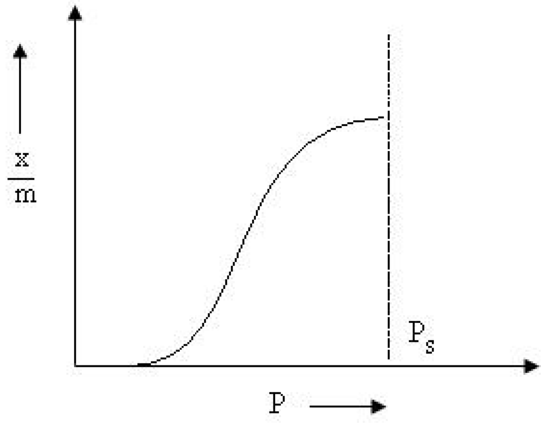

Type V Adsorption Isotherm

Figure 3.2: Sketches of different types of isotherm

3.5.4 UV-visible spectroscopy

UV-Vis spectroscopy is a characterization technique for measurement of optical or electronic properties of different solid and liquid materials by the transmission, absorption or reflection of light in the visible and UV region. A conventinal UV-vis spectrometer consists of: source of light, such as incandescent lamp for the visible or deuterium lamp, for the ultraviolet region, sample holder, reference cell (in double beam) and detector such as photodiode by using monochromator to filter the light. UV-vis spectrometer has either single beam or double beam. In single beam, the intensity of light pass through the sample cell. Light that strikes the sample could be absorbed, reflected or transmitted. When the sample is solution in a cell, the transmittance (T) is defined as the ratio $\frac{I}{I_o}$ where I_o and I denote the intensity of light that is incident on the sample and the transmitted intensity respectively. Absorbance (A) of the sample is given by the Beer Lamberts law as follow:

$$A = -\log_{10}(\frac{I}{I_o}) = \epsilon \times c \times L \tag{3.7}$$

where ϵ is a constant known as the molar absorptivity, c is the concentration of the absorbing species into the solution. L is absorption path length.

In this work, the UV-vis absorption spectroscopy of the samples were carried out by using Jasco 670 with double beam spectrophotometer in the wavelength range 200 nm to 700 nm. Tauc plots were obtained for each sample to estimate their respective band gaps. The band gap, E_g, of the materials was determined by using the following equation

$$h\nu\alpha = K(h\nu - E_g)^n \tag{3.8}$$

where h, ν, α, E_g and K represent the Planck's constant, frequency of vibration, absorption coefficient, band gap and constant of proportionality respectively. It is well known that the optical absorption near the band edge for crystalline semiconductors follows the stated equation [109, 110]. The value of the exponent n depends on the nature of the sample transition. The value of n used in this work is $\frac{1}{2}$ since all the semiconductor materials used exhibit direct transition. The α in Tauc equation denotes the so-called Kubelka-Munk or remission function which is given by Equation 3.9

$$\alpha = \frac{(1 - R^2)}{2R} \tag{3.9}$$

where R is the reflectance. The relational expression becomes the linear extrapolation of the plots of $(h\nu\alpha)^{\frac{1}{2}}$ against $h\nu$.

3.5.5 Fluorescence spectroscopy

Photoluminescence (PL) refers to optical radiation emitted by a semiconducting crystal during de-excitation process of its photo-excited electron. Absorption of photon, with energy greater than the band gap of a semiconductor, by an electron in the valence band will cause transition into the conduction band across the energy gap. Photoexcited electron generally has excess energy which must be emitted before returning to its lowest energy level. During the process of transition back into the valence band, the energy is released in form of a luminescent photon which is emitted from the material. Thus, the energy of the emitted photon is a direct measure of the band gap energy, E_g. The process of photon excitation followed by photon emission is called photoluminescence. The photoluminescence characteristics of the as-obtained semiconductor catalysts were investigated by a Fluorolog FL3-iHR, HORIBA Jobin Yvon which uses xenon lamp as light source, using 350 nm excitation wavelength.

3.5.6 X-ray photoelectron spectroscopy

X-ray photoelectron spectroscopy (XPS) is a surface-sensitive quantitative spectroscopic technique that measures the elemental composition, in the parts per thousand range, empirical formula, chemical state and electronic state of the elements that exist within a material. XPS spectra are obtained by irradiating a material with a beam of X-rays while simultaneously measuring the kinetic energy and number of electrons that escape from the top 0 to 10 nm of the material under analysis. It requires high vacuum or ultra-high vacuum (UHV). Highlight of task which can be carried by a typical XPS apparatus is given below:

1. elemental composition of the surface (top $0 - 10$ nm usually)
2. empirical formula of pure materials
3. elements that contaminate a surface

4. chemical or electronic state of each element in the surface
5. uniformity of elemental composition across the top surface (or line profiling or mapping)
6. uniformity of elemental composition as a function of ion beam etching (or depth profiling)

The basic physics involved in XPS technique can be described based on the following Einstein equation:

$$E_B = h\nu - E_K - E_R - \phi - \delta E \tag{3.10}$$

Where E_B is the binding energy of the electron in the atom which vary with the type of atom. Various binding energies corresponding different elements in various chemical states are well documented in handbooks of atomic data which can be consulted for reference. E_K is the kinetic energy of the emitted electron that is measured by XPS spectrometer. $h\nu$ is the energy of the photons in X-ray source. E_R is the recoil energy which is very small and usually can be neglected, ϕ is the work function, and δE is the charge shift.

X-ray photoelectron spectroscopy (XPS) was the spectroscopic technique used to measures the elemental composition, chemical state and electronic state of the elements that exist within the synthesized nanomaterial.

3.6 Application: Photocatalytic reduction of CO_2 to methanol

The schematic of the setup for the photo-reduction of CO_2 to methanol, with 355 nm laser as the irradiation source, is given in Figure 3.3. The setup is identical to that with 266 nm laser irradiation source, except that the third harmonic generator is replaced with a fourth harmonic generator. The reactor for the photocatalytic activities over the synthesized nanostructures is a cylindrical cell made of stainless steel with quartz windows at the top. A gas inlet with a needle valve and an outlet fixed with rubber septum are located along the cross-section of the cylinder for passage of the CO_2 gas and dispensation of the sample respectively. The sample is dispensed through the septum by use of micro-syringe to avoid opening the reaction cell during the process.

The source of irradiation for the reaction is either 266 nm or 355 nm high power laser beam respectively generated from the fourth or third harmonic of the Spectra Physics Nd: YAG laser (Model GCR 250) with pulse width of $\sim$ 8 ns. The diameter of the laser beam was expanded to $\sim$ 1.5 cm to avoid destructive effect of the radiation.

High purity CO_2 gas (99.99 %) was purged into 100 mL water containing the selected catalyst with constant stirring for about 30 min prior to turning on the pulsed laser. The purging of CO_2 continued during the entire process and the samples were extracted from the cell at intervals for GC analysis. The laser pulse energy, though quite stable, was monitored during the whole experiment. The reactants mixture was analyzed for presence of methanol and other products after 30 min before the laser irradiation started but no product was identified in the absence of light. This procedure is similar for each process of photocatalytic CO_2 reduction to methanol over each of the semiconductor materials.

The liquid analysis of the sample was carried out by using gas chromatograph (Agilent 4890D) equipped with a two-column system connected to a mass spectrometry detector (MSD) and a flame ionized detector (FID) respectively. The separation of the components was carried out on Rtx-Wax column (30 m × 0.32 mm × 0.32 mm) under temperature programmed conditions and detected by MSD. 1.0 μL of the liquid samples were manually injected into the GC under the following conditions: Initial oven temperature set at 30 ^{o}C which was then increased to 100 ^{o}C at heating rate of 5 ^{o}C/min and then increased to 200 ^{o}C at the rate of 30 ^{o}C/min to evacuate all the components from the column. The total analysis run time was 15.5 min. The injector and detector were both set at 170 ^{o}C and the carrier gas was helium.

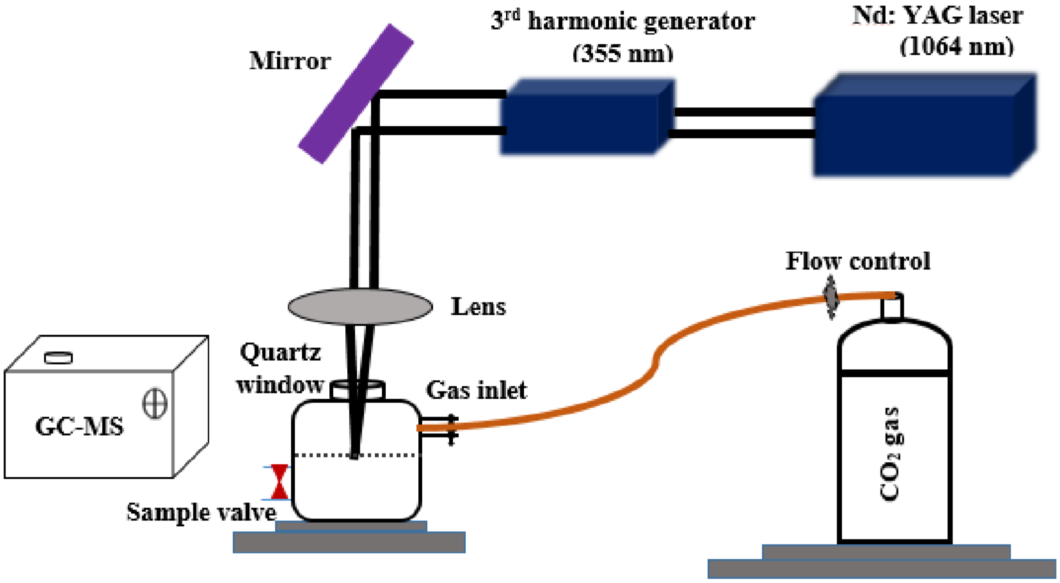

Figure 3.3: Schematic diagram of the experimental set up used for studying photocatalytic activities of the materials with 355 nm laser as the irradiation source

CHAPTER 4

RESULTS AND DISCUSSION

4.1 Characterization of the nanocatalysts

This chapter presents results of various characteristic analyses performed on each of the synthesized materials. The analysis results discussed include; X-ray powder diffraction (XRD), Field emission scanning electron microscopy (FESEM), Brunauer-Emmett-Teller (BET), UV-Vis spectrophotometry, X-ray photoelectron spectroscopy and photoluminescence analyses

4.2 Phase identification and crystal structure analysis

Crystal structure and phase identification as well as strain and crystallite sizes of the synthesized materials were studied using X-ray powder diffraction discussed in chapter three. Phase present along with estimated lattice parameters, crystallite sizes and microstrains are listed for each material in Table **??** Results of respective XRD analyses are discussed in detail in the following subsections.

4.2.1 XRD analysis of In_2O_3-T and In_2O_3-M nanocrystals

Figure 4.1 depicts the XRD pattern of the as prepared ordered mesorporous In_2O_3-T and In_2O_3-M nanocatalysts. The main diffraction peaks for both samples can be indexed to (211), (222), (400), (440) and (622) cubic plane with lattice parameters 1.0111 nm (JCPDS card No 71-2195) and 1.0115 nm (JCPDS card No 06-0416) respectively. The extra and more prominent peaks observed in the mesostructured In_2O_3-T is attributed to its more crystalline structure. The crystallite sizes are calculated, by Scherrer equations [66] to be around 100 nm and 69.2 nm for In_2O_3-T and In_2O_3-M catalysts while the microstrains are estimated to be around 4.0×10^{-4} nm and 1.9×10^{-2} nm respectively. The effect of larger strain and small crystallites is shown by larger broadening in the XRD pattern of the In_2O_3-M nanocatalyst which often arise from dislocation, precipitate or other forms of defects [102]. Extra defects are however expected to create more active sites which increases adsorption ability and hence photocatalytic activities of the mesoporous material.

4.2.2 XRD analysis of WO_3 and In_2O_3-WO_3 nanocomposites

The X-ray powder diffraction patterns of the as prepared WO_3, MIW-1 MIW-2 and MIW-3 are shown in Figure 4.2. It is observed from the patterns that the WO_3 phase present is monoclinic with lattice parameters $a = 0.7283$ nm, $b = 0.7477$ nm and $c = 0.3822$ nm (JCPDS Card No 01-083-0950) [103]. The major reflections of the phase are (002), (020) and (200). It is worth noting that presence of In_2O_3 is confirmed by the additional peaks in the pattern for MIW-1 MIW-2 and MIW-3. The slight increase in the heights of the main peaks, (200) (002) and (020), implies higher crystallinity in the composite materials as compared to the pure WO_3. The phase of the In_2O_3 present in the composites is cubic with lattice parameters 1.0118 nm (JCPDS card No 06-0416) [104].

4.2.3 XRD analysis of Ta/WO_3 and Nb/WO_3 nanostructures

The XRD patterns of the as-prepared Ta/WO_3 and Nb/WO_3 are given in Figure 4.3. The diffraction peaks can be indexed to the pure hexagonal phase of WO_3 (JCPDS card No 33-1387). Planes (001) showed, compared with other planes, the strongest XRD peak intensity for both Ta/WO_3 and Nb/WO_3. This simply indicates that major growth direction is the (001) plane. We can therefore infer the following from the results; (i) Absence of typical XRD peaks for Nb_2O_5 and Ta_2O_5 indicates that Nb and Ta may be in the lattice space of WO_3 and that the concentration of Nb and Ta doping are too low to be detected by XRD. (ii) The lattice type of WO_3 changed from monoclinic to hexagonal structure which could be attributed to effect of heat treatment. Low crystallinity of the doped materials is also observed from the appearance of the XRD patterns. High peak broadening is an indication of small crystallite sizes or high strain effect. This may be attributed to the space available within the WO_3 cell being smaller than diameters of the Nb^{5+} or Ta^{5+}. This can cause distortion and consequently induce more defects [77, 106].

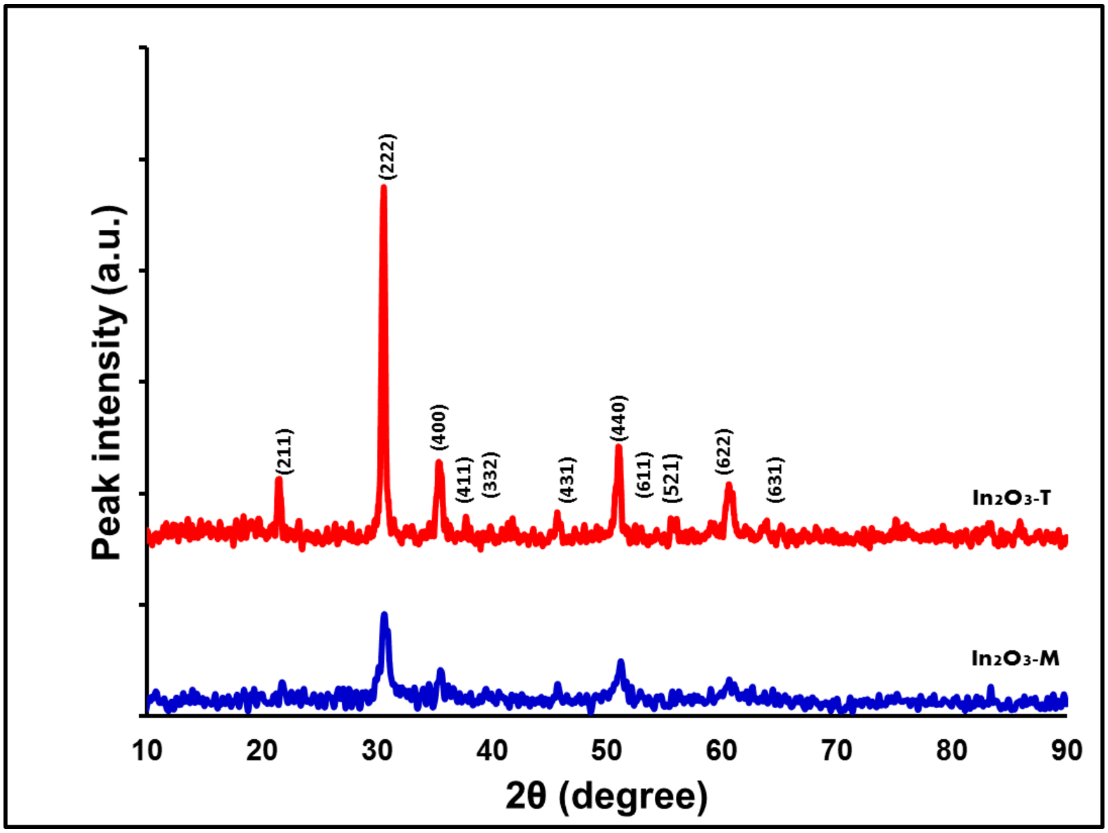

Figure 4.1: XRD patterns of In_2O_3-T and In_2O_3-M semiconductor nanocatalysts

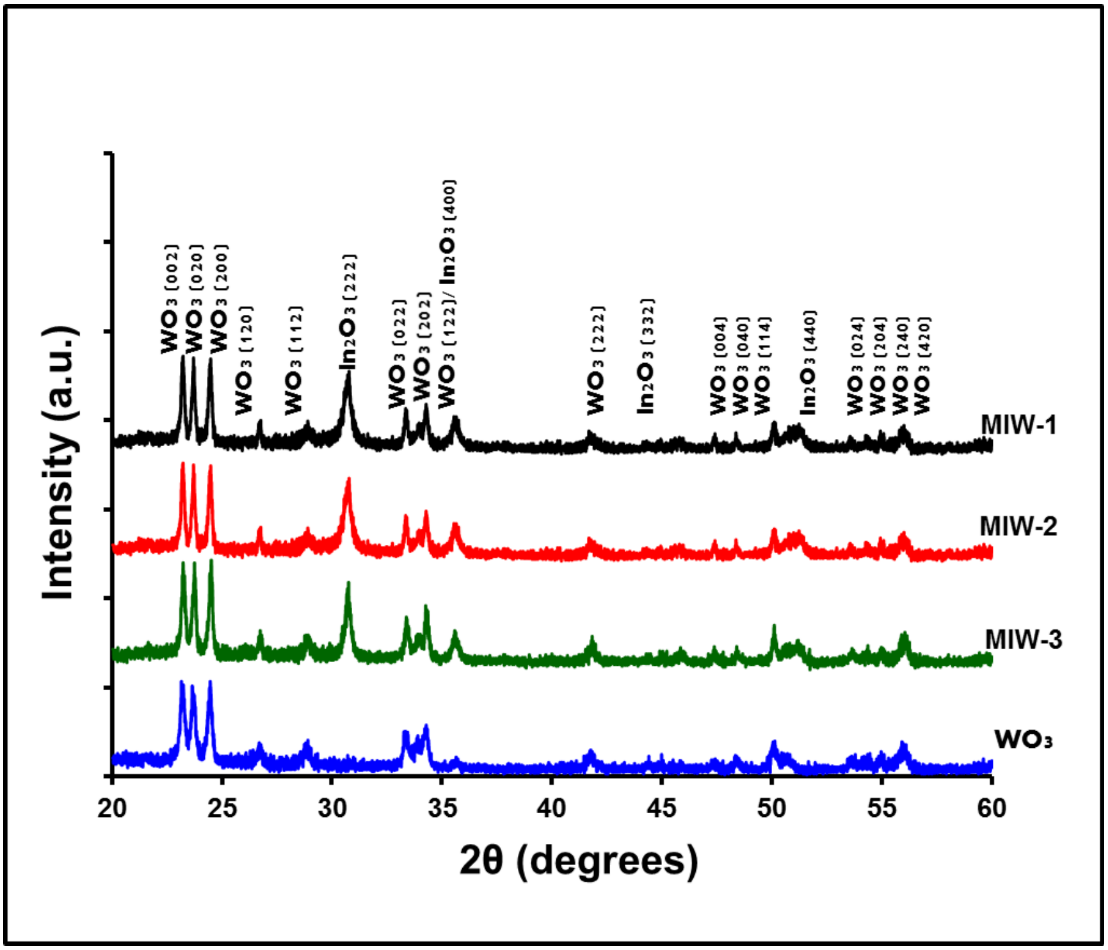

Figure 4.2: XRD patterns of WO_3, MIW-1, MIW-2, and MIW-3 nanocomposites

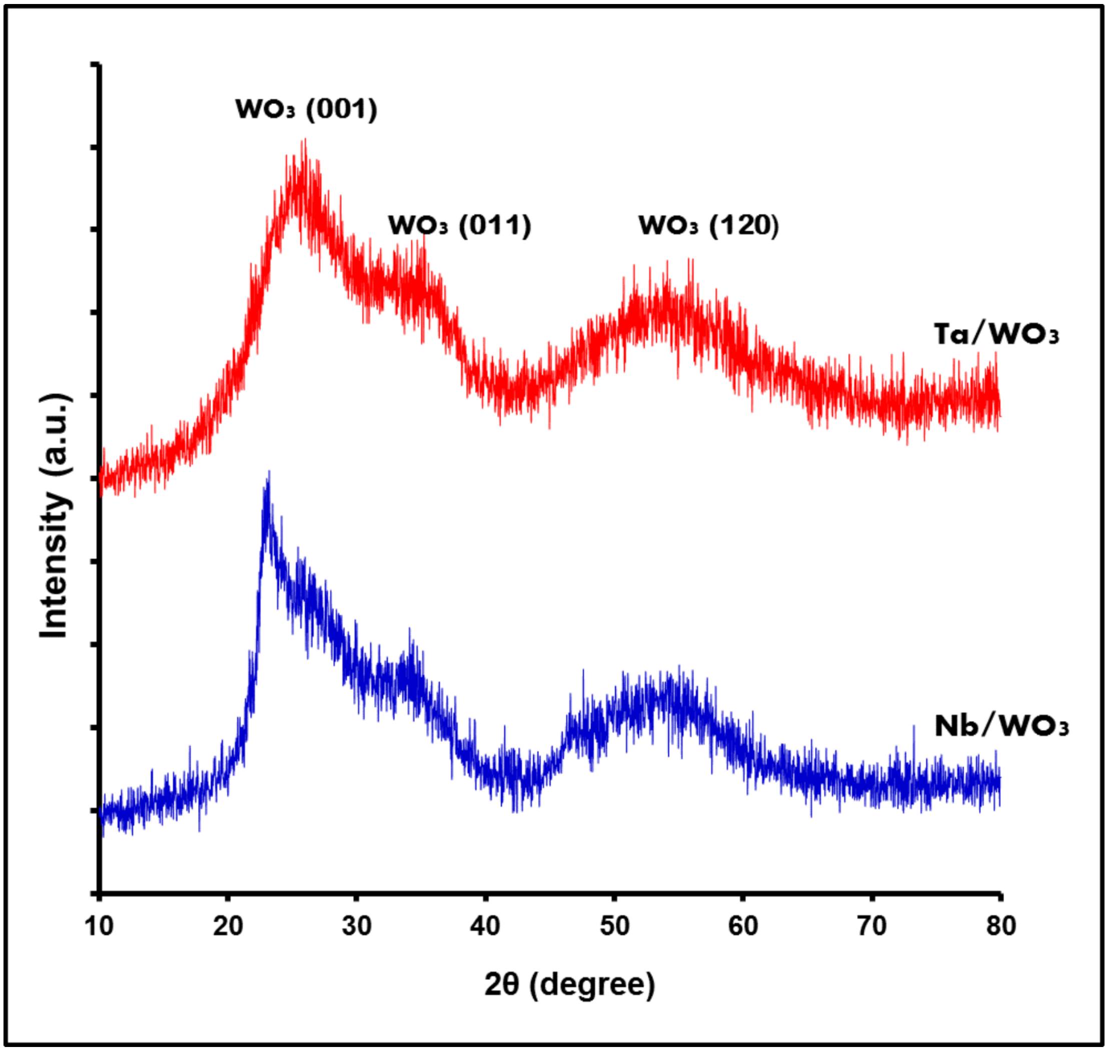

Figure 4.3: XRD patterns of Ta/WO_3 and Nb/WO_3 nanostructures

Table 4.1: Summary of the results of XRD analysis on the as-synthesized nanocatalysts

S/N	**Material**	**Phase present**	**Lattice parameter**		
			a (nm)	b(nm)	c(nm)
1	WO_3	monoclinic	0.7283	0.7477	0.3822
2	MIW-1	monoclinic/cubic	0.7279	0.7477	0.3822
3	MIW-2	monoclinic/cubic	0.7280	0.7482	0.3821
4	MIW-3	monoclinic/cubic	0.7275	0.7479	0.3822
5	In_2O_3-T	cubic	1.0111	1.0111	1.0111
6	In_2O_3-M	cubic	1.0115	1.0115	1.0115

4.3 Analysis of morphology of the materials

It has been discussed earlier that the reaction performance of a nanoscale photocatalyst particle is deeply affected by its size and shape. The reactive facet of a morphology-dependent photocatalyst, on which the active sites can be enriched and tuned, could be selectively exposed [107]. In this study, Lyra TESCAN Field emission electron microscope (FESEM) was used to study the surface morphology of each of the materials synthesized. Details of the results are discussed in the subsequent subsections

4.3.1 Morphology of In_2O_3-T and In_2O_3-M nanocrystals

Results showing the surface morphologies of the In_2O_3-T and In_2O_3-M nanostructures are displayed in Figure 4.4, where it is confirmed that the synthesized materials are nanoscaled and the particles are well dispersed. The result of x-ray diffraction is validated by higher crystallinity and quasi-nanocubic nature of the In_2O_3-T as observed directly from the images. It can also be seen from the figure that In_2O_3-T has larger particle sizes, a property that can be associated with its anticipated smaller specific surface area. However, the lesser crystalline In_2O_3-M nanoparticles are characterized by rougher surfaces.

4.3.2 Morphology of WO_3 and In_2O_3-WO_3 nanocomposites

Figure 4.5-4.7 are the FESEM images showing morphologies of WO_3, In_2O_3 and MIW-3. The nanoclusters of the synthesized WO_3 is depicted in Figure 4.5 with particle sizes ranges from about 33 nm to 45 nm. The ordered mesoporous indium oxide depicted in Figure 4.6 has slightly larger particle sizes with rougher surface. The morphological picture of the MIW-3 (Figures 4.7) further confirms the hindrance caused to the crystal growth in WO_3 nanoparticle clusters during the heat treatment by the presence of the In_2O_3, since no significant increase in the particle size of the WO_3 is observed. However, addition of the In_2O_3 particles enhances the crystallinity of the composite and smoothen the particle surfaces.

4.3.3 Morphology of Ta/WO_3 and Nb/WO_3 nanostructures

The FESEM images of the as-obtained Nb/WO_3 and Ta/WO_3 nanoparticles are presented in Figures 4.8 and 4.9 respectively. The images demonstrate change in WO_3 morphology as a result of doping. The dopants had little influence on the morphology of the final products when compared with the undoped WO_3 sample (Figure 4.5) which composed of slightly larger sizes of interconnected nanoparticles. Slightly larger agglomeration of nanoparticles due to doping was also obtained. The dopant ions could enter into WO_3 lattice to replace W^{5+} or W^{6+} ions, because of their slightly larger ionic radius, and cause blurring in the lattice fringe of the WO_3 nanoparticles which can lead to the appearance of various crystal defects. Emergence of the crystal defects provide favorable location sites for the dopant ions. This deduction coincides with some literature [77] and elsewhere, with the result of Mo-doped WO_3 [108].

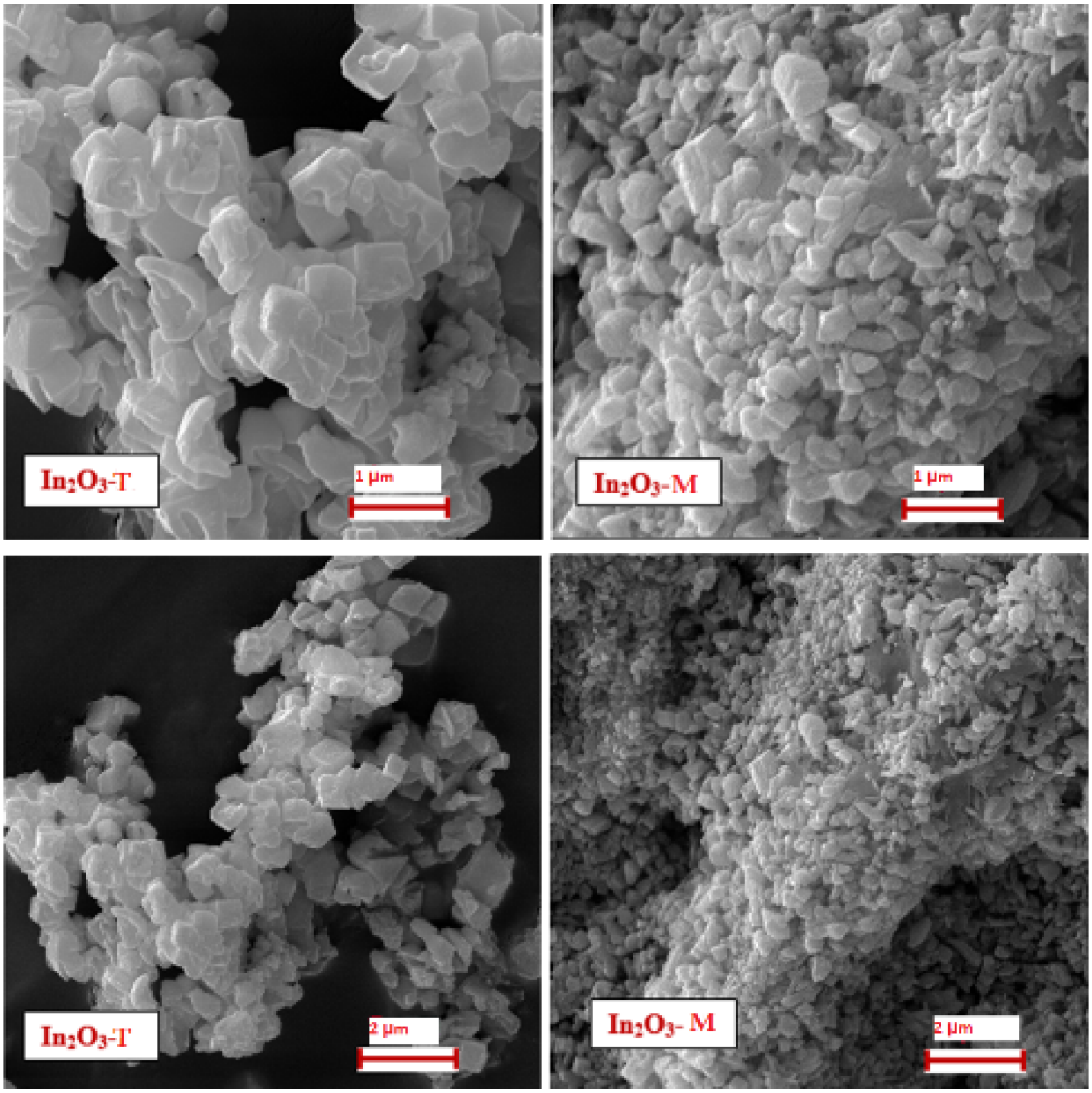

Figure 4.4: FE-SEM images of as-synthesized In$_2$O$_3$-T and In$_2$O$_3$-M semiconductor nanocatalysts at different magnifications

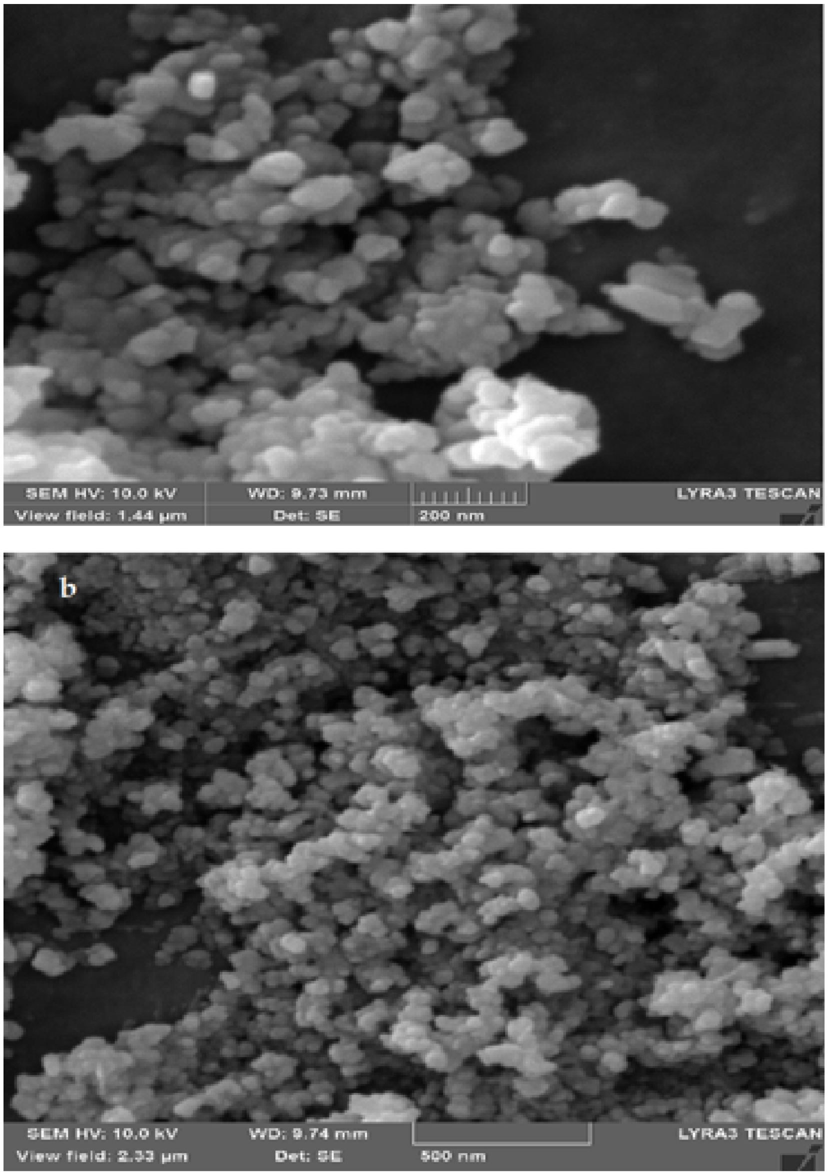

Figure 4.5: FE-SEM images of as-synthesized WO_3 nanostructure at different magnifications

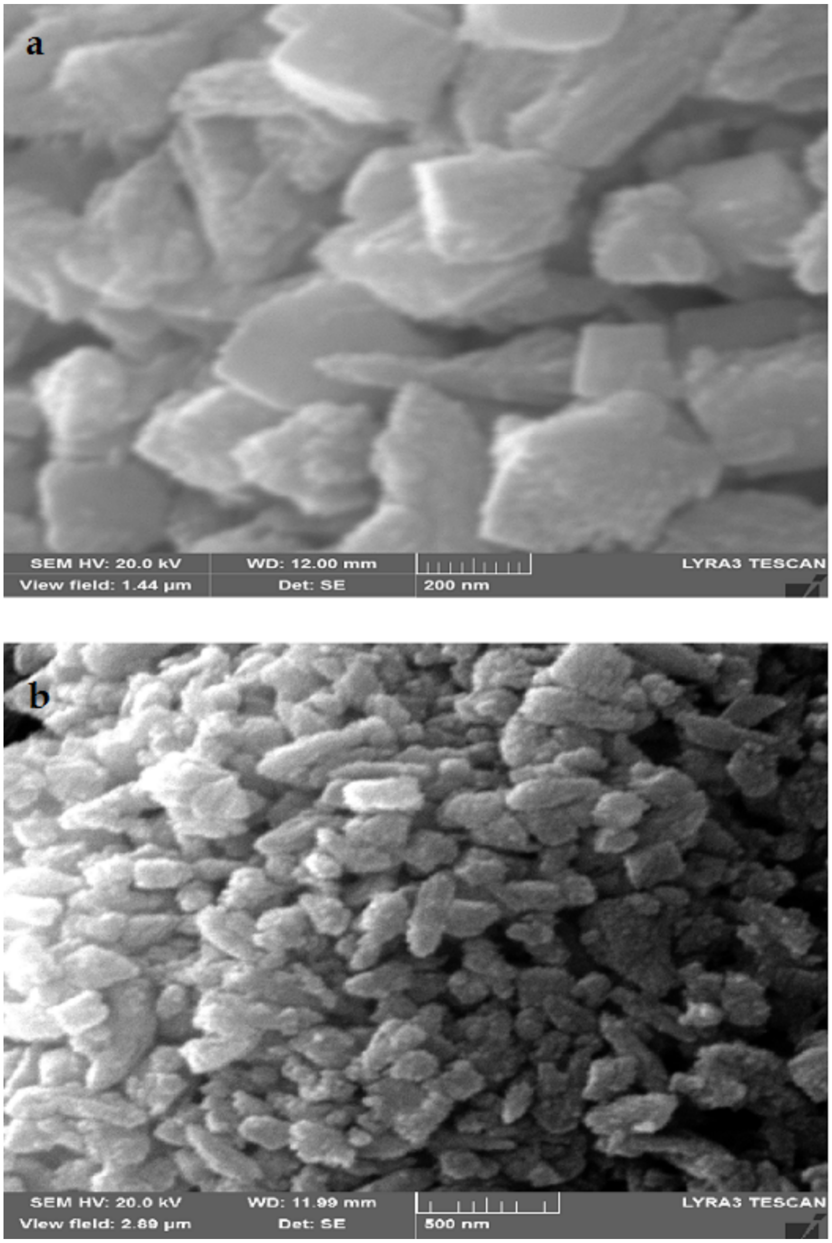

Figure 4.6: FE-SEM images of as-synthesized In_2O_3 nanocrystals at different magnifications

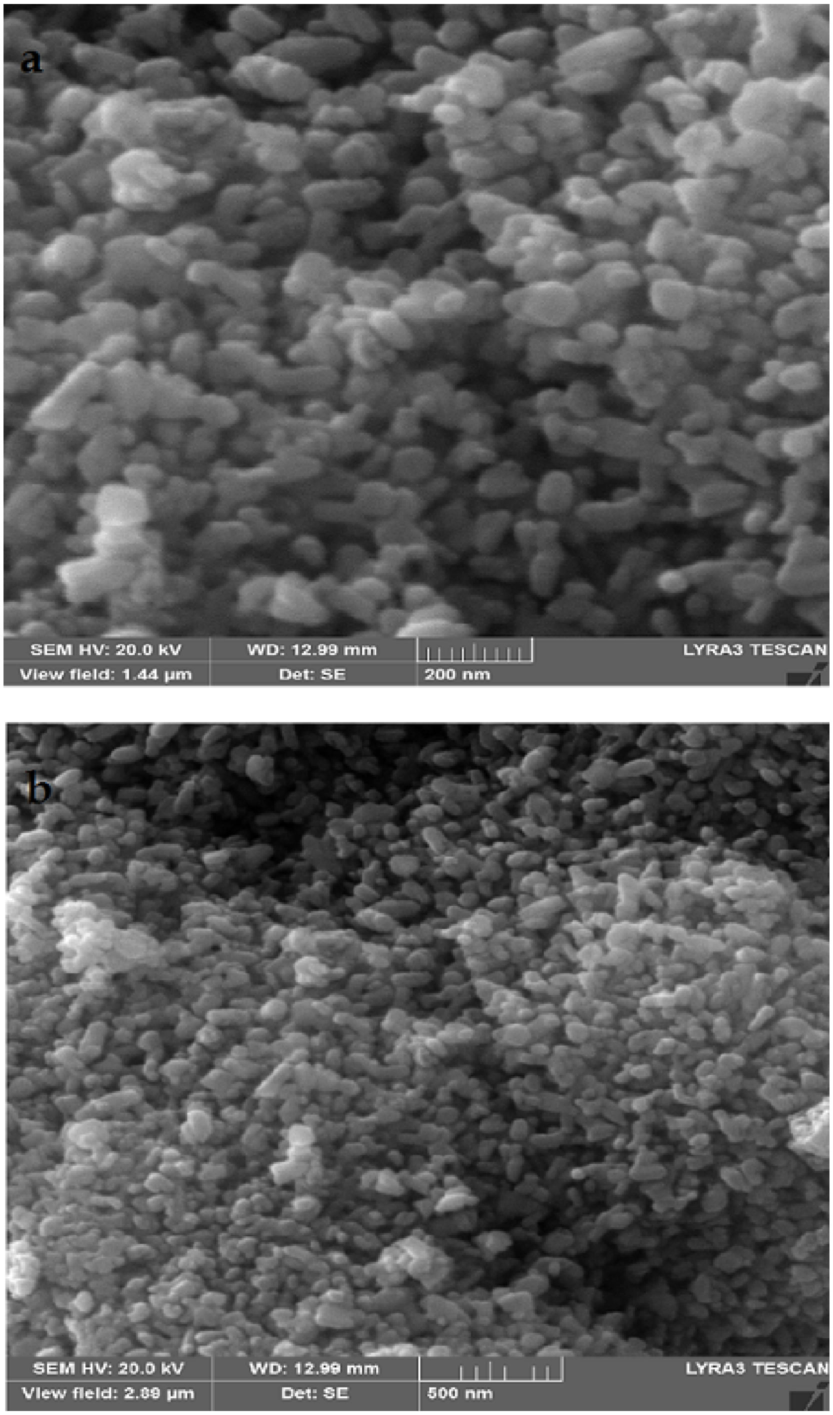

Figure 4.7: FE-SEM images of as-synthesized MIW-3 nanocomposites at different magnifications

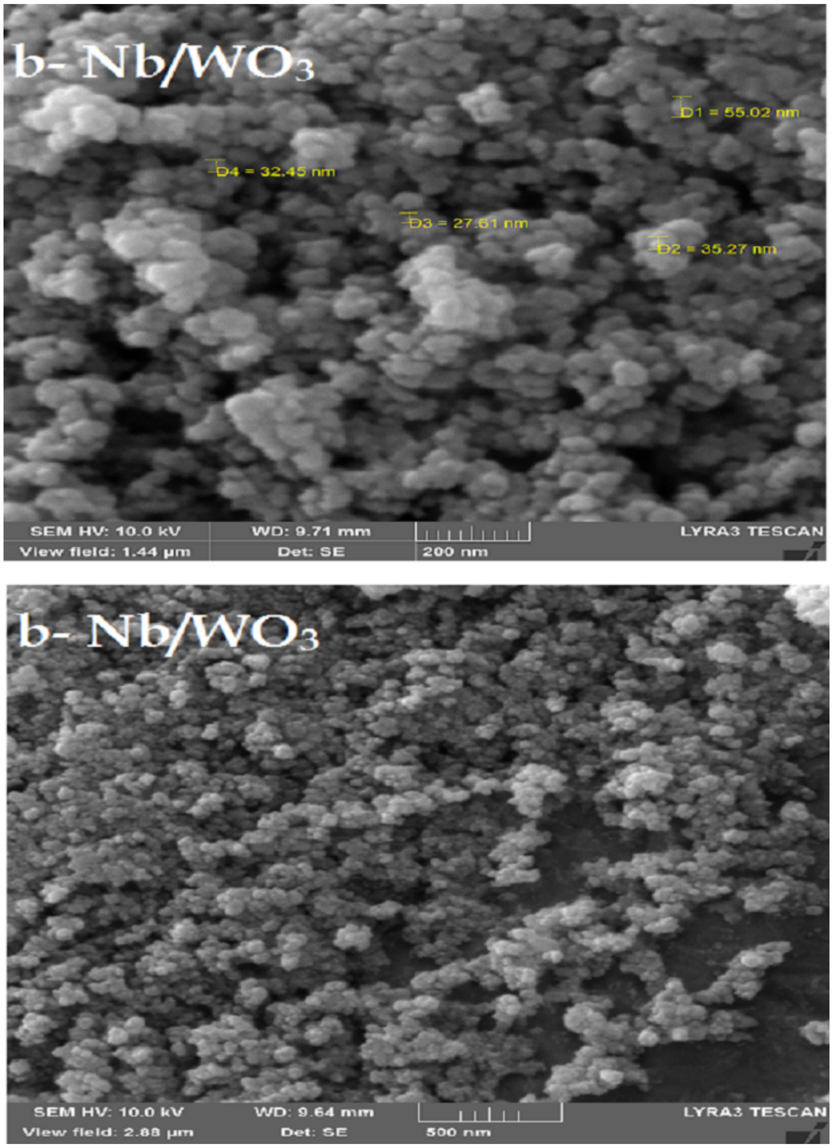

Figure 4.8: FE-SEM images of as-synthesized Nb/WO_3 nanoparticles at different magnifications

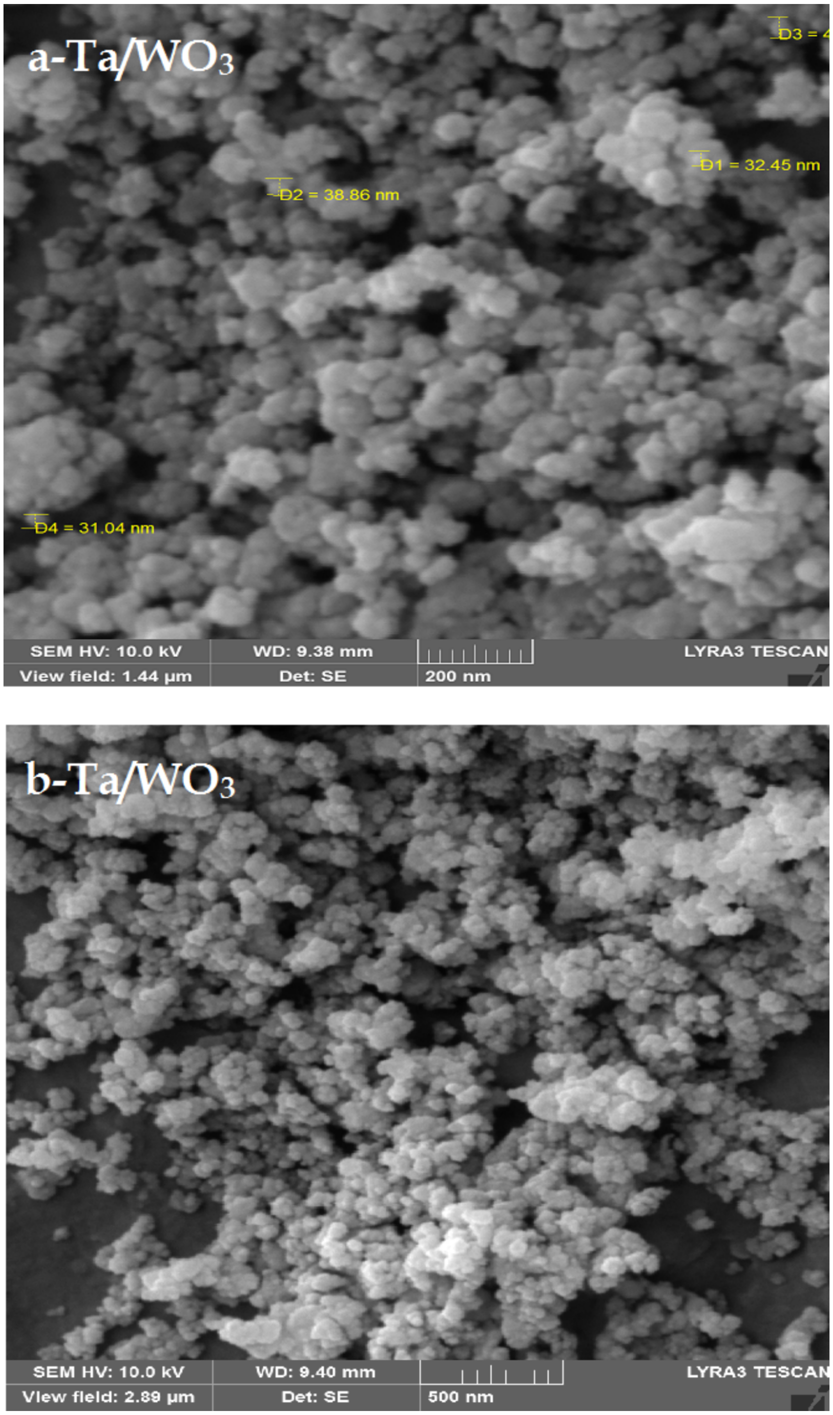

Figure 4.9: FE-SEM images of as-synthesized Ta/WO$_3$ nanoparticles at different magnifications

4.4 Analysis of N_2 adsorption-desorption of the materials

Nitrogen adsorption-desorption analysis of the semiconductor catalysts were carried out with the use of a micromeritics accelerated surface area and porosimeter (ASAP 2020). Pore volume distribution of the samples were also estimated as can been seen in Table 4.2

4.4.1 N_2 adsorption-desorption analysis of In_2O_3-T and In_2O_3-M nanocrystals

The specific surface areas, pore sizes and pore volumes analysis of the In_2O_3-T and In_2O_3-M nanomaterials, measured by BET and BJH respectively, are given in Table 4.2. The specific surface area ($= 56.1$ m^2/g) from BET analysis confirms that In_2O_3-M nanocrystals has smaller particle sizes compare to In_2O_3-T catalyst due to difference in the synthetic methods. The pore volume distribution of In_2O_3-T, In_2O_3-M and SBA-15 materials are shown in Figure 4.10, 4.11 and 4.12 respectively along with the nitrogen adsorption-desorption isotherms. In_2O_3-T and In_2O_3-M show type III and type IV hysteresis loops respectively which is evidence of presence of mesopores in the materials [86]. The increased specific surface areas aids photocatalytic activities of In_2O_3-M since the adsorption rate is enhanced.

4.4.2 N_2 adsorption-desorption analysis of Ta/WO_3 and Nb/WO_3 nanostructures

The nitrogen adsorption-desorption isotherms of undoped WO_3 which exhibit a type-IV hysteresis loop is depicted in Figure 4.13. However, 4.14 and 4.15 shows a type-III isotherms of the Nb-doped and Ta-dope WO_3 nanomaterials, with hysteresis loops originating from the small slit-shapes pores. The type of loops is the confirmation of presence of mesopores in the as-obtained materials. The BET specific surface areas of the Ta-doped and Nb-doped WO_3 materials were estimated to be 46.4 and 55.1 m^2/g respectively. The BJH volume and pore sizes distribution were also examined (Table 4.2). Significant increase in the specific surface areas as a result of doping were observed. This can enhance photocatalytic behavior of the material.

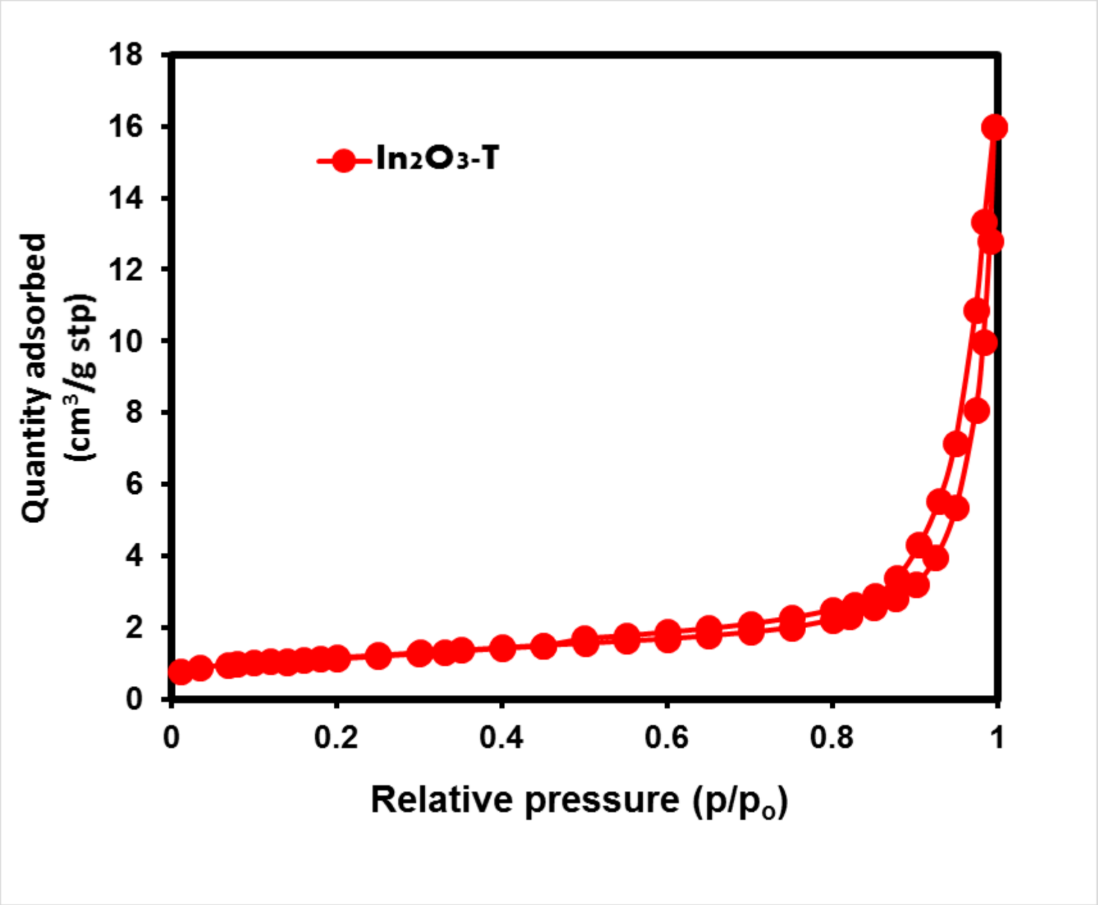

Figure 4.10: N_2 adsorption-desorption isotherm of as-synthesized In_2O_3-T

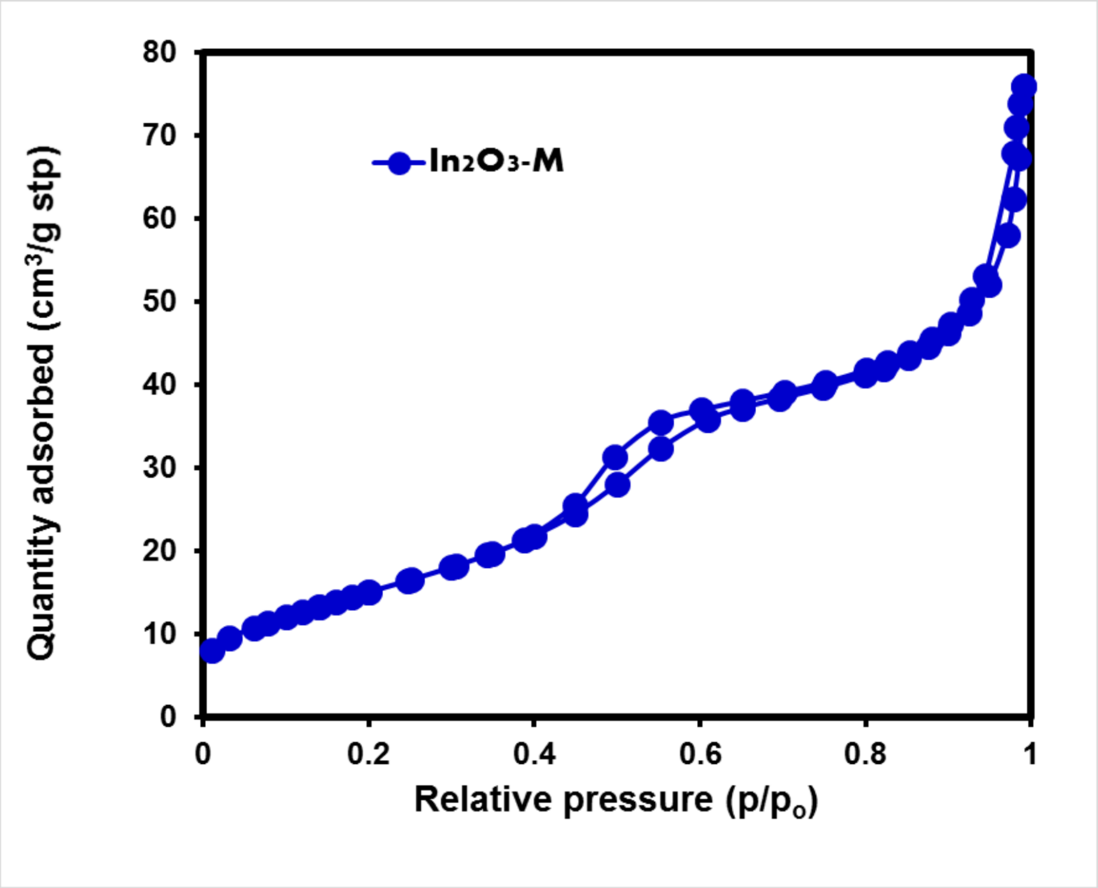

Figure 4.11: N_2 adsorption-desorption isotherm of as-synthesized In_2O_3-M

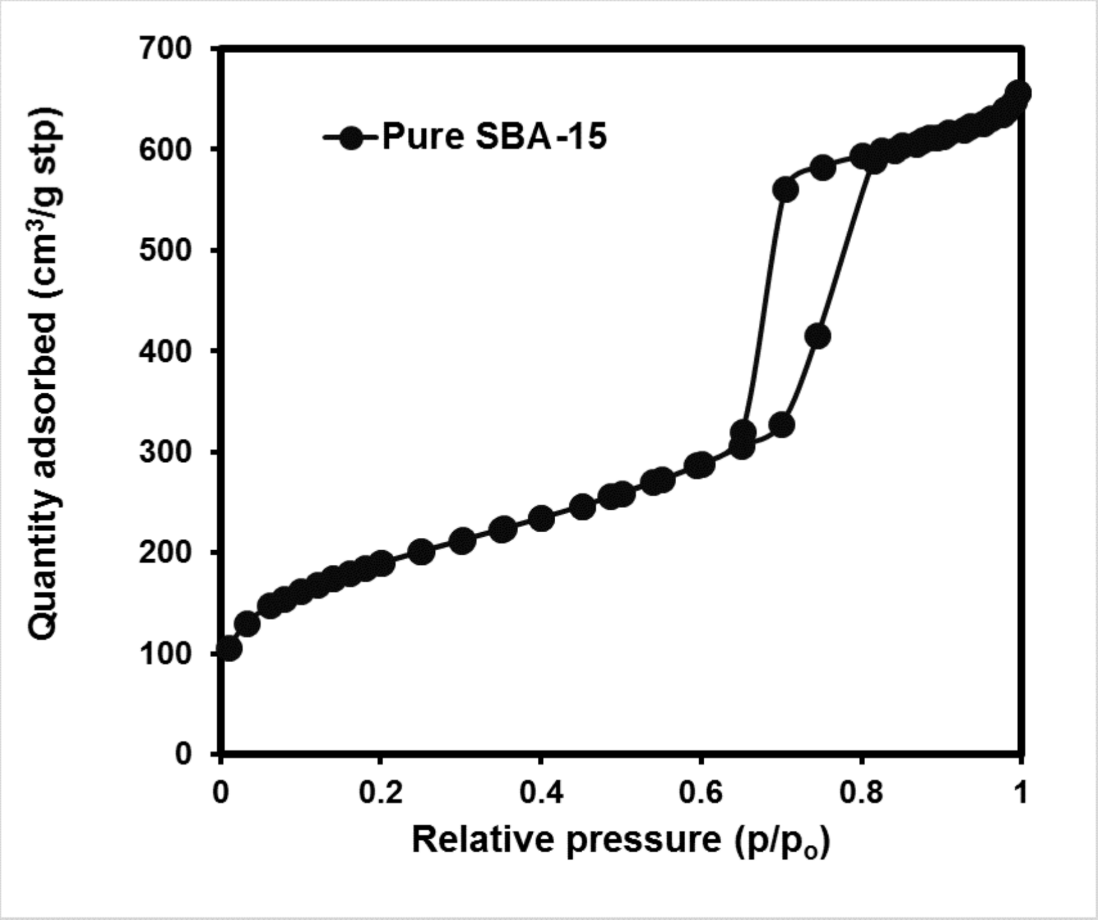

Figure 4.12: N_2 adsorption-desorption isotherm of SBA-15

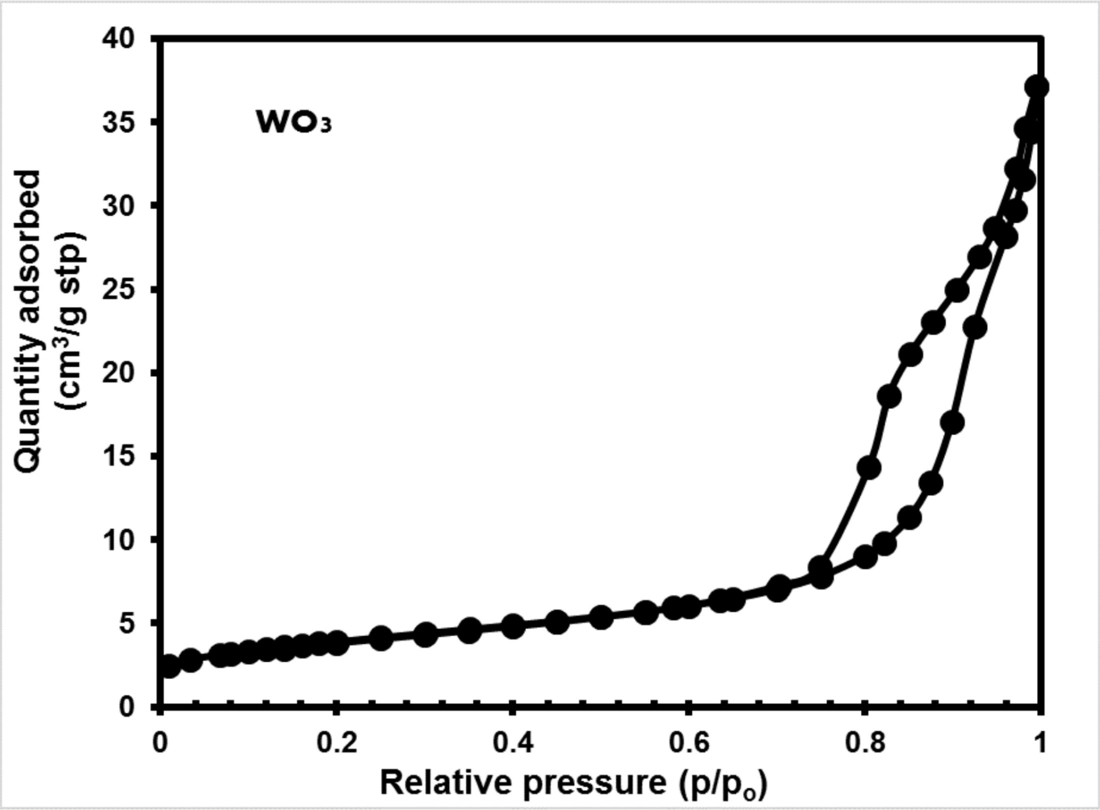

Figure 4.13: N_2 adsorption-desorption isotherm of as-synthesized WO_3

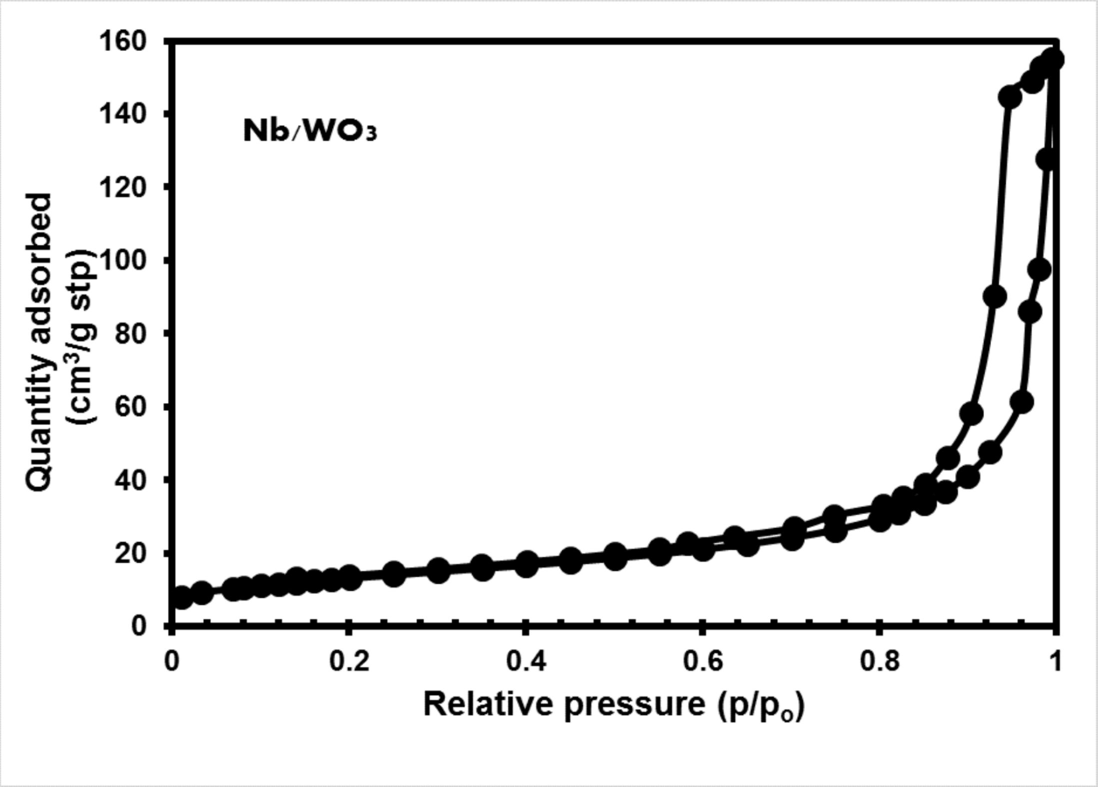

Figure 4.14: N_2 adsorption-desorption isotherm of as-synthesized Nb/WO_3

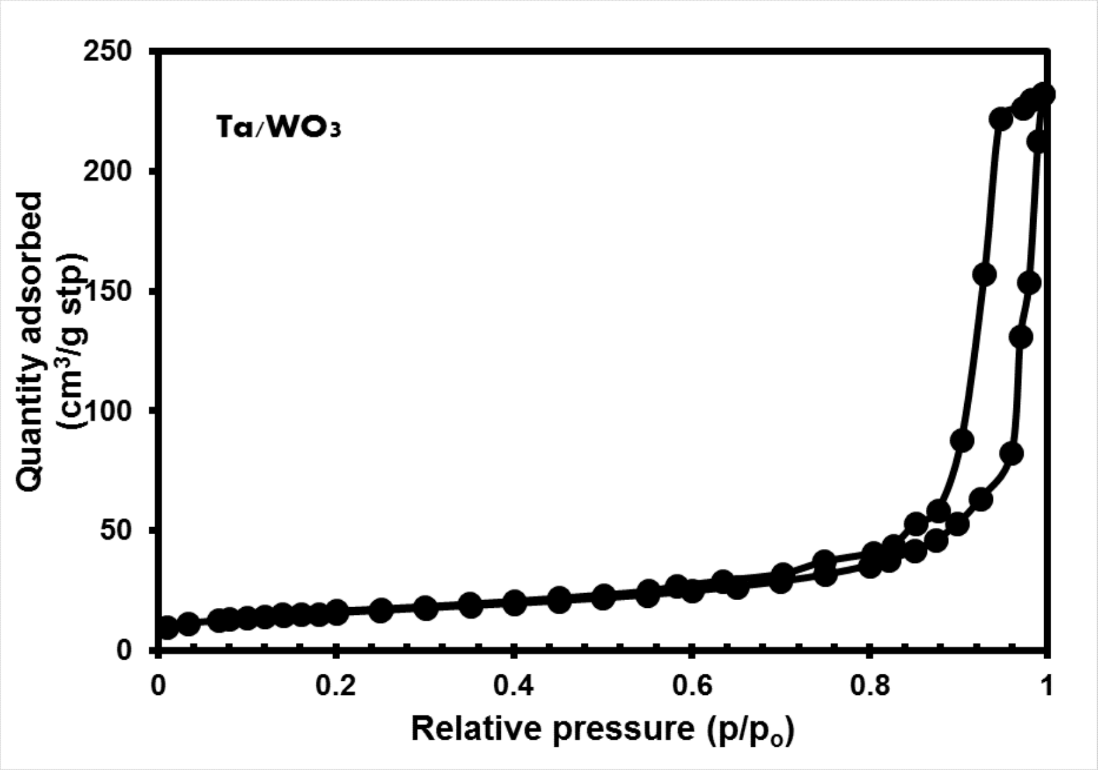

Figure 4.15: N_2 adsorption-desorption isotherm of as-synthesized Ta/WO_3

Table 4.2: List of estimated BET specific surface area, BJH pore volume and pore sizes for each nanocatalyt

S/N	**Material**	**BET surface area** ($m^2 g^{-1}$)	**BJH pore volume** ($m^3 g^{-1}$)
1	SBA-15	664	1.1
2	WO_3	13.4	0.058
3	In_2O_3-T	4.01	0.024
4	In_2O_3-M	56.0	0.12
5	MIW-1	4.27	0.038
6	MIW-2	9.69	0.051
7	MIW-3	22.7	0.21
8	Ta/WO_3	46.4	0.24
9	Nb/WO_3	55.1	0.36

4.5 Analysis of optical properties the materials

UV-visible absorption spectra of the synthesized materials were obtained and used to estimate the absorption edges as well as the band gaps of the samples. The Tauc plots were obtained for each sample to estimate their respective band gaps by using the Equations 3.8 and 3.9. Photoluminescence spectra were also recorded for the materials. The summary estimated band gap energies and absorption edges for each material are given in Table 4.3.

4.5.1 UV-visible absorption analysis of In_2O_3-T and In_2O_3-M nanocrystals

The band gap energy (E_g) of the semiconducting material is so important for any application including photocatalysis. In order to find the band gap energy of the materials, the reflectance spectrum was carried out and was transformed into Kubelka- Munk function [111, 112] which is expressed as in the Equation3.9. It is clear from the expression of Kubelka- Munk function that it is directly related to the absorbance and hence this function can very well be used in the Tauc plot in the place of absorbance to find the band gap energy of the material. Figure 4.16 shows the absorption spectra in terms of Kubelka Munk function for In_2O_3-T and In_2O_3-M, where it is quite obvious that the absorption in the visible region more for In_2O_3-T than In_2O_3-M (shown in the dashed box). The insets in Figure 4.16 contain the Tauc plots of In_2O_3-T and In_2O_3-M from which the band gap energies forIn_2O_3-T and In_2O_3-M were estimated to be $\sim$ 3.30 and $\sim$ 3.10 eV respectively.

4.5.2 UV-visible absorption analysis of WO_3 and In_2O_3-WO_3 nanocomposites

Figure 4.17 depicts the UV-visible absorption spectra of the materials WO_3 MIW-1 MIW-2 and MIW-3 and Tauc plots for WO_3 and MIW-3. The spectra of the In_2O_3-T incoporated WO_3 show red shift in the absorption edge of the materials from longer to shorter wavelengths thereby resulting in increase in the band gap and consequently possibility of reduction in the electron-hole pair recombination. The absorption edge of WO_3 is approximately 450 nm. MIW-3 shows most notable, but slight, wavelength shift to 440 nm. The values of the band gaps range from 2.88 eV to about 3.10 eV. Variation in the band gap can be accounted for by quantum confinement of the particles as their sizes reduce based on the reaction conditions applied during the samples preparation [77, 113]. Introduction of the indium oxides also inevitably results in new crystal defects, such as dislocations and stacking faults, which would lead to the formation of different forms of localized states in the band gap of WO_3 and change of band gap [114].

4.5.3 UV-visible absorption analysis of Ta/WO_3 and Nb/WO_3 nanostructures

The room temperature UV-visible absorption spectra and the Tauc plot of the Ta- and Nb-doped WO_3 are shown in Figure 4.18. Red shift in band gap transition and the absorption edge to the longer wavelength are observed the spectra of the doped materials. Equations 3.8 and 3.9 were used to determine the band gap of the semiconducting materials. The values of the band gap energies of Ta/WO_3 and Nb/WO_3 are 3.20 and 2.60 eV respectively. Doping with Nb narrowed the band gap of WO_3 while it was slightly widened by Ta-doping. This variation in band gaps of WO_3 which is reportedly an n-type semiconductor with band gap values ranging from 2.6 eV to 3.2 eV [77, 116] can be attributed to two possible reasons; change in the particle sizes and defects due to addition of dopant.

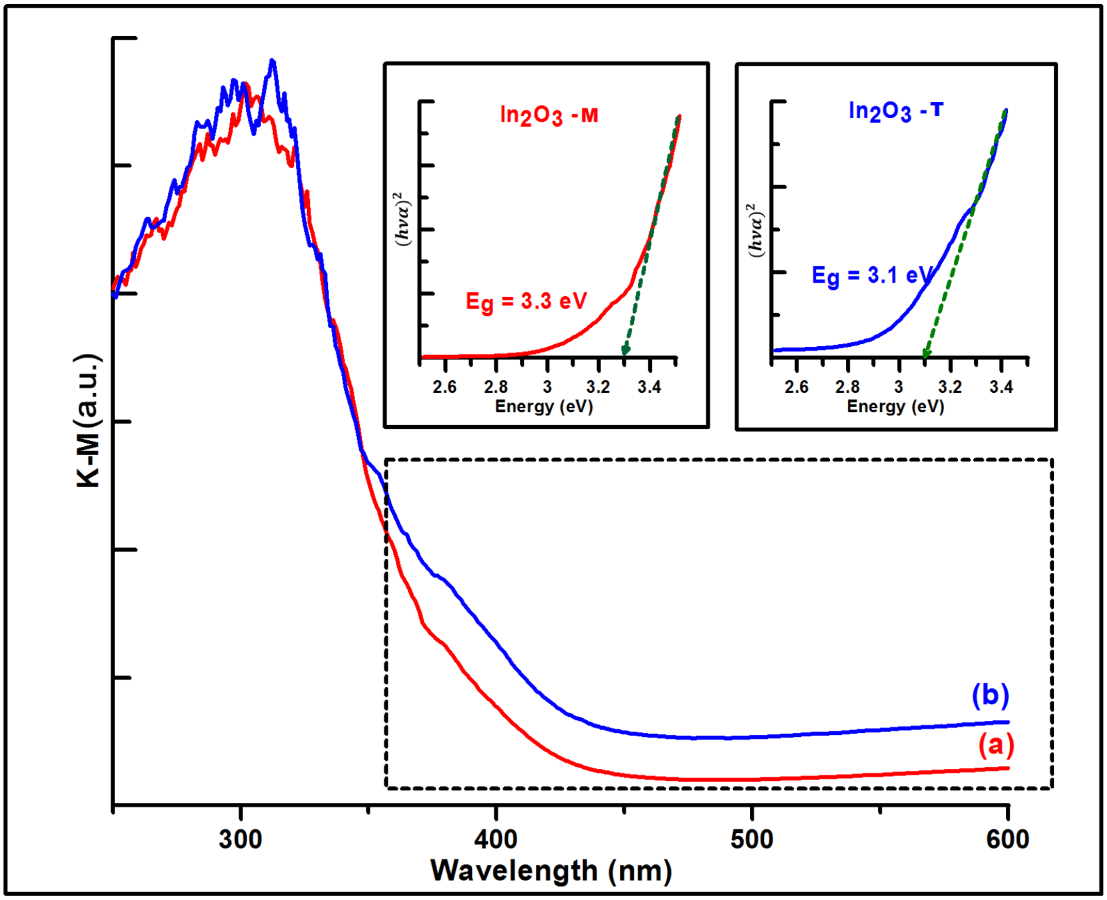

Figure 4.16: UV-vis absorption spectra represented as Kubelka- Munk function for In_2O_3-T and In_2O_3-M semiconductor nanocatalysts. The inset contains Tauc plots and band gap energies

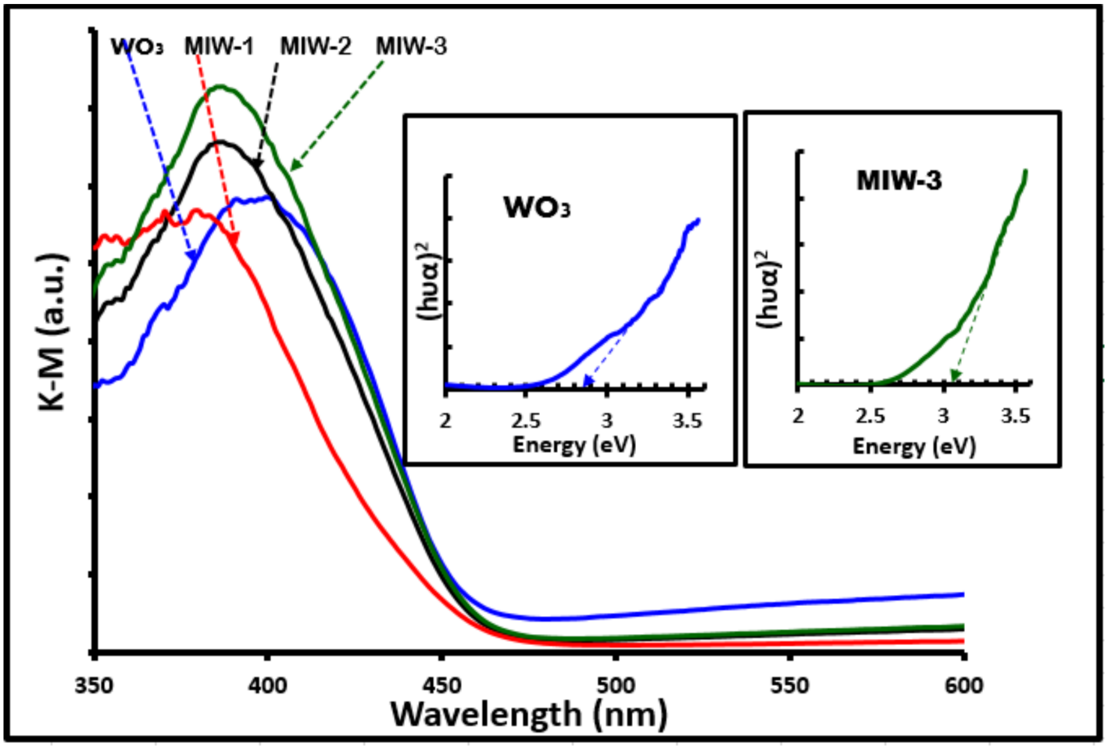

Figure 4.17: UV-vis absorption spectra represented as Kubelka- Munk function for WO_3 and In_2O_3-WO_3 semiconductor nanocatalysts. The inset contains Tauc plots and band gap energies for WO_3 and MIW-3

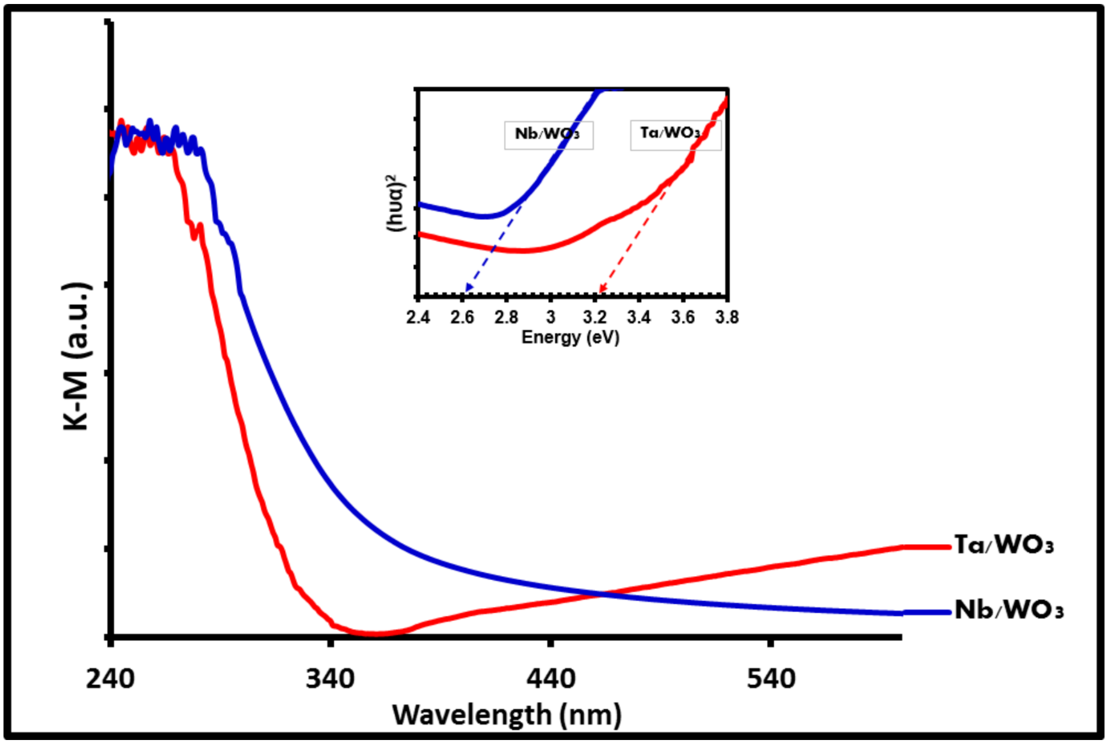

Figure 4.18: UV-vis absorption spectra represented as Kubelka- Munk function for Ta/WO_3 and Nb/WO_3 semiconductor nanocatalysts. The inset contains Tauc plots and band gap energies

Table 4.3: Estimated band gaps of the nanomaterials

S/N	**Material**	**Band gap (eV)**
1	WO_3	2.86
2	In_2O_3-T	3.15
3	In_2O_3-M	3.10
4	MIW-1	3.05
5	MIW-2	3.06
6	MIW-3	3.07
7	Nb/WO_3	2.60
8	Ta/WO_3	3.20

4.5.4 Photoluminescence analysis of In_2O_3-T and In_2O_3-M nanocrystals

Figure 4.19 depicts the room temperature photoluminescence spectra for the as-prepared mesoporous In_2O_3-T and In_2O_3-M nanostuctures with 350 nm excitation wavelength. On comparison of the PL spectra in Figure 4.19, the non-templated In_2O_3-T does not show any substantial PL emission where in the case of ordered mesoporous In_2O_3-M, a broad PL peak centered on 443 nm is observed. The enhanced PL emission of the mesoporous In_2O_3-M might be due to the defects [114]. In general, emissions can be divided into the near band-edge (NBE) and deep-level (DL) emissions. While the NBE emissions can be facilitated by the high crystal quality and quantum confinement effect, the DL emissions can be favored by low crystallinity or structure defects [114]. As discussed before, the XRD pattern of mesoporous In_2O_3-M indicated that there are some induced defects in the ordered material due to the presence of SBA-15 template and theses defect centers luminance through the electron phonon coupling rather than due to the electron- hole recombination and this explains the enhanced PL emission in the case of mesoporous In_2O_3-M compared to In_2O_3-T.

4.5.5 Photoluminescence analysis of WO_3 and In_2O_3-WO_3 nanocomposites

Another way of explaining catalytic activities of the MIW nanocomposite is the photoluminescence (PL) emission spectra of the materials shown in Figure 4.20.

The PL emission spectra have been widely employed in explaining some properties of semiconductor materials. Examples of the properties are the process of electron-hole recombination, efficiency of charge carrier transfer, migration and trapping. It is known that PL emissions result from recombination process between excited electrons and holes, thus smaller rate of recombination between electrons and holes under irradiation may be signified by lower PL relative intensity [118]. The Figure 4.20 depicts the PL spectra of WO_3 and its composites with the two fundamental emission peaks centered at around 417 nm and 440 nm respectively and WO_3 displaying the highest peak intensity. The high emission peak of WO_3 implies that it exhibit most efficient radiative recombination among the materials. It is observed that the PL intensities decreased with addition of In_2O_3, as MIW-1, MIW-2 and MIW-3 each shows significant reduction respectively. This could be a reason for superior catalytic activity of MIW-3 since it indicates lower recombination rate of the photoexcited charge carriers.

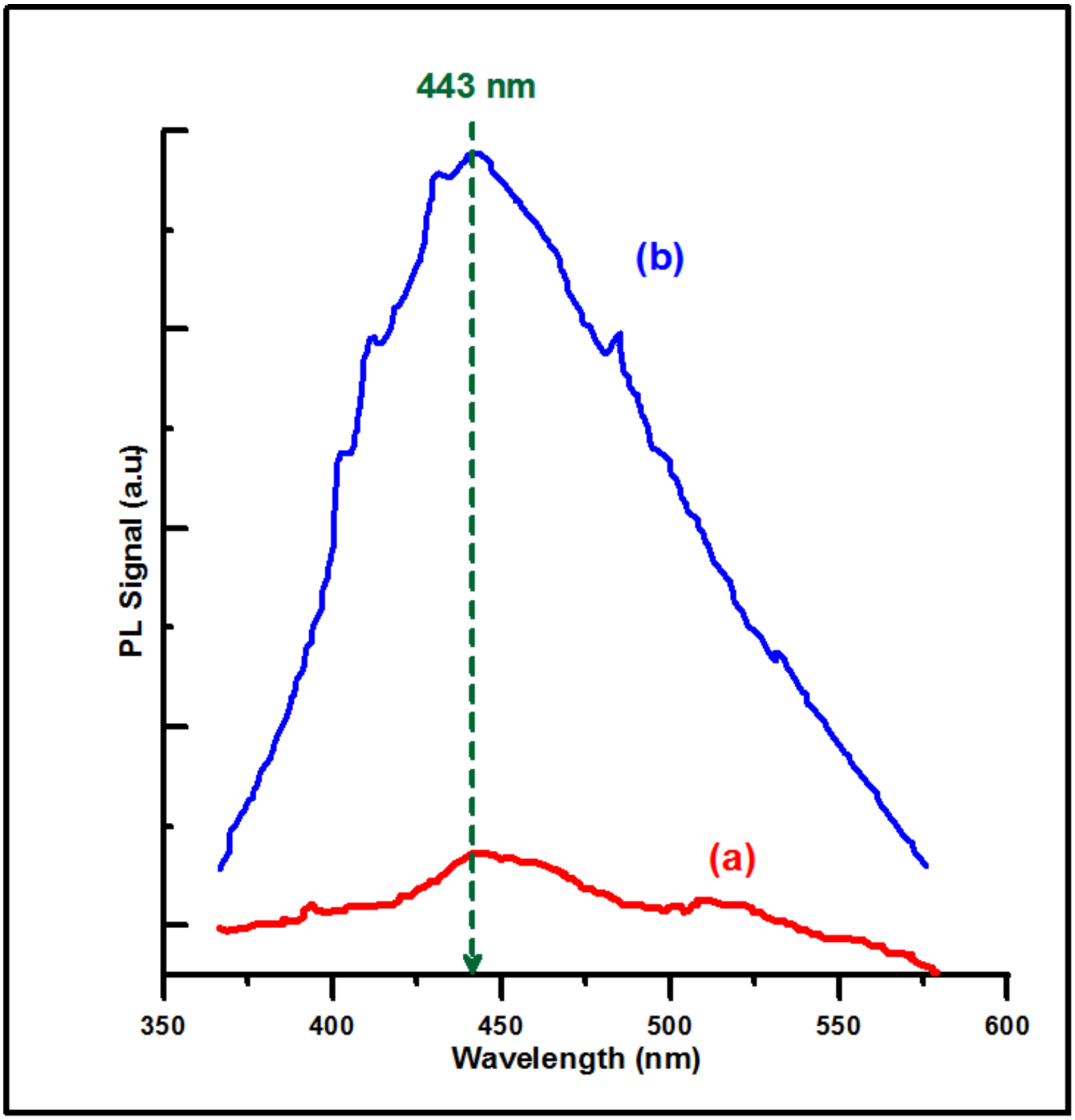

Figure 4.19: PL spectra of (a) In_2O_3-M and (b) In_2O_3-T nanocatalysts measured at room temperature

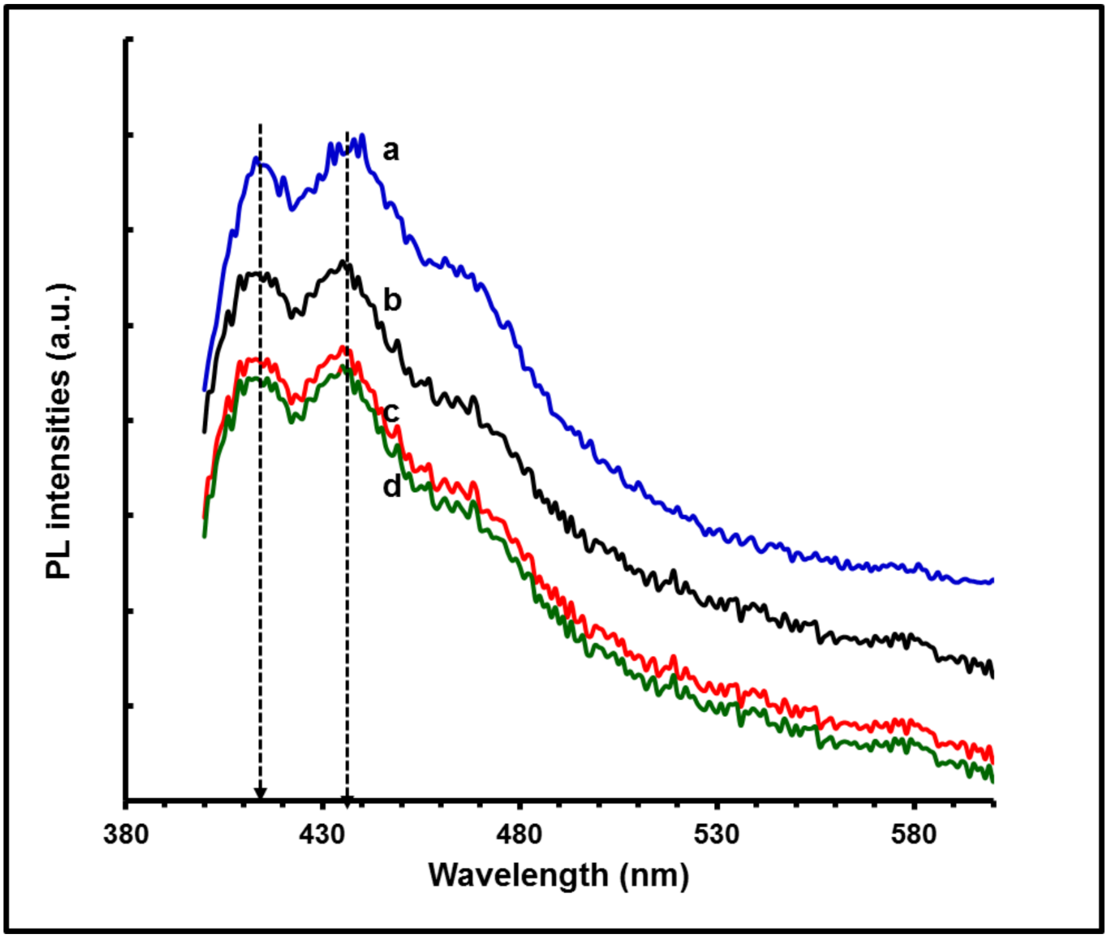

Figure 4.20: PL spectra of (a) WO_3 (b) MIW-1 (c) MIW-2 and (d) MIW-3 nanocomposites measured at room temperature

4.6 Analysis of chemical composition of the composite materials

Study of elemental composition and electronic state of the constituent elements were carried out for the composite and doped materials by using x-ray photoelectron spectroscopy (XPS).

4.6.1 XPS analysis of WO_3 and In_2O_3-WO_3 nanocomposites

The chemical states of W, In and O in the as-prepared In_2O_3-WO_3 nanocomposites were determined by XPS. XPS spectrum of the tungsten core level (W4f) in the undoped WO_3 sample is given by Figure 4.21. The two peaks at 35.2 and 37.2 eV in the spectrum can be attributed to $W4f_{7/2}$ and $W4f_{5/2}$, respectively, which are in good agreement with the values reported elsewhere [119]. It can be concluded that all tungsten atoms are in the +6 oxidization state since the two peaks are well separated without any shoulder. The typical XPS spectra of the sample MIW-3 were studied with the presence of In, W and O suggested. Two peaks belonging to oxygen appeared at 530.4 and 530.8 eV are shown in Figure 4.22, they can be assigned to the lattice oxygen in In_2O_3 and WO_3 species [113, 120]. Figure 4.23 depicts the spectrum of W 4f with two evident peaks at 35.3 and 37.4 eV that can be attributed to $W4f_{7/2}$ and $W4f_{5/2}$ of WO_3 respectively [77, 120]. Separation of these two peaks without shoulder indicates the presence of W^{6+} state for all tungsten atoms [77]. In Figure 4.24, doublet peaks belonging to $In3d_{3/2}$ and $In3d_{5/2}$ were found at binding energies 452.2 and 444.6 eV [120]

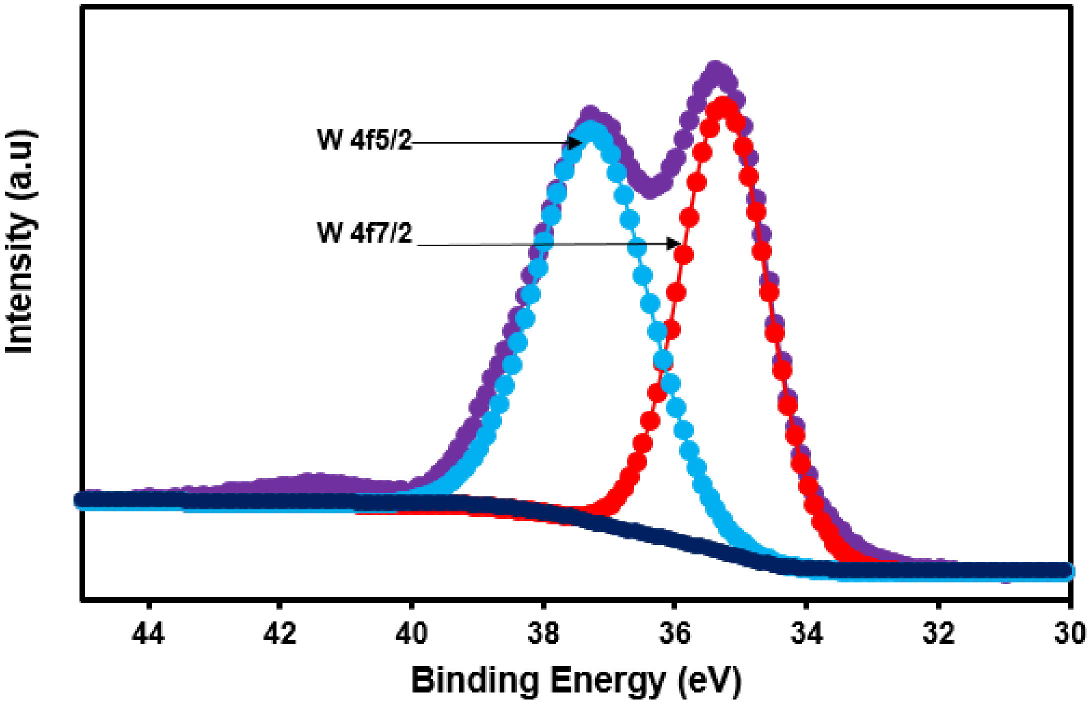

Figure 4.21: XPS spectra of undoped WO_3 sample

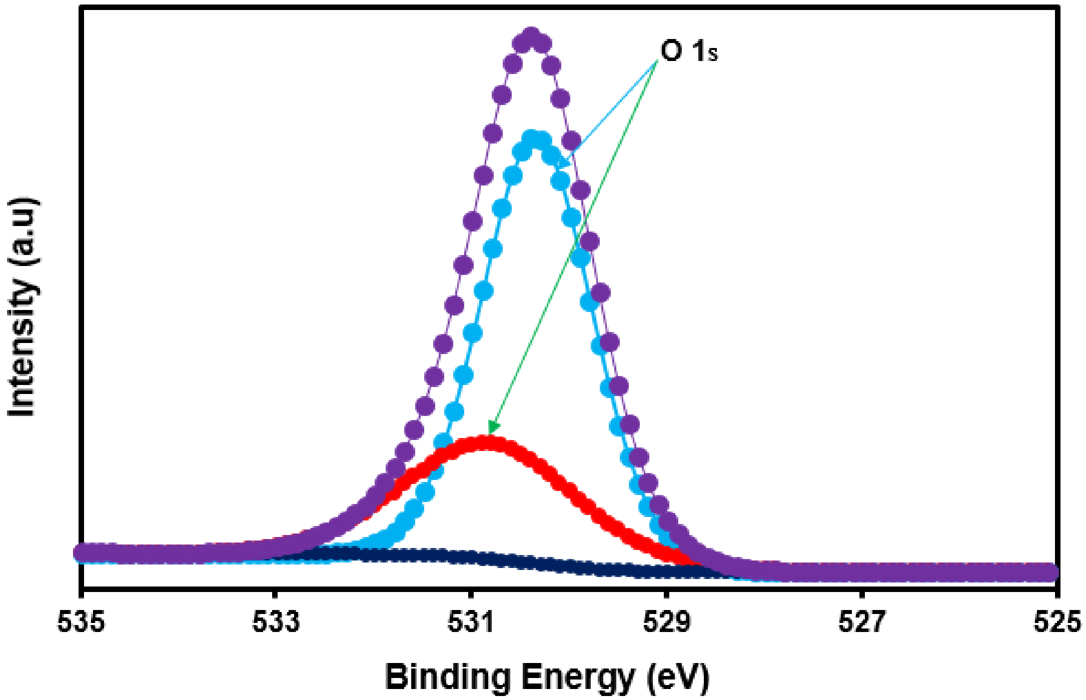

Figure 4.22: XPS spectra of O 1s in In_2O_3-WO_3 nanocomposites

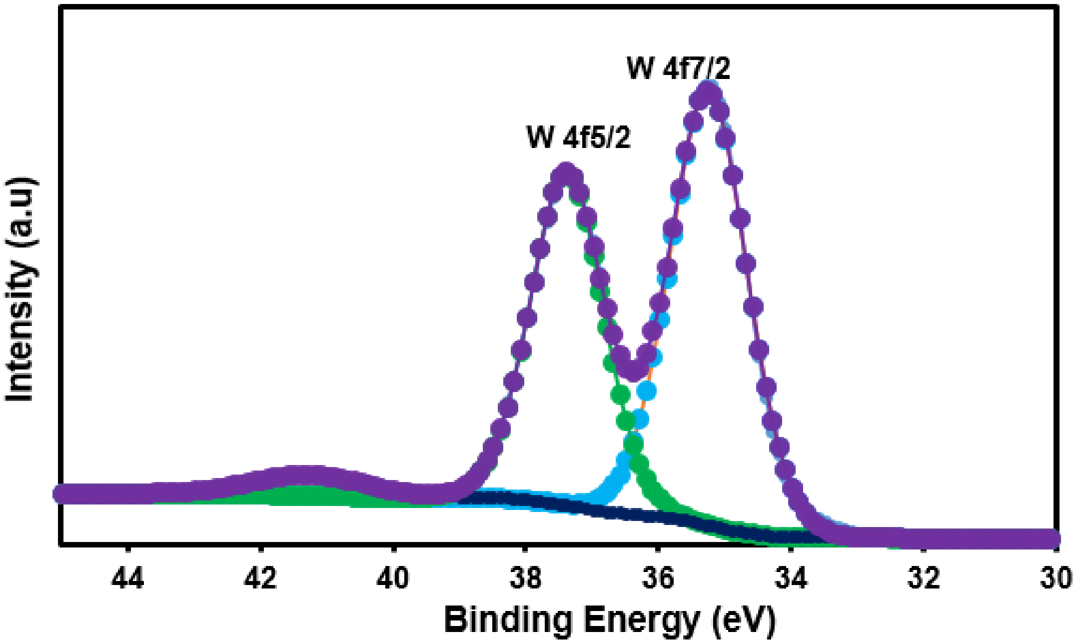

Figure 4.23: XPS spectra of W 4f in n_2O_3-WO_3 nanocomposites

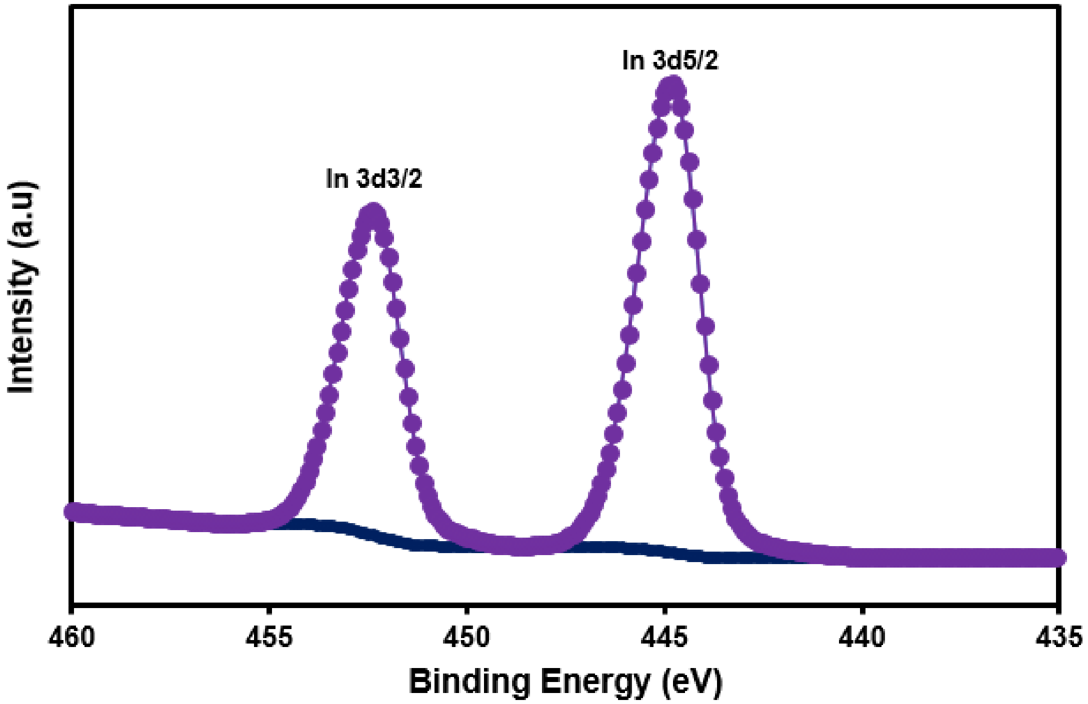

Figure 4.24: XPS spectra of In3d in In_2O_3-WO_3 nanocomposites

4.6.2 XPS analysis of Ta/WO_3 and Nb/WO_3 nanostructures

XPS analysis were used to study the chemical states of W, Ta and Nb in the as-synthesized sample. Figure 4.25 shows the XPS spectrum of W 4f in the Nb-doped WO_3 sample, where a doublet that could be attributed to $W4f_{7/2}$ and $W4f_{5/2}$ appeared at the electron binding energies of 34.9 and 37.0 eV respectively [77]. The doublet can be identified as W^{5+} oxidation state. Similar doublet of W^{5+} is identified in the spectrum (Figure 4.26) of Ta-doped WO_3 at the electron binding energies of 34.7 and 36.9 eV [121, 122]. Figure Figure 4.27 is the XPS spectrum of Nb 3d with well-distinguished doublet peaks that can be assigned to $Nb3d_{3/2}$ and $Nb3d_{5/2}$ observed at binding energies 206.9 and 209.7 eV [77] respectively. A similar version of this can be seen in the spectrum (Figure 4.28) of Ta 4f with two separate doublets appearing at 25.4, 25.7, 27.6 and 28.2 eV. Each of the binding energies of Nb 3d and Ta 4f describes +5 oxidation state for the Nb [77, 123] and Ta [124] ions respectively. From these results, it can be concluded that the chemical compositions in doped WO_3 samples are WO_3, WO_{3-x} and either Ta_2O_5 or Nb_2O_5. However, the relative amount of Ta_2O_5 or Nb_2O_5 in the resulting products is below the detection limit of the XRD analysis.

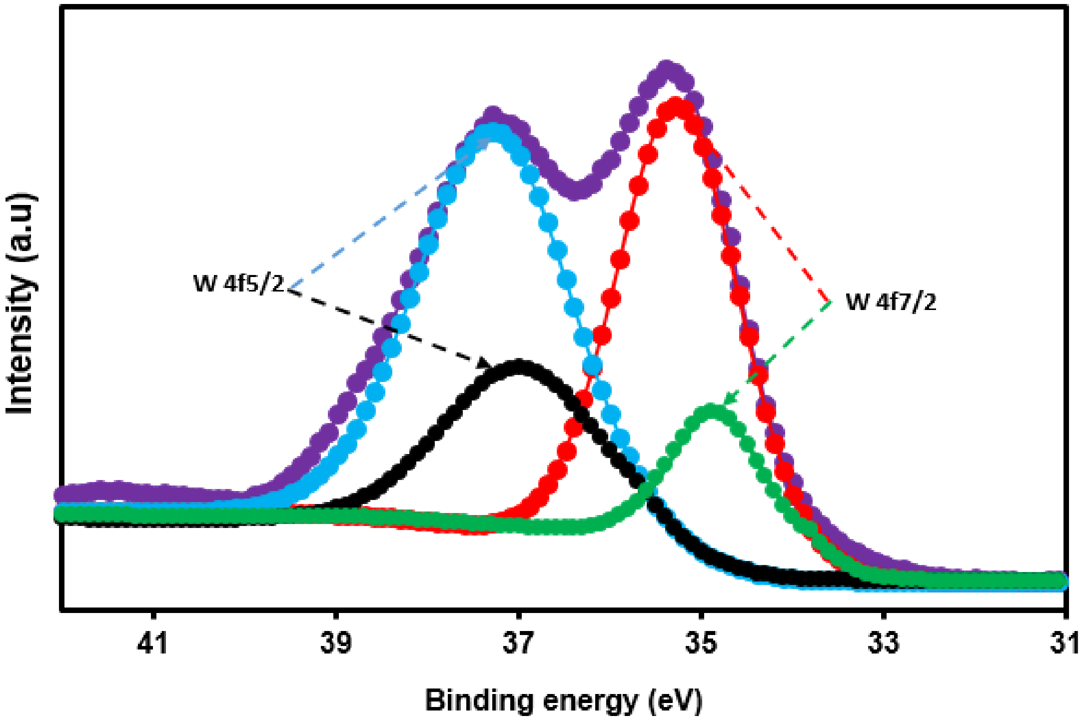

Figure 4.25: XPS spectra of W 4f in Nb/WO_3 nanocatalyst

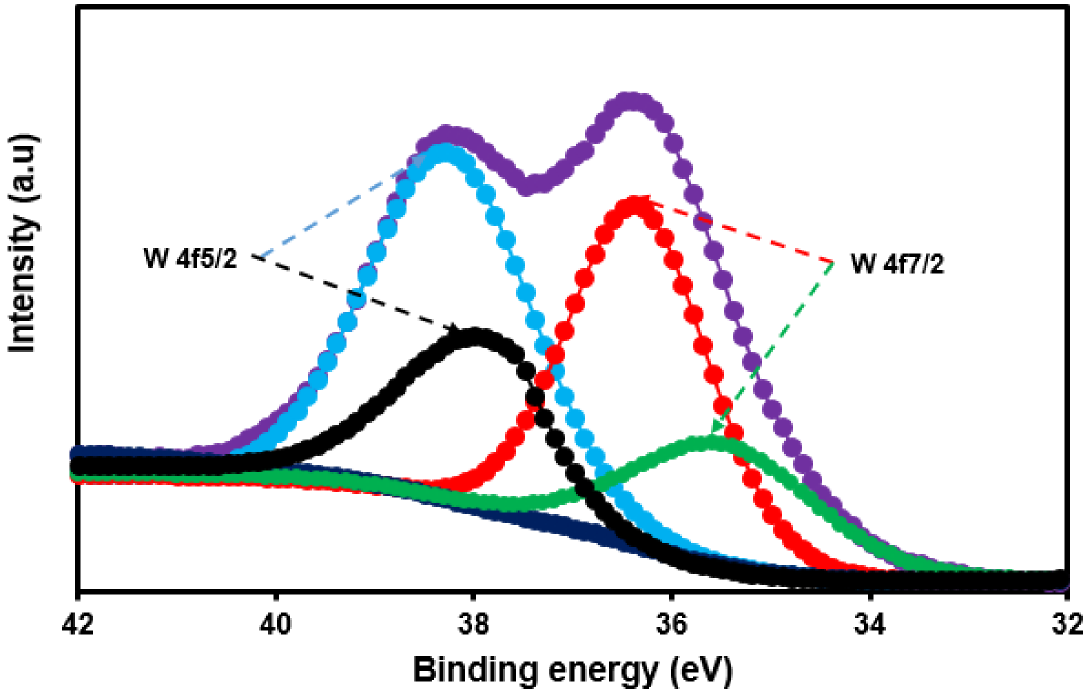

Figure 4.26: XPS spectra of W 4f in Ta/WO_3 nanocatalyst

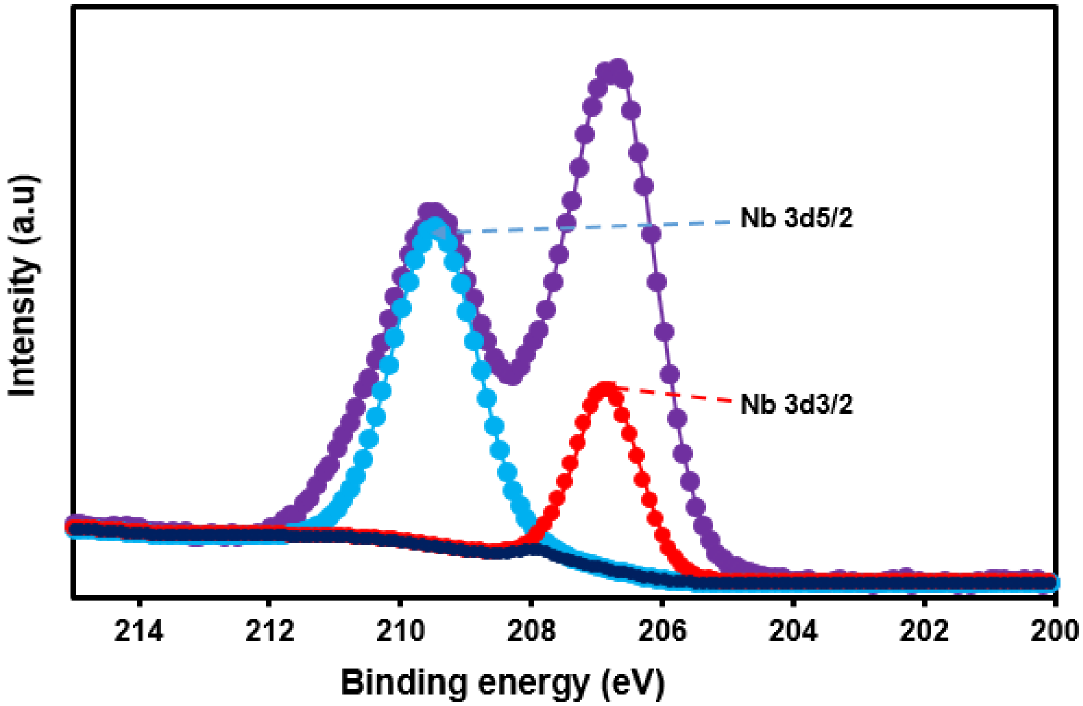

Figure 4.27: XPS spectra of Nb3d in Nb/WO_3 nanocatalyst

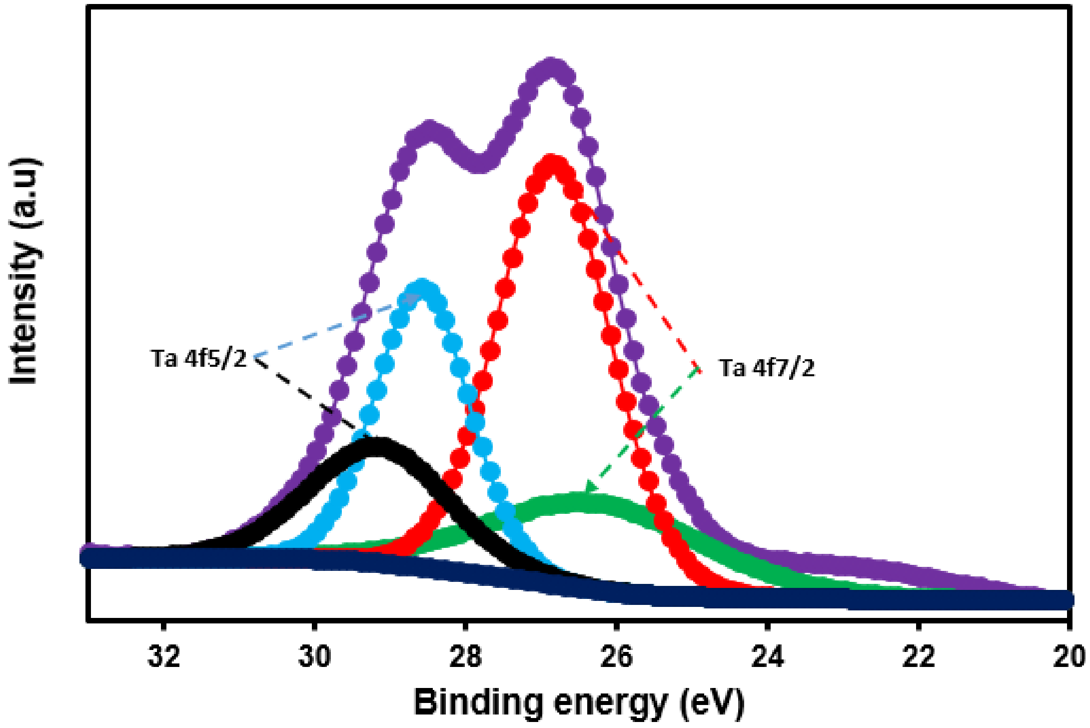

Figure 4.28: XPS spectra of Ta 4f in Ta/WO_3 nanocatalyst

CHAPTER 5

APPLICATION IN LASER INDUCED PHOTOASSISTED REDUCTION OF CO_2 TO LOW CARBON FUEL

In this chapter we discuss results of photoctalytic activities of the synthesized nanomaterials in photoreduction of CO_2 to methanol. The selected nanomaterials for this application are In_2O_3-T, In_2O_3-M, WO_3, MIW-1, MIW-2 and MIW-3, since these nanocrytals and nanocomposites showed enhanced photocatalytic activities as discussed later in this chapter.

Laser is a monochromatic source of light, it is coherent with very high power. Probability of photonic absorption by semiconductor photocatalysts, in laser, is higher than in broad spectra sources such as lamps where most of the emission wavelengths lie outside the band gap of the catalyst [110, 125]. In this work, conversion of greenhouse gas to value-added low carbon fuel has been investigated with 266 nm and 355 nm pulsed laser beam as irradiation source the catalysts. Detailed description of the laser parameters and conditions used for these experiments were given chapter three.

5.1 Calibration of GC for methanol quantification

Verification and quantification of methanol produced from CO_2 reduction over the synthesized catalysts were carried out by using gas chromatography. Methanol standard solution were prepared to identify the methanol retention time. It was 8.32 min as depicted in Figure 5.1

In order to quantify the methanol produced out of CO_2 reduction, we established a calibration curve that relates the concentration of methanol with the area of the concerned GC peak. The retention time of the GC for a particular product depends on the GC parameters and the GC column used, and in our case the retention time for methanol standard was found to be at 8.32 minutes. The standard calibration samples of a particular concentration were prepared with utmost care from the stock solution and after every GC analysis of a particular sample, blank GC runs were carried out to deplete the traces of methanol in the GC column from previous run. Figure 5.1 is the chromatogram for a set of methanol standards of known concentrations (31, 63, 78, 156, 313, 625 and 1563 mol per 100 mL of water) and all the GC peaks are centered on the retention time of 8.32 minutes. Figure 5.2 shows variation of the peak areas and peak heights with the concentrations. Figure 5.3 is the linear calibration plot of the peak area versus methanol concentration in water, which can be used to find the unknown concentrations of methanol produced from the reaction

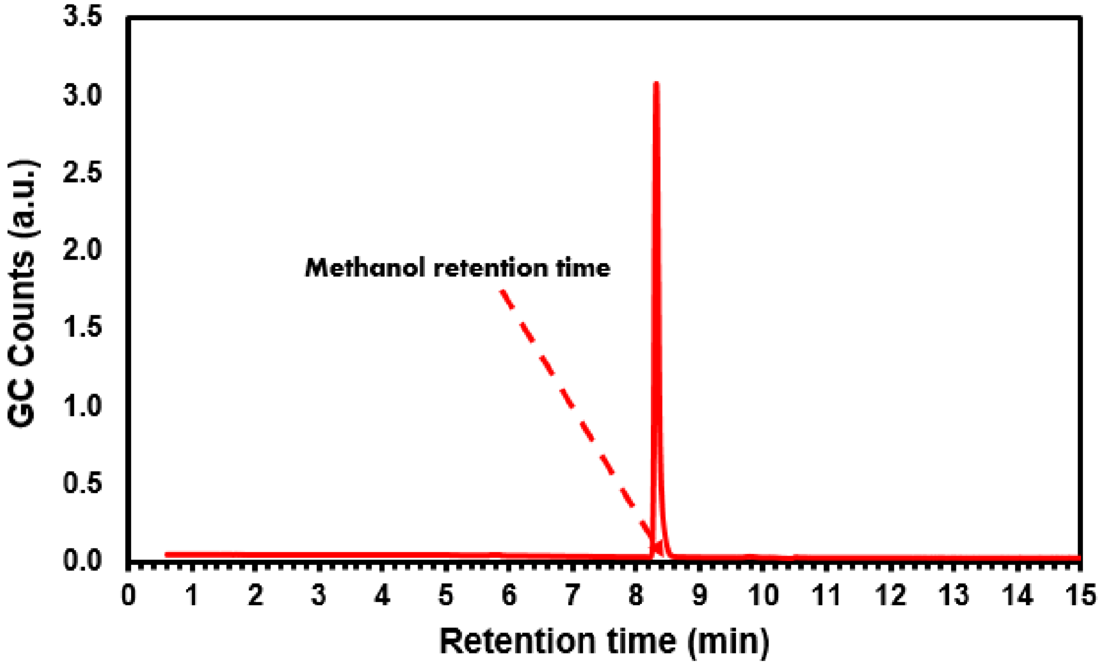

Figure 5.1: Position of GC peak for methanol standard used to identify the retention time and calibration

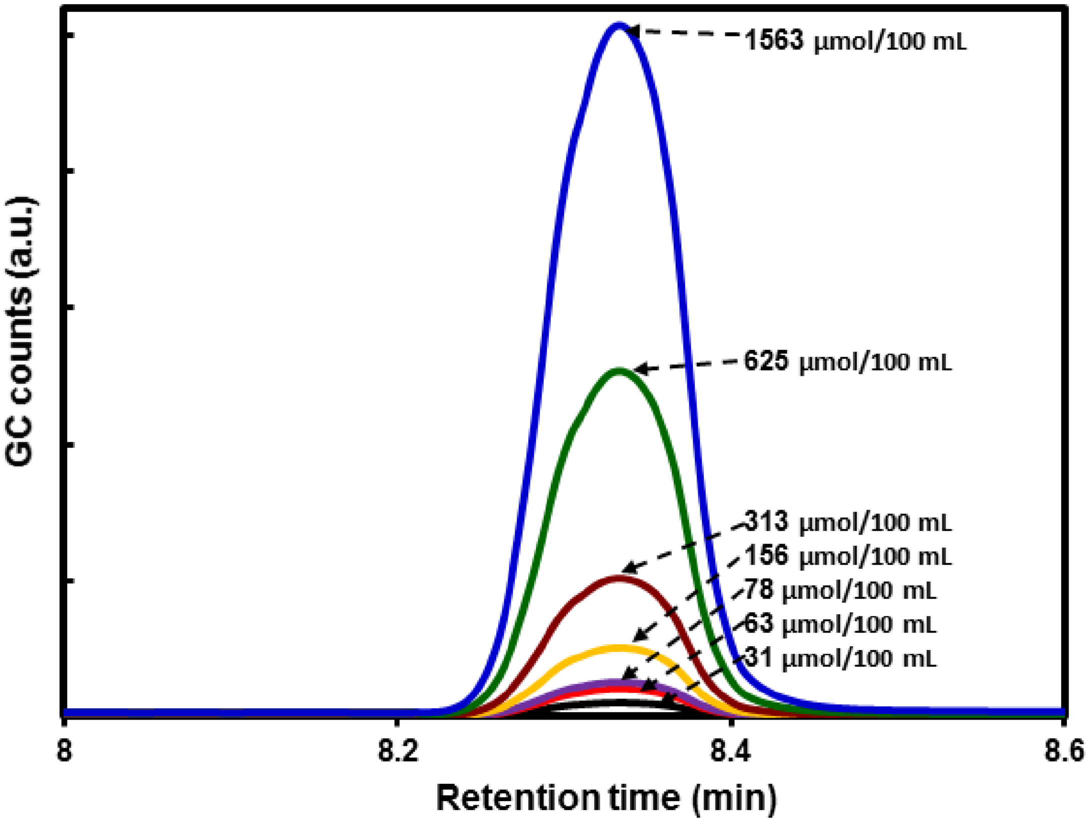

Figure 5.2: XGC chromatograms for increasing concentration of standard methanol

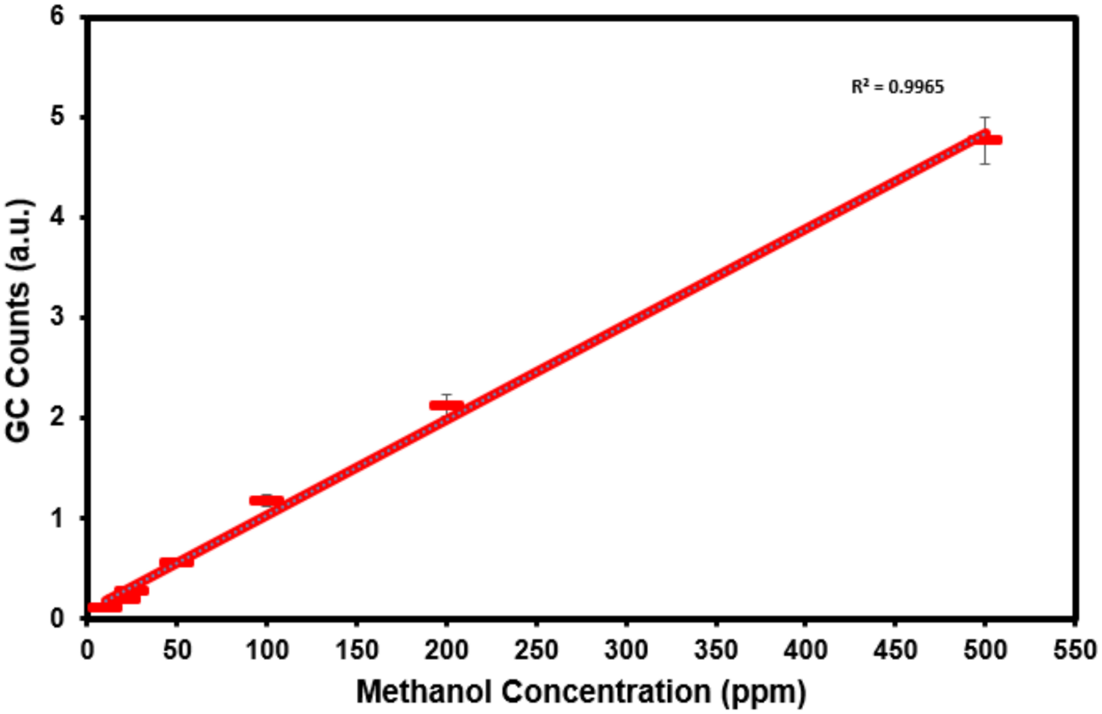

Figure 5.3: Calibration plot of GC counts versus concentration of standard methanol

5.2 Photoreduction of CO_2 to methanol over WO_3 and In_2O_3-WO_3 nanocomposites

The photocatalytic ability of the synthesized WO_3 nanoparticles, MIW-1, MIW-2 and MIW-3 nanocomposites in the CO_2 conversion to low carbon fuel were investigated, using water as hole scavenger and high power 266 nm laser as the irradiation source. As it is generally known, numbers of reaction products like formic acid, formaldehyde (HCHO), methane (CH_4), CO, methanol (CH_3OH), etc. can be obtained during CO_2 photoreduction process. Though we were selectively interested in methanol (CH_3OH) as the main product in this study, the pathways of CO_2 photoreduction are highlighted in chapter one with the corresponding reduction potentials.

Unlike the MIW nanocomposites, no notable product was obtained when pure $WO_3$was used as the catalyst. This is attributed to non-negative conduction band potential of the material. Table 5.1 shows the calculated conduction band (CB) edge and the valence band (VB) edge positions of WO_3 and In_2O_3 by using Equations 5.1 and 5.2 [126].

$$E_{CB} = X - E_C - \frac{1}{2}E_g \tag{5.1}$$

$$E_{VB} = E_g - E_{CB} \tag{5.2}$$

In the equations, X represent the absolute electronegativity of the semiconductor, E_C the energy of free electron on hydrogen scale (= 4.50 V) [140] and E_g is the semiconductor band gap. As shown in Table 5.1, the calculated valence band edge position (= +3.39 V vs NHE) of the pure WO_3 is high enough to initiate the water-hole reaction leading to formation of O_2 and H^+ but the calculated conduction band edge position (= +0.79 V vs NHE) is not sufficient for transformation of CO_2 to CH_3OH with H^+ and photogenerated electron, where the needed potential is negative order potential (= −0.38 V vs NHE). With this, photoreduction of CO_2 to methanol is not feasible over pure WO_3.

Typical GC peaks of methanol products for samples from CO_2 photoreduction over which catalyst, which was taken at regular interval, is depicted in Figure 5.4. The Figure shows growing of the peaks with irradiation time, which appears at the 8.32 min retention time. Methanol yield, in μmol per 100 mL of water, over WO_3, MIW-1, MIW-2 and MIW-3 are depicted in Figure 5.5. The methanol concentration increases with the irradiation time and reaches its maximum for all the tested catalysts after 60 min of irradiation and decline afterwards. It is worth noting that MIW-3 gives the best methanol yield among the four catalysts (WO_3, MIW-1, MIW-2 and MIW-3), this is likely due to reduced $e^- - h^+$ recombination when compared with other catalysts. Maximum methanol yields for each catalyst is listed in Table 5.2. This can also be accounted for by its highest In_2O_3 contents since In_2O_3 has sufficient band edges (- 0.42 eV vs NHE CB edge & + 1.98 eV vs NHE VB edge) for methanol formation as listed in Table 5.1.

Figure 5.6 depicts a schematic diagram of the mechanism for charge separation in the In_2O_3-WO_3 nanocomposites. When the nanocomposite material (MIW) is irradiated with light, photoelectrons from the conduction band of In_2O_3 will transfer into the conduction band of WO_3 nanoparticles. Also holes residing in the valence band of In_2O_3 will transfer into the valence band of WO_3. This process will reduce charge recombination effect to minimal, and also makes the photoelectrons from In_2O_3 and photo-holes from WO_3 structures available for photoreduction of CO_2 and photo-oxidation of water respectively.

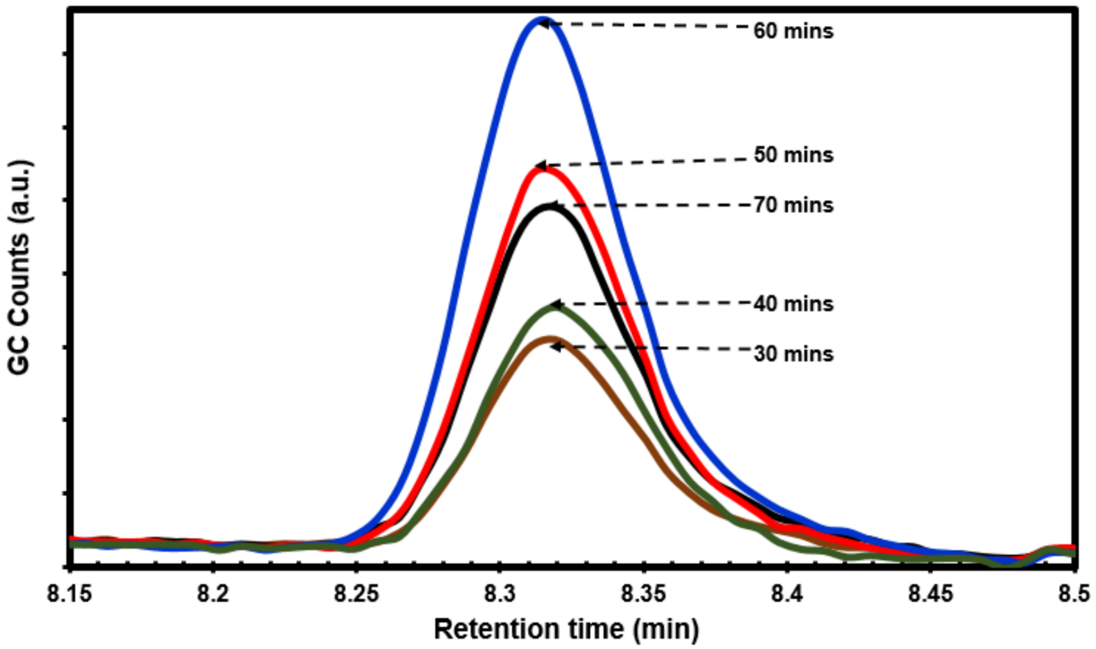

Figure 5.4: GC peaks of methanol from sample taken after 30, 40, 50, 60 and 70 min

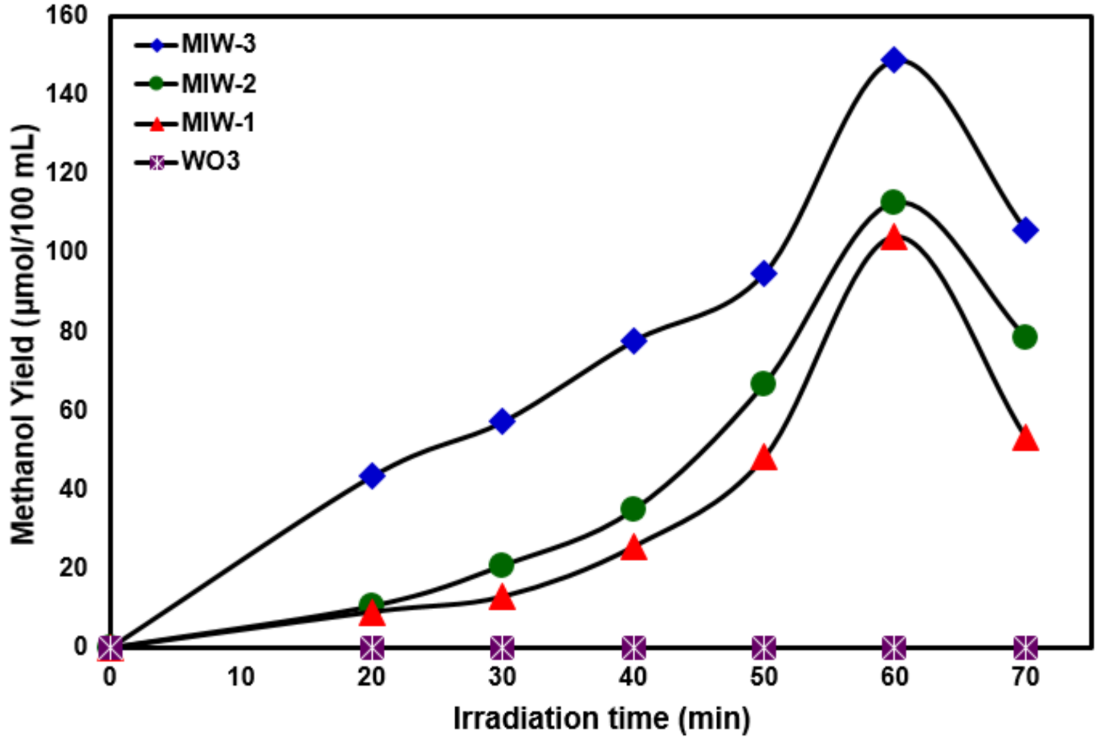

Figure 5.5: Plot of concentration of methanol produced against irradiation time with 266 nm laser

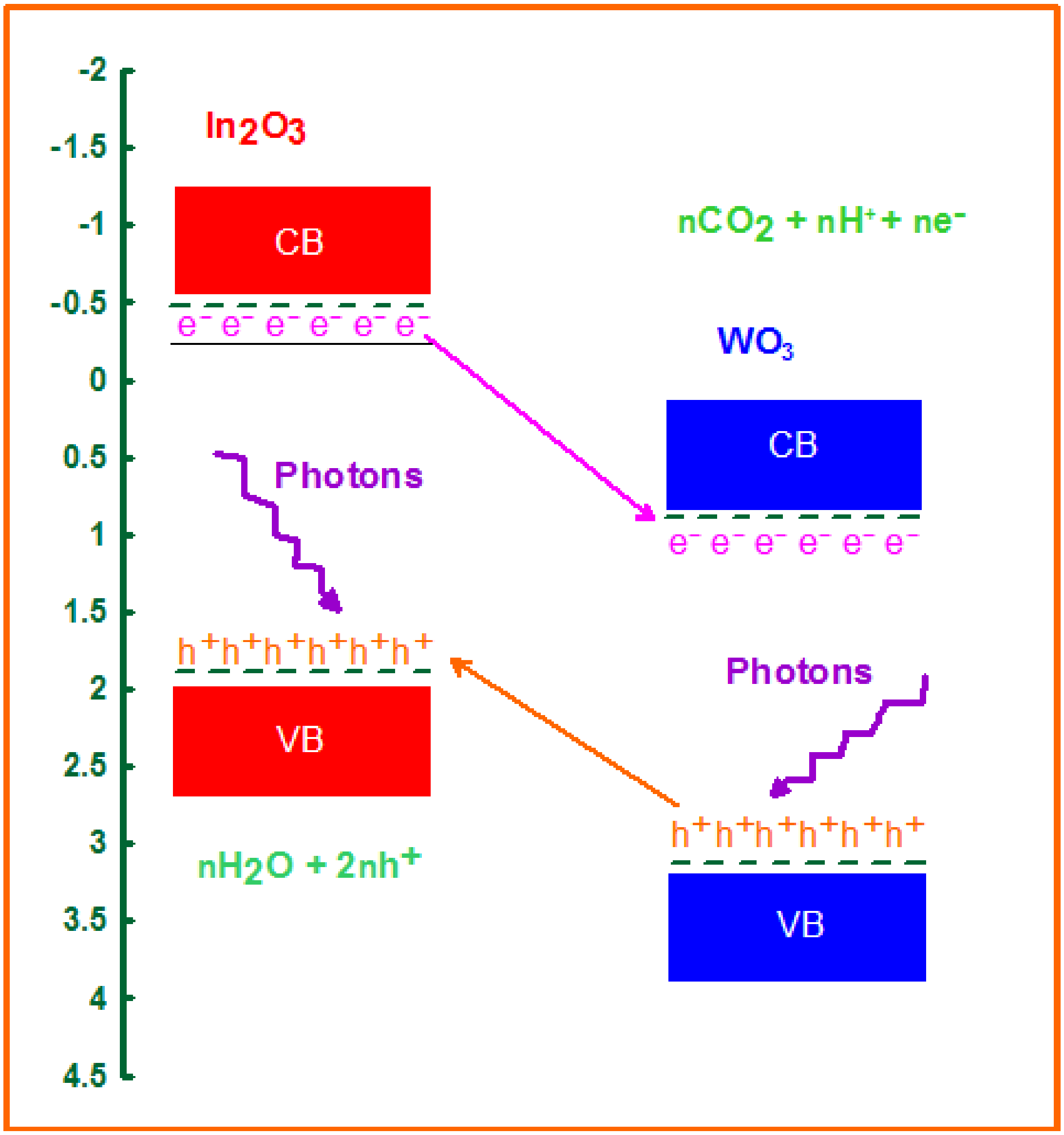

Figure 5.6: Schematic diagram for mechanism of enhanced photocatalytic activities for In_2O_3/WO_3 nanocomposites

Table 5.1: Electronegativity, calculated conduction band edges, valence band edges for the In_2O_3-T, In_2O_3-M and WO_3 nanocatalysts

S/N	**Conduction band edge (eV vs NHE)**	**Valence band edge (eV vs NHE)**	**Electronegativity X(eV)**
In_2O_3-T	-0.80	+2.35	5.28
In_2O_3-M	-0.77	+2.33	5.28
WO_3	+0.79	+3.39	6.52

Table 5.2: Maximum methanol yield, quantum efficiency and CO_2 conversion efficiency for the as-synthesized nanocatalysts

S/N	**Maximum methanol yield (μmol/100 mL)**	**Quantum efficiency (%)**	**Conversion efficiency (%)**
WO_3	-	-	-
MIW-1	104.3	1.6	8.3
MIW-2	112.8	1.8	8.9
MIW-3	148.8	2.3	11.8
In_2O_3-T	435.8	4.0	41.9
In_2O_3-M	481.4	4.5	46.8

5.3 Photoreduction of CO_2 to methanol over In_2O_3-T and In_2O_3-M nanocrystals

The synthesized non-templated In_2O_3-T and mesoporous In_2O_3-M nanocrystals were used as photo-catalysts for the production of methanol from photocatalytic reduction of CO_2 with 355 nm laser as the radiation source

The calculated VB and CB for In_2O_3-M are + 2.43 and -0.8 V vs NHE respectively and the same for In_2O_3-T nanocatalysts are +2.38 and - 0.77 V vs NHE as given in Table 5.1. This values satisfy the energy conditions that determines the suitability of the catalyst to carry out the photo reduction reaction. The proposed mechanism of reaction for photconversion of CO_2 to methanol by the In_2O_3 catalysts is depicted in Figure 5.7.

As the photocatalytic reduction of CO_2 to methanol proceeds in the reactor, The concentration of methanol produced increased up to 150 minutes of irradiation after which the methanol concentration starts to decrease. This reverse trend with prolonged irradiation time indicates some kind of competing back reaction or the photo-degradation of produced methanol. These opposing reactions may be present right from the beginning of the process and the desired CO_2 reduction reaction rate wins over the backward reactions for the first 150 minutes and afterwards gradually backed off. The concentration of methanol produced in the photochemical process for the samples collected every 30 minutes interval of irradiation time is shown in Figure 5.8, which was estimated from the calibration curve given in Figure 5.3. We can notice from the bar chart depicted in Figure 5.8 that for all the irradiation time the amount of methanol produced with In_2O_3M is consistently higher than that with In_2O_3T. The maximum concentration of methanol produced with the mesoporous In_2O_3-M catalyst was $\sim$ 481 μmol/100mL (at 150 min irradiation time) and the same with In_2O_3-T catalyst was $\sim$ 436 μmol/100mL (at 150 min irradiation time) under the same experimental conditions. The enhanced phtocatalytic activity of mesoporous In_2O_3-M nanocrystals in the CO_2 photoreduction can be mainly attributed to its larger specific surface area that brought about more active sites. According to a recent report [130] the yield of CO_2 conversion into methanol using Ag doped TiO_2 is 130 mol / gram of catalyst after one hour of irradiation, compared to 40 μmol/gram of pure TiO_2 as a catalyst. When we convert our 481 μmol yield using 400 mg of catalyst in 150 minutes to this standard, our yield using mesoporous In_2O_3-M is approximately 481 μmol/ gram of catalyst, which is 3.2 times higher than the highest achieved yield.

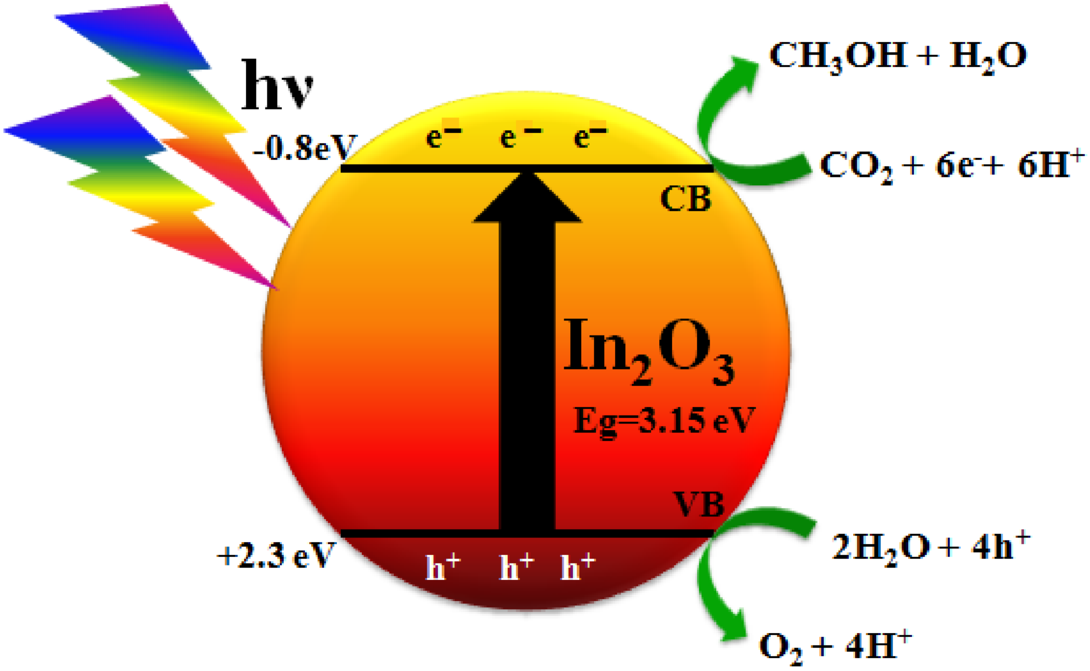

Figure 5.7: Schematic diagram for mechanism of enhanced photocatalytic activities for In_2O_3-T and In_2O_3-M samples

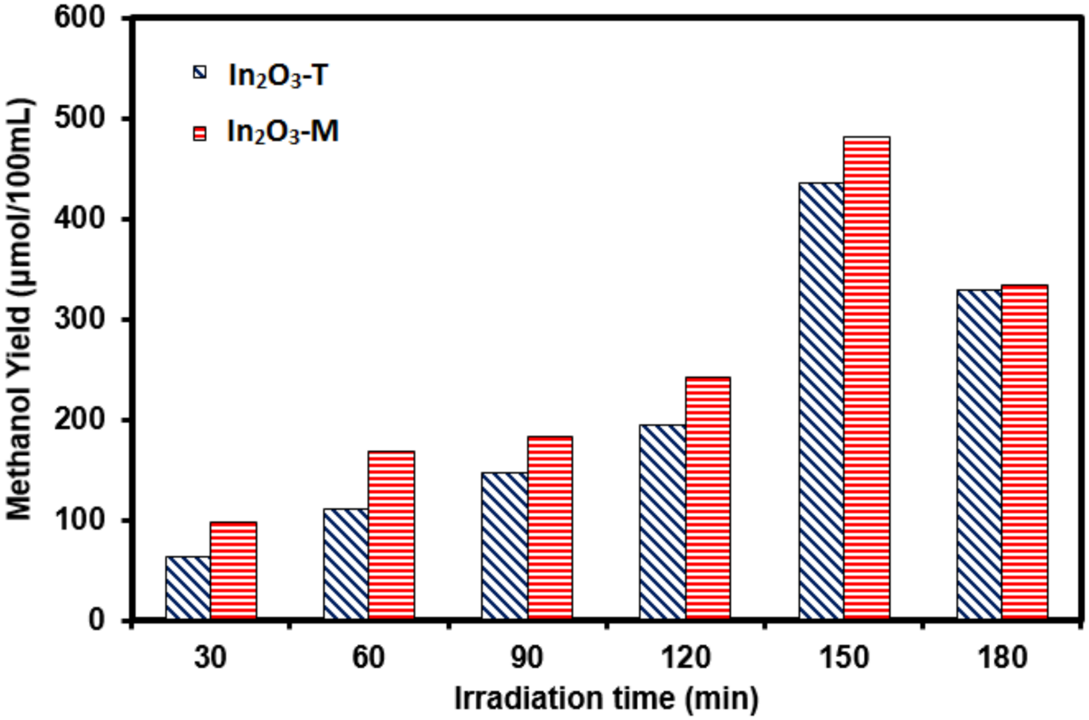

Figure 5.8: Chart showing concentration of methanol produced at different irradiation times with 355 nm laser

5.4 Quantum efficiency and CO_2 conversion efficiency

The quantum efficiency (QE) of the CO_2 was estimated by using Equations 5.3 and 5.4;

$$QE = \frac{Numnber\ of\ MeOH\ produced/time}{Number\ of\ photons\ of\ wavelength\ \lambda/time} \times 100 \tag{5.3}$$

$$Number\ of\ photons\ of\ wavelength\ \lambda = \frac{laser\ power \times\ time(s)}{h\nu} \tag{5.4}$$

Therefore, QE is the quotient of total number of target hydrocarbon molecules produced to total number of photons of the incident laser. Moreover, we applied Henrys law in calculating the amount of dissolved CO_2 in deionized water under our experimental conditions in order to estimate the CO_2 conversion efficiency of the process. Knowing the methanol concentration for a given irradiation time of the photocatalytic process, the CO_2 conversion efficiency $\{X(CO_2)\}$ is given by Equation 5.5;

$$X(CO_2) = \frac{[MeOH]}{[CO_2]} \tag{5.5}$$

where [MeOH] and $[CO_2]$ are methanol and CO_2 concentrations respectively. However, the estimated $X(CO_2)$ by this method may be slightly higher than the actual efficiency, this follows from Schlers experimental result that the solubility of CO_2 in a binary mixture of water and methanol increases with methanol content [129]. Figure 5.9 depicts the maximum QE and X(CO_2), obtained at 60 min irradiation time, which are 2.33 % and 11.8 % respectively with MIW-3 as the catalyst. The bar charts in Figure 5.10 compare the QE and X(CO_2) for each catalysts. Similarly, Figure 5.11 depicts the quantum efficiency of this photocatalytic process with In_2O_3-T and In_2O_3-M catalysts, where we can see that the quantum efficiency for mesoporous In_2O_3-M is consistently higher than that for the In_2O_3-T for all irradiation times considered in this work. The highest quantum efficiency for In_2O_3-M is 4.5 % as compared to 4.0 % for In_2O_3-T, which is approximately 12.5 % increase after 150 minutes of irradiation. Figure 5.12 shows the CO_2 conversion efficiency with irradiation time where we can see that the maximum CO_2 conversion efficiency achieved is 41.9 % for In_2O_3-T compared to 46.3 % in the case of In_2O_3-M, after 150 minutes of irradiation

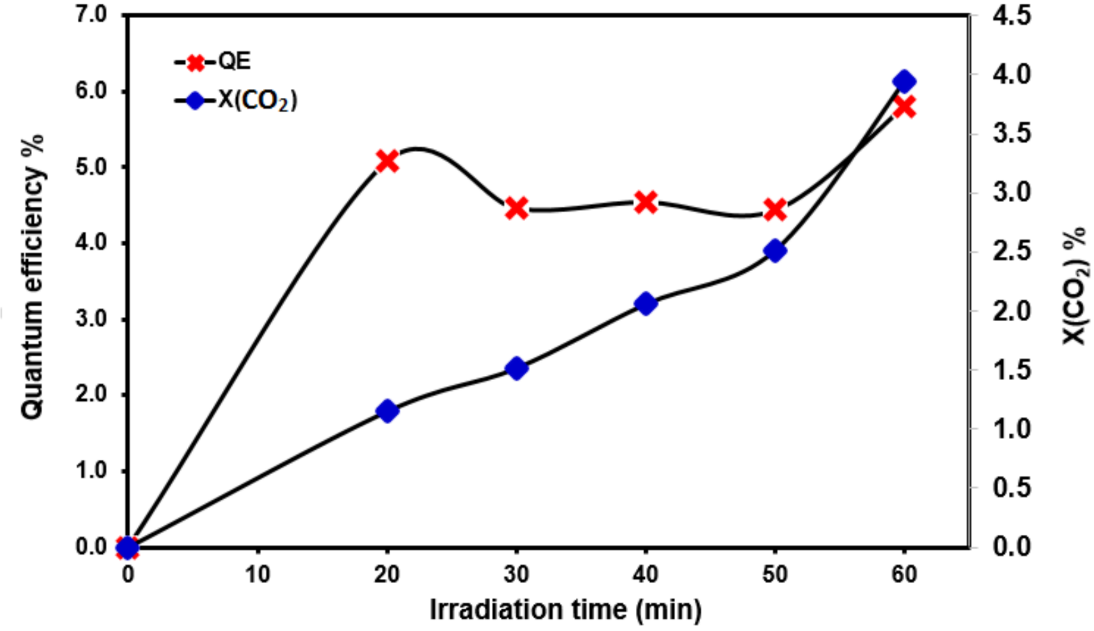

Figure 5.9: Quantum efficiency (QE) and CO_2 conversion efficiency ($X(CO_2)$) for MIW-3 at different irradiation time

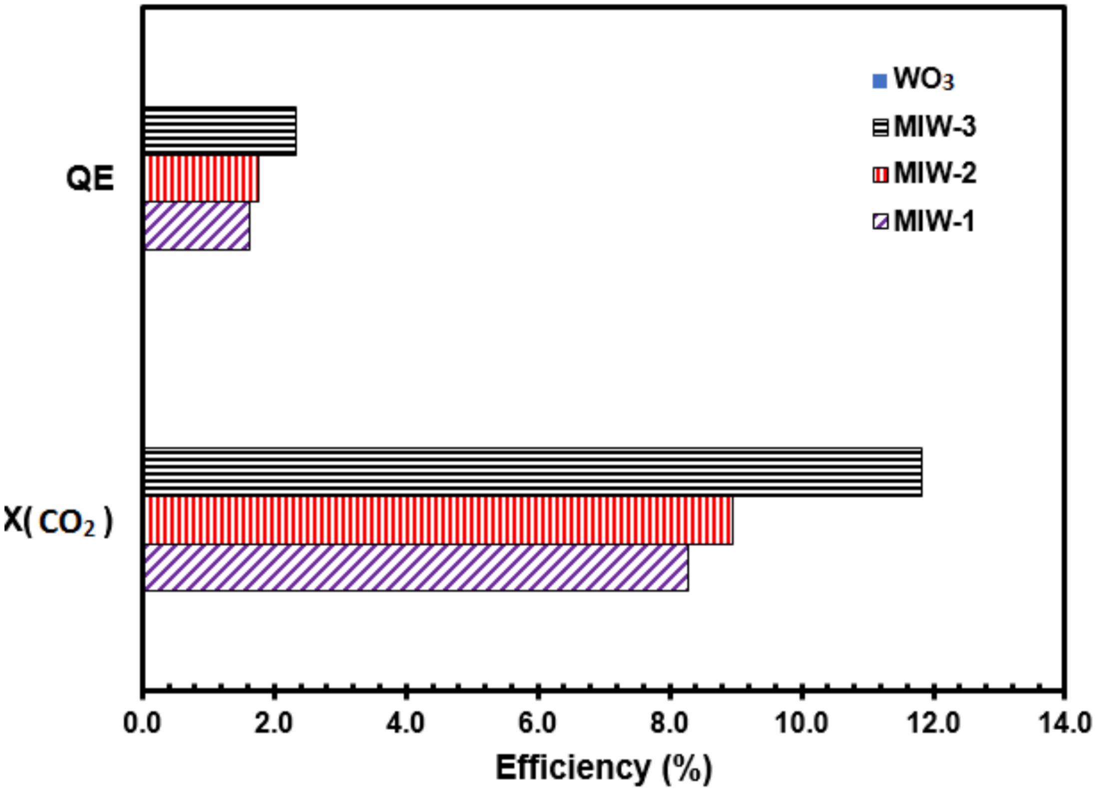

Figure 5.10: Comparison of the QE and $X(CO_2)$ for each catalyst

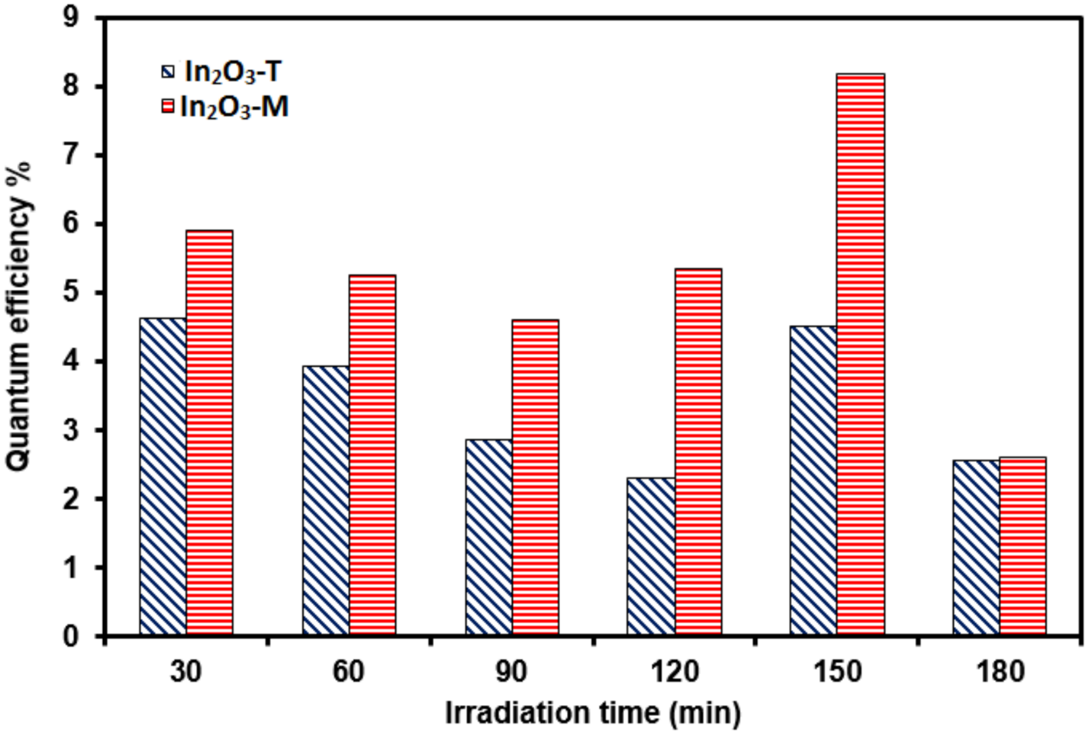

Figure 5.11: Quantum efficiencies of the process using In_2O_3-T and In_2O_3-M catalysts at different irradiation time

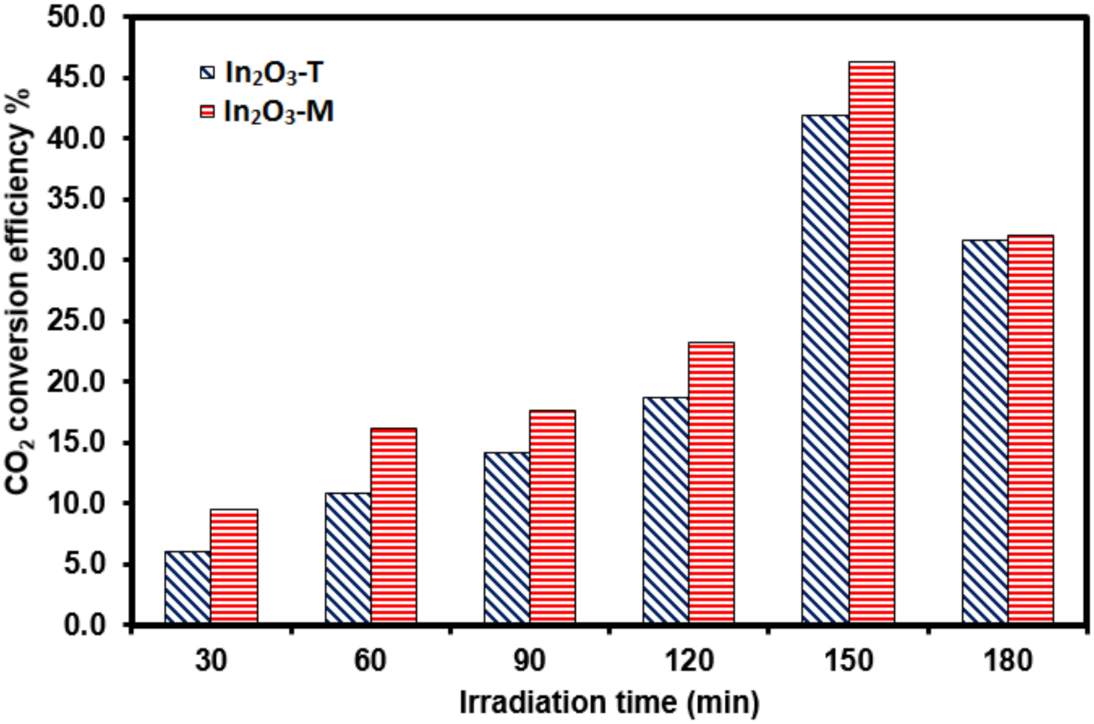

Figure 5.12: CO_2 conversion efficiencies of the process using In_2O_3-T and In_2O_3-M catalysts at different irradiation time

CONCLUSION AND OUTLOOK

In this work, we have successfully synthesized ordered mesoporous oxide semiconductor nanocatalaysts (WO_3, In_2O_3-T, In_2O_3-M, In_2O_3-WO_3, Ta/WO_3 and Nb/WO_3) with enhanced photocatalytic performance. This was confirmed by their application in photoassisted reduction of CO_2 to low carbon fuel (methanol). Nanocomposites of In_2O_3-WO_3 (named MIW-1, MIW-2 and MIW-3) were prepared in the ratio 1 : 3, 2 : 3 and 1 : 1 respectively. Similarly we introduced metal ions into lattice space of WO3 through doping. The dopants used were niobium (Nb) and tantalum (Ta) ions, which showed alteration in electro-physical, chemical as well as photoctalytic properties of WO_3.

Each of the doped WO_3 and the nanocomposite materials were characterized for various properties like optical properties, morphology, porosity and crystal structure, by UV-vis, FESEM, BET and XRD. Laser induced photocatalytic conversion of CO_2 to methanol over In_2O_3-WO_3 nanocomposites was performed and observed to have improved over pure WO_3 nanostructure. This application in laser induced photo-reduction of CO_2 shows that the material with highest In_2O_3 content has superior photocatalytic property over others since it gave the best methanol yield and efficiencies. Highest methanol yield, photonic efficiency for CO_2 photoreduction and CO_2 conversion efficiency, among the catalysts irradiated with 266 nm laser, were estimated to be about 149 μmol/100 mL of water, 2.33 % and 11.8 % respectively.

Also, we synthesized ordered mesoporous indium oxide (In_2O_3-M) with SBA-15 and the non-templated indium oxide (In_2O_3-T).This lead to variation in their optical, morphological and surface properties as well as catalytic activities. In_2O_3-T particles have quasi-cubic structures with high crystallinity and bigger pore sizes, while In_2O_3-M particles were characterized with smaller sizes, multiple PL emission, larger specific surface area and pore volume. These two materials were used as the photo-catalyst to convert CO_2 to methanol and the maximum methanol yield observed with In_2O_3-T andIn_2O_3-M are $\sim$ 436 μmol/100 mL and $\sim$ 481 μmol/100 mL respectively. The maximum quantum efficiency with In_2O_3-M (after 150 minutes of irradiation) is 4.5 % as compared to 4.0 % in the case of In_2O_3-T. The CO_2 conversion efficiency is 46.3 % for In_2O_3-M while it was about 41.9 % for In_2O_3-T and the results were discussed in light of morphological and optical characteristics of these materials.

Semiconductors studied in this work are oxides of indium (In) and tungsten (W). These materials have band gaps of $\sim$ 3.0 eV; which impedes the absorption of a large proportion of the available solar spectrum thereby diminishing the solar radiation efficiencies. Although efforts have already been made to find working combinations of semiconductor catalysts, much of the domain of pairs (even for the materials used in this work) is yet to be explored.

Some of the recently adopted innovations in photocatalysis, such as use of photosensitizer, were first applied in photovoltaics but could prove effective in photocatalysis. The use of organic semiconductors (OSCs), is another innovation which, to the best of our knowledge, has not yet been taken up in photocatalytic reduction of CO_2. Although organic photovoltaics are still less efficient than silicon [131], mutability of these semiconductors may make them interesting candidates for use in catalysis. The large scope of synthetic methods available permits tuning of the electronics [132]. Functional groups qualities could also be harnessed for effective CO_2 reduction.

REFERENCES

1. M. Huang, Y. Wu, and W. Hu, A facile synthesis of reduced graphene oxide-wrapped WO_3 nanowire composite and its enhanced electrochemical catalysis properties, *Ceram. Int.*, vol. 40, no. 5, pp. 7219-7225, 2014.

2. T. K. Ghorai, Synthesis of spherical mesoporous titania modified iron-niobate nanoclusters for photocatalytic reduction of 4-nitrophenol, *J. Mater. Res. Technol,* Vol. 4, no. 2, pp. 133-143, 2015.

3. Y. Hu, P. Wu, Y. Yin, H. Zhang, and C. Cai, Effects of structure, composition, and carbon support properties on the electrocatalytic activity of Pt-Ni-graphene nanocatalysts for the methanol oxidation, *Appl. Catal. B Environ.*, vol. 111-112, pp. 208217, 2012.

4. M. Khairy, S. a. El-Safty, M. Ismael, and H. Kawarada, Mesoporous NiO nanomagnets as catalysts and separators of chemical agents, *Appl. Catal. B Environ.*, vol. 127, pp. 1-10, 2012.

5. A. Macagnano, New Applications of Nanoheterogeneous Systems. Elsevier 2013.

6. A. Chapelle, F. Oudrhiri-Hassani, L. Presmanes, a. Barnab, and P. Tailhades, CO_2 sensing properties of semiconducting copper oxide and spinel ferrite nanocomposite thin film, *Appl. Surf. Sci.*, vol. 256, no. 14, pp. 4715-4719, 2010.

7. D. R. Miller, S. a Akbar, and P. a Morris, Nanoscale metal oxide-based heterojunctions for gas sensing: A review, *Sensors Actuators B*, vol. 204, pp. 250-272, 2014.

8. K. Wetchakun, T. Samerjai, N. Tamaekong, C. Liewhiran, C. Siriwong, V. Kruefu, A. Wisitsoraat, a. Tuantranont, and S. Phanichphant, Semiconducting metal oxides as sensors for environmentally hazardous gases, *Sensors Actuators, B*, vol. 160, no. 1, pp. 580-591, 2011.

9. N. Huesing, B. Launay, G. Kickelbick, S. Gross, L. Armelao, G. Bottaro, M. P. Feth, H. Bertagnolli, and G. Kothleitner, Transition metal oxide-doped mesostructured silica films, *Appl. Catal. A Gen.*, vol. 254, no. 2, pp. 297-310, 2003.

10. Q. Ye, J. Zhao, F. Huo, D. Wang, S. Cheng, T. Kang, and H. Dai, Nanosized Au supported on three-dimensionally ordered mesoporous β-MnO$_3$: Highly active catalysts for the low-temperature oxidation of carbon monoxide, benzene, and toluene, *Microporous Mesoporous Mater.*, vol. 172, pp. 20-29, 2013.

11. S. Phanichphant, Semiconductor metal oxides as hydrogen gas sensors, *Procedia Eng.*, vol. 87, pp. 795-802, 2014.

12. A. Chapelle, M. H. Yaacob, I. Pasquet, L. Presmanes, A. Barnab, P. Tailhades, J. Du Plessis, and K. Kalantar-zadeh, Structural and gas-sensing properties of CuOCu$_x$Fe$_3 - x$O$_4$ nanostructured thin films, *Sensors Actua-*

tors B, vol. 153, no. 1, pp. 117-124, 2011.

13. M. R. Bayati, H. Zargar, R. Molaci, F. Golcstani-Fard, E. Kajbafvala, and S. Zanganeh, One step growth of WO_3-loaded Al_2O_3 micro/nano-porous films by micro arc oxidation, Colloids Surfaces A Physicochem. *Eng. Asp.*, vol. 355, no. 1-3, pp. 187-192, 2010.

14. J. Xic, Z. Zhou, Y. Lian, Y. Hao, X. Liu, M. Li, and Y. Wci, Simple preparation of WO_3-ZnO composites with UVVis photocatalytic activity and energy storage ability, *Ceram. Int.*, vol. 40, no. 8, pp. 12519-12524, 2014.

15. S. M. Zanetti, K. O. Rocha, J. a J. Rodrigues, and E. Longo, Soft-chemical synthesis, characterization and humidity sensing behavior of WO_3/TiO_2 nanopowders, *Sensors Actuators, B*, vol. 190, pp. 40-47, 2014.

16. Y. X. Gan, Structural assessment of nanocomposites, *Micron*, vol. 43, no. 7, pp. 782-817, 2012.

17. A. T. Mane, S. T. Navale, and V. B. Patil, Room temperature NO_2 gas sensing properties of DBSA doped PPy-WO_3 hybrid nanocomposite sensor, *Org. Electron.*, vol. 19, no. 2, pp. 15-25, 2015.

18. R. J. Wu, W. C. Chang, K. M. Tsai, and J. G. Wu, The Novel CO sensing material CoOOH-WO_3 with Au and SWCNT performance enhancement, *Sensors Actuators, B*, vol. 138, no. 1, pp. 35-41, 2009.

19. H. Zhang, Z. Liu, J. Yang, W. Guo, L. Zhu, and W. Zheng, Temperature

and acidity effects on WO_3 nanostructures and gas- sensing properties of WO_3 nanoplates, *Mater. Res. Bull.*, vol. 57, pp. 260-267, 2014.

20. G. Mahmodi, S. Sharifnia, F. Rahimpour, and S. N. Hosseini, Photocatalytic conversion of CO_2 and CH_4 using ZnO coated mesh: Effect of operational parameters and optimization, *Sol. Energy Mater. Sol. Cells*, vol. 111, pp. 31-40, 2013.

21. A. Nishimura, G. Mitsui, M. Hirota, and E. Hu, “CO_2 reforming performance and visible light responsibility of Cr-doped TiO_2 prepared by sol-gel and dip-coating method, *Int. J. Chem. Eng.*, vol 222, pp. 234-247, 2010.

22. A. B. A. A. Nassr, A. Quetschke, E. Koslowski, and M. Bron, Electrocatalytic oxidation of formic acid on Pd/MWCNTs nanocatalysts prepared by the polyol method, *Electrochim. Acta*, vol. 102, pp. 202-211, 2013.

23. Y. Li, W.-N. Wang, Z. Zhan, M.-H. Woo, C.-Y. Wu, and P. Biswas, Photocatalytic reduction of CO_2 with H2O on mesoporous silica supported Cu/TiO_2 catalysts, *Appl. Catal. B Environ.*, vol. 100, no. 1-2, pp. 386392, 2010.

24. Q. Li, L. Zong, C. Li, and J. Yang, Photocatalytic reduction of CO_2 on MgO/TiO_2 nanotube films, *Appl. Surf. Sci.*, vol. 314, pp. 458-463, 2014.

25. Y. Izumi, Recent advances in the photocatalytic conversion of carbon dioxide to fuels with water and/or hydrogen using solar energy and beyond, *Coord. Chem. Rev.*, vol. 257, no. 1, pp. 171-186, 2013.

26. Y. Li, Y. Guo, S. Li, Y. Li, and J. Wang, Efficient visible-light photocatalytic hydrogen evolution over platinum supported titanium dioxide nanocomposites coating up-conversion luminescence agent (Er^{3+}:$Y_3Al_5O_{12}$/$PtTiO_2$), *Int. J. Hydrogen Energy*, vol. 40, no. 5, pp. 2132-2140, 2015.

27. W.-N. Wang, Comparison of CO2 Photoreduction Systems: A Review, *Aerosol Air Qual. Res.*, pp. 533-549, 2014.

28. A. FUJISHIMA, X. ZHANG, and D. TRYK, TiO_2 photocatalysis and related surface phenomena, *Surf. Sci. Rep.*, vol. 63, no. 12, pp. 515-582, 2008.

29. J. L. White, M. F. Baruch, J. E. Pander, Y. Hu, I. C. Fortmeyer, J. E. Park, T. Zhang, K. Liao, J. Gu, Y. Yan, T. W. Shaw, E. Abelev, and A. B. Bocarsly, Light-Driven Heterogeneous Reduction of Carbon Dioxide: Photocatalysts and Photoelectrodes, *Chem. Rev.*, vol. 115, no. 23, pp. 12888-12935, 2015.

30. Wiley: Electrochemical Methods: Fundamentals and Applications, 2nd Edition. [Online]. Available: http://eu.wiley.com/WileyCDA/WileyTitle/productCd-0471043729.html. [Accessed: 15-Feb-2016].

31. R. J. Forster , P. Bertoncello,T. E. Keyes, "Electrogenerated Chemiluminescence,". *Annu Rev Anal Chem*, vol, 2, pp 359-385, 2009

32. R. V. De Krol, M. Grtzel, "*Photoelectro - chemical Hydrogen Production*," Springer 2012.

33. W. Wang and P. Biswas, Aerosol Processing of Advanced Functional Materials for Energy and Environmental Applications, *Earozoru Kenkyu*, vol. 29, no. 2, pp. 77-87, 2014.

34. C. A. Martnez-huitle and L. S. Andrade, *Reviso*, vol. 34, no. 5, pp. 850-858, 2011.

35. Z. Chen, H. N. Dinh, and E. Miller, *Photoelectrochemical water splitting: standards, experimental methods, and protocols*'. Springer 2013.

36. T. W. Hamann and N. S. Lewis, Control of the stability, electron-transfer kinetics, and pH-dependent energetics of Si/H_2O interfaces through methyl termination of Si(111) surfaces, *J. Phys. Chem. B*, vol. 110, no. 45, pp. 22291-22294, 2006.

37. A. FUJISHIMA and K. HONDA, Electrochemical Photolysis of Water at a Semiconductor Electrode, *Nature*, vol. 238, no. 5358, pp. 37-38, Jul. 1972.

38. J. J. Kelly and R. Memming, The Influence of Surface Recombination and Trapping on the Cathodic Photocurrent at p-Type III-V Electrodes, *J. Electrochem. Soc.*, vol. 129, no. 4, pp. 730-738, 1982.

39. L. Peter, L. Peter, J. Li, J. Li, R. Peat, and R. Peat, Surface recombination at semiconductor electrodes. Part I Transient and steady-state photocurrents, *J. Electroanal. Chem.*, vol. 165, pp. 29-40, 1984.

40. M. Nishida, A theoretical treatment of charge transfer via surface states at a semiconductor-electrolyte interface: Analysis of the water photoelectrolysis process, *J. Appl. Phys.*, vol. 51, no. 3, p. 1669, 1980.

41. V. P. Indrakanti, H. H. Schobert, and J. D. Kubicki, Quantum mechanical modeling of CO_2 interactions with irradiated stoichiometric and oxygen-deficient anatase TiO_2 surfaces: Implications for the photocatalytic reduction of CO_2, *Energy and Fuels*, vol. 23, no. 10, pp. 5247-5256, 2009.

42. W. Tu, Y. Zhou, and Z. Zou, Photocatalytic conversion of CO_2 into renewable hydrocarbon fuels: State-of-the-art accomplishment, challenges, and prospects, *Adv. Mater.*, vol. 26, no. 27, pp. 4607-4626, 2014.

43. K. I. Yamanaka, S. Sato, M. Iwaki, T. Kajino, and T. Morikawa, Photoinduced electron transfer from nitrogen-doped tantalum oxide to adsorbed ruthenium complex, *J. Phys. Chem. C*, vol. 115, no. 37, pp. 18348-18353, 2011.

44. M. Yu, Y.-Z. Long, B. Sun, and Z. Fan, Recent advances in solar cells based on one-dimensional nanostructure arrays, *Nanoscale*, vol. 4, no. 9, p. 2783, 2012.

45. J. Han, Y. Hayashi, A system dynamics model of CO2 mitigation in Chinas inter-city passenger transport*Transportation Research Part D*, vol. 13, no. 5, pp. 298-305 2008.

46. A. D. Yoffe, Semiconductor quantum dots and related systems: Electronic,

optical, luminescence and related properties of low dimensional systems, *Adv. Phys.*, vol. 8732, no. February, pp. 1-208, 2010.

47. C. Wang, R. L. Thompson, J. Baltrus, and C. Matranga, Visible light photoreduction of CO_2 using CdSe/Pt/TiO_2 heterostructured catalysts, *J. Phys. Chem. Lett.*, vol. 1, no. 1, pp. 48-53, 2010.
48. J. Yu, J. Low, W. Xiao, P. Zhou, and M. Jaronicc, Enhanced photocatalytic CO_2-reduction activity of anatase TiO_2 by coexposed {001} and {101} facets., *J. Am. Chem. Soc., vo*l. 136, no. 25, pp. 8839-42, 2014.
49. J. Li and N. Wu, Semiconductor-based photocatalysts and photoelectrochemical cells for solar fuel generation: a review, *Catal. Sci. Technol.*, vol. 5, no. 3, pp. 1360-1384, 2015.
50. F. E. Osterloh, Inorganic nanostructures for photoelectrochemical and photocatalytic water splitting., *Chem. Soc. Rev.*, vol. 42, no. 6, pp. 2294-320, 2013.
51. O. L. Muskens, J. G. Rivas, R. E. Algra, E. P. A. M. Bakkers, and A. Lagendijk, Design of light scattering in nanowire materials for photovoltaic applications, *Nano Lett.*, vol. 8, no. 9, pp. 2638-2642, 2008.
52. T. Baba, Slow light in photonic crystals, *Nat. Photonics*, vol. 2, no. 8, pp. 465-473, Aug. 2008.
53. N. Ahmed, M. Morikawa, and Y. Izumi, Photocatalytic conversion of carbon

dioxide into methanol using optimized layered double hydroxide catalysts, *Catal. Today*, vol. 185, no. 1, pp. 263-269, 2012.

54. S. Das and W. M. a Wan Daud, Photocatalytic CO_2 transformation into fuel: A review on advances in photocatalyst and photoreactor, *Renew. Sustain. Energy Rev.*, vol. 39, pp. 765-805, 2014.

55. I. Ganesh, Conversion of carbon dioxide into methanol - A potential liquid fuel: Fundamental challenges and opportunities (a review), *Renew. Sustain. Energy Rev.*, vol. 31, pp. 221-257, 2014.

56. X. Sun, Y. Shi, H. Ji, X. Li, S. Cai, and C. Zheng, Nanocasting synthesis of ordered mesoporous indium tin oxide (ITO) materials with controllable particle size and high thermal stability, *J. Alloys Compd.*, vol. 545, pp. 5-11, 2012.

57. B. Tahir, M. Tahir, and N. S. Amin, Goldindium modified TiO_2 nanocatalysts for photocatalytic CO_2 reduction with H2 as reductant in a monolith photoreactor, *Appl. Surf. Sci.*, vol. 338, pp. 1-14, 2015.

58. Efficient catalytic system for the photocatalytic reduction of carbon dioxide to hydrocarbons, *Focus Catal.*, vol. 2015, no. 2, pp. 6, 2015.

59. F. Yaripour, Z. Shariatinia, S. Sahebdelfar, and A. Irandoukht, The effects of synthesis operation conditions on the properties of modified -alumina nanocatalysts in methanol dehydration to dimethyl ether using factorial experimental design, *Fuel*, vol. 139, pp. 40-50, 2015.

60. W. C. Chueh and S. M. Haile, Ceria as a Thermochemical Reaction Medium for Selectively Generating Syngas or Methane from H_2O and CO_2, *ChemSusChem*, vol. 2, no. 8, pp. 735-739, 2009.

61. T. Abe, T. Yoshida, S. Tokita, F. Taguchi, H. Imaya, and M. Kaneko, Factors affecting selective electrocatalytic CO_2 reduction with cobalt phthalocyanine incorporated in a polyvinylpyridine membrane coated on a graphite electrode, *J. Electroanal. Chem.*, vol. 412, no. 1-2, pp. 125-132, 1996.

62. M. Jitaru, D. a. Lowy, M. Toma, B. C. Toma, and L. Oniciu, Electrochemical reduction of carbon dioxide on flat metallic cathodes, *J. Appl. Electrochem.*, vol. 27, no. 8, pp. 875-889, 1997.

63. T. INOUE, A. FUJISHIMA, S. KONISHI, and K. HONDA, Photoelectrocatalytic reduction of carbon dioxide in aqueous suspensions of semiconductor powders, *Nature*, vol. 277, no. 5698, pp. 637-638, Feb. 1979.

64. R. E. Blankenship, D. M. Tiede, J. Barber, G. W. Brudvig, G. Fleming, M. Ghirardi, M. R. Gunner, W. Junge, D. M. Kramer, A. Melis, T. A. Moore, C. C. Moser, D. G. Nocera, A. J. Nozik, D. R. Ort, W. W. Parson, R. C. Prince, and R. T. Sayre, Comparing photosynthetic and photovoltaic efficiencies and recognizing the potential for improvement., *Science*, vol. 332, no. 6031, pp. 805-9, May 2011.

65. T. Athar, Metal Oxide Nanopowder, First Edit. Elsevier 2010.

66. S. Supothina, Effect of SiO_2 Doping on Growth Retardation of WO_3 Nanoplate, *J. Solid Mech. Mater. Eng.*, vol. 1, no. 4, pp. 431-438, 2007.

67. S. Supothina, P. Seeharaj, S. Yoriya, and M. Sriyudthsak, Synthesis of tungsten oxide nanoparticles by acid precipitation method, Ceram. Int., vol. 33, no. 6, pp. 931936, 2007.

68. L. Zhang, N. Li, H. Jiu, G. Qi, and Y. Huang, ZnO-reduced graphene oxide nanocomposites as efficient photocatalysts for photocatalytic reduction of CO_2, *Ceram. Int.*, vol. 41, pp. 6256-6262, 2015.

69. S. Anandan and J. J. Wu, Ultrasound assisted synthesis of TiO_2-WO_3 heterostructures for the catalytic degradation of Tergitol (NP-9) in water, *Ultrason. Sonochem.*, vol. 21, no. 4, pp. 1284-1288, 2014.

70. H. Widiyandari, A. Purwanto, R. Balgis, T. Ogi, and K. Okuyama, CuO/WO_3 and Pt/WO_3 nanocatalysts for efficient pollutant degradation using visible light irradiation, *Chem. Eng. J.*, vol. 180, pp. 323-329, 2012.

71. R. Vadakkekara, M. Chakraborty, and P. a. Parikh, Hollow mesoporous silica spheres supported Ag and Ag-Au catalyzed reduction of 4-nitrobenzo-15-crown, *J. Ind. Eng. Chem.*, vol. 20, no. 3, pp. 767-774, 2014.

72. P. Akhter, M. Hussain, G. Saracco, and N. Russo, Novel nanostructured-TiO_2 materials for the photocatalytic reduction of CO_2 greenhouse gas to hydrocarbons and syngas, *Fuel*, vol. 149, pp. 55-65, 2015.

73. K. Hayat, M. a. Gondal, M. M. Khaled, Z. H. Yamani, and S. Ahmed, Laser induced photocatalytic degradation of hazardous dye (Safranin-O) using self synthesized nanocrystalline WO_3, *J. Hazard. Mater.*, vol. 186, no. 2-3, pp. 1226-1233, 2011.

74. G. Korotcenkov, Metal oxides for solid-state gas sensors: What determines our choice?, *Mater. Sci. Eng. B Solid-State Mater. Adv. Technol.*, vol. 139, no. 1, pp. 1-23, 2007.

75. P. Xia, S. Zuo, F. Liu, and C. Qi, Ceria modified crystalline mesoporous Cr_2O_3 based nanocomposites supported metal oxide for benzene complete oxidation, *Catal. Commun.*, vol. 41, pp. 91-95, 2013.

76. Z. G. Zhao and M. Miyauchi, Nanoporous-walled tungsten oxide nanotubes as highly active visible-light-driven photocatalysts, *Angew. Chemie - Int. Ed.*, vol. 47, no. 37, pp. 7051-7055, 2008.

77. W. Mu, X. Xie, X. Li, R. Zhang, Q. Yu, K. Lv, H. Wei, and Y. Jian, Characterizations of Nb-doped WO_3 nanomaterials and their enhanced photocatalytic performance, *RSC Adv.*, vol. 4, no. 68, p. 36064, 2014.

78. S. L. Liew, Z. Zhang, T. W. G. Goh, G. S. Subramanian, H. L. D. Seng, T. S. A. Hor, H. K. Luo, and D. Z. Chi, Yb-doped WO_3 photocatalysts for water oxidation with visible light, *Int. J. Hydrogen Energy*, vol. 39, no. 9, pp. 4291-4298, 2014.

79. F. Fang, J. Kennedy, J. Futter, T. Hopf, a Markwitz, E. Manikandan, and G.

Henshaw, Size-controlled synthesis and gas sensing application of tungsten oxide nanostructures produced by arc discharge., *Nanotechnology*, vol. 22, no. 33, p. 335702, 2011.

80. L. Zhou, L. Yang, P. Yuan, J. Zou, Y. Wu, and C. Yu, "α-MoO_3 Nanobelts: A High Performance Cathode Material for Lithium Ion Batteries, *J. Phys. Chem. C*, vol. 114, no. 49, pp. 21868-21872, 2010.

81. C. Feng, S. Wang, and B. Geng, Ti(IV) doped WO_3nanocuboids: fabrication and enhanced visible-light-driven photocatalytic performance., *Nanoscale*, vol. 3, no. 9, pp. 3695-9, 2011.

82. J. Palau, a. a. Assadi, J. M. Penya-roja, a. Bouzaza, D. Wolbert, and V. Martnez-Soria, Isovaleraldehyde degradation using UV photocatalytic and dielectric barrier discharge reactors, and their combinations, *J. Photochem. Photobiol. A Chem.*, vol. 299, pp. 110-117, 2015.

83. X. Liu, R. Wang, T. Zhang, Y. He, J. Tu, and X. Li, Synthesis and characterization of mesoporous indium oxide for humidity-sensing applications, *Sensors Actuators, B Chem.*, vol. 150, no. 1, pp. 442-448, 2010.

84. L. Zheng, C. Chen, Y. Zheng, Y. Zhan, Y. Cao, X. Lin, Q. Zheng, K. Wei, and J. Zhu, Photocatalytic activity of $ZnO/Sn_{1-x}Zn_xO_{2-x}$ nanocatalysts: A synergistic effect of doping and heterojunction, *Appl. Catal. B Environ.*, vol. 148-149, pp. 44-50, 2014.

85. Slamet, H. W. Nasution, E. Purnama, S. Kosela, and J. Gunlazuardi, Pho-

tocatalytic reduction of CO_2 on copper-doped Titania catalysts prepared by improved-impregnation method, *Catal. Commun.*, vol. 6, no. 5, pp. 313-319, 2005.

86. S. C. Chang and M. H. Huang, Formation of short In_2O_3 nanorod arrays within mesoporous silica, *J. Phys. Chem. C*, vol. 112, no. 7, pp. 2304-2307, 2008.

87. J.-L. Cao, G.-J. Li, Y. Wang, G. Sun, X.-D. Wang, B. Hari, and Z.-Y. Zhang, Mesoporous CoFeO nanocatalysts: Preparation, characterization and catalytic carbon monoxide oxidation, *J. Environ. Chem. Eng.*, vol. 2, no. 1, pp. 477-483, 2014.

88. Y. Liu, H. Dai, J. Deng, S. Xie, H. Yang, W. Tan, W. Han, Y. Jiang, and G. Guo, Mesoporous Co_3O_4-supported gold nanocatalysts: Highly active for the oxidation of carbon monoxide, benzene, toluene, and o-xylene, *J. Catal.*, vol. 309, pp. 408-418, 2014.

89. C. Carlesi, D. Carvajal, D. Vasquez, and R. Schrebler Arratia, Analysis of carbon dioxide-to-methanol direct electrochemical conversion mediated by an ionic liquid, *Chem. Eng. Process. Process Intensif.*, vol. 85, pp. 48-56, 2014.

90. M. Tahir and N. S. Amin, Recycling of carbon dioxide to renewable fuels by photocatalysis: Prospects and challenges, *Renew. Sustain. Energy Rev.*, vol. 25, pp. 560-579, 2013.

91. W. G. Menezes, P. H. C. Camargo, M. M. Oliveira, D. J. Evans, J. F. Soares, and a. J. G. Zarbin, Sol-gel processing of a bimetallic alkoxide precursor confined in a porous glass matrix: A route to novel glass/metal oxide nanocomposites, *J. Colloid Interface Sci.*, vol. 299, no. 1, pp. 291-296, 2006.

92. C. H. Liu, N. C. Lai, S. C. Liou, M. W. Chu, C. H. Chen, and C. M. Yang, Deposition and thermal transformation of metal oxides in mesoporous SBA-15 silica with hydrophobic mesopores, *Microporous Mesoporous Mater.*, vol. 179, pp. 40-47, 2013.

93. X. Li, H. Liu, D. Luo, J. Li, Y. Huang, H. Li, Y. Fang, Y. Xu, and L. Zhu, Adsorption of CO_2 on heterostructure $CdS(Bi_2S_3/TiO_2$ nanotube photocatalysts and their photocatalytic activities in the reduction of CO_2 to methanol under visible light irradiation, *Chem. Eng. J.*, vol. 180, pp. 151-158, 2012.

94. M. U. Anu Prathap and R. Srivastava, Synthesis of nanoporous metal oxides through the self-assembly of phloroglucinol-formaldehyde resol and tri-block copolymer, *J. Colloid Interface Sci.*, vol. 358, no. 2, pp. 399-408, 2011.

95. B. J. Clapsaddle, D. W. Sprehn, A. E. Gash, J. H. Satcher, and R. L. Simpson, A versatile sol-gel synthesis route to metal-silicon mixed oxide nanocomposites that contain metal oxides as the major phase, *J. Non. Cryst. Solids*, vol. 350, pp. 173-181, 2004.

96. C. Daz, M. L. Valenzuela, D. Bravo, C. Dickinson, and C. ODwyer,

Solid-state synthesis of embedded single-crystal metal oxide and phosphate nanoparticles and in situ crystallization, *J. Colloid Interface Sci.*, vol. 362, no. 1, pp. 21-32, 2011.

97. Y. Hu, Q. Shao, P. Wu, H. Zhang, and C. Cai, Synthesis of hollow mesoporous Pt-Ni nanosphere for highly active electrocatalysis toward the methanol oxidation reaction, *Electrochem. commun.*, vol. 18, no. 1, pp. 96-99, 2012.
98. P. K. Rastogi, V. Ganesan, and S. Krishnamoorthi, Palladium nanoparticles incorporated polymer-silica nanocomposite based electrochemical sensing platform for nitrobenzene detection, *Electrochim. Acta*, vol. 147, pp. 442-450, 2014.
99. T. N. Templates and A. P. Templates, *Nanostructures of Metal Oxides,* 2011.
100. L. Li, C. Tian, S. H. Chai, A. Binder, S. Brown, G. M. Veith, and S. Dai, Gold nanocatalysts supported on heterostructured PbSO$_2$-MCF mesoporous materials for CO oxidation, *Catal. Commun.*, vol. 46, pp. 234-237, 2014.
101. A. Biabani-Ravandi and M. Rezaei, Low temperature CO oxidation over Fe-Co mixed oxide nanocatalysts, *Chem. Eng. J.*, vol. 184, no. 3, pp. 141-146, 2012.
102. MIT CMSE X-ray Diffraction Facility. [Online]. Available: *http://prism.mit.edu/xray/.* [Accessed: 17-Nov-2015].

103. I. Vamvasakis, I. Georgaki, D. Vernardou, G. Kenanakis, and N. Katsarakis, Synthesis of WO_3 catalytic powders: evaluation of photocatalytic activity under NUV/visible light irradiation and alkaline reaction pH, *J. Sol-Gel Sci. Technol.*, vol. 76, no. 1, pp. 120-128, 2015.

104. H. Kim, H. Na, and J. Yang, Synthesis, structure, photoluminescence, and raman spectrum of indium oxide nanowires, *Acta Phys. Pol. A*, vol. 119, no. 2, pp. 143-145, 2011.

105. J. Yu, L. Yuan, H. Wen, M. Shafiei, M. R. Field, J. Liang, J. Yang, Z. F. Liu, W. Wlodarski, N. Motta, Y. X. Li, G. Zhang, K. Kalantar-Zadeh, and P. T. Lai, Hydrothermally formed functional niobium oxide doped tungsten nanorods., *Nanotechnology*, vol. 24, no. 49, p. 495501, Dec. 2013.

106. W. Chun, A. Ishikawa, H. Fujisawa, T. Takata, J. N. Kondo, M. Hara, M. Kawai, Y. Matsumoto, and K. Domen, Conduction and Valence Band Positions of Ta_2O_5 , TaON, and $Ta_3N_5$by UPS and Electrochemical Methods, *J. Phys. Chem. B*, vol. 107, no. 8, pp. 1798-1803, 2003.

107. W. Hu, Y. Zhao, Z. Liu, C. W. Dunnill, D. H. Gregory, and Y. Zhu, Nanostructural evolution: From one-dimensional tungsten oxide nanowires to three-dimensional ferberite flowers, *Chem. Mater.*, vol. 20, no. 17, pp. 5657-5665, 2008.

108. J. Theerthagiri, R. A. Senthil, A. Malathi, A. Selvi, J. Madhavan, and M. Ashokkumar, Synthesis and characterization of a $CuSWO_3$ composite

photocatalyst for enhanced visible light photocatalytic activity, *RSC Adv.*, vol. 5, no. 65, pp. 52718-52725, 2015.

109. J. Tang, Z. Zou, and J. Ye, Photophysical and photocatalytic properties of $AgInW_2O_8$, *J.Phys. Chem B*, vol 107 pp. 14265-14269, 2003.

110. M. A. Gondal, M. A. Ali, X. F. Chang, K. Shen, Q. Y. Xu, and Z. H. Yamani, Pulsed laser-induced photocatalytic reduction of greenhouse gas CO_2 into methanol: A value-added hydrocarbon product over SiC., *J. Environ. Sci. Health. A. Tox. Hazard. Subst. Environ. Eng.*, vol. 47, no. 11, pp. 1571-6, Jan. 2012.

111. V. Dimbeg-mali, . Barbari-mikoevi, and K. Itri, Kubelka-Munk Theory in Describing Optical Properties of Paper (1), *Tech. Gaz.*, vol. 18, no. 1, pp. 117-124, 2011.

112. P. KUBELKA, New contributions to the optics of intensely light-scattering materials., *J. Opt. Soc. Am.*, vol. 38, no. 5, pp. 448-57, May 1948.

113. L. Yin, D. Chen, M. Hu, H. Shi, D. Yang, B. Fan, G. Shao, R. Zhang, and G. Shao, Microwave-assisted growth of In_2O_3 nanoparticles on WO_3 nanoplates to improve H_2S-sensing performance, *J. Mater. Chem. A*, vol. 2, no. 44, pp. 18867-18874, 2014.

114. H. Yang, L. Liu, H. Liang, J. Wei, and Y. Yang, Phase-controlled synthesis of monodispersed porous In_2O_3 nanospheres via an organic acid-assisted hydrothermal process, *CrystEngComm,* vol. 13, no. 15, p. 5011, 2011.

115. X. Lu and L. Yin, Porous Indium Oxide Nanorods: Synthesis, Characterization and Gas Sensing Properties, *J. Mater. Sci. Technol.*, vol. 27, no. 8, pp. 680-684, 2011.

116. E. Washizu, A. Yamamoto, Y. Abe, M. Kawamura, and K. Sasaki, Optical and electrochromic properties of RF reactively sputtered WO_3 films, *Solid State Ionics*, vol. 165, no. 1-4, pp. 175-180, 2003.

117. A. Rougier, F. Portemer, A. Quede, and M. El Marssi, Characterization of pulsed laser deposited WO_3 thin films for electrochromic devices, *Appl. Surf. Sci.*, vol. 153, pp. 1-9, 1999.

118. X. Wang, X. Tian, F. Li, J. Zhao, Y. Li, R. Liu, and Y. Hao, The synergy between Ti species and g-$C_3N_4$by doping and hybridization for the enhancement of photocatalytic H_2 evolution, *Dalt. Trans.*, vol. 44, no. 40, pp. 17859-17866, 2015.

119. C. Y. Su and H. C. Lin, Direct route to tungsten oxide nanorod bundles: Microstructures and electro-optical properties, *J. Phys. Chem. C*, vol. 113, no. 10, pp. 4042-4046, 2009.

120. NIST XPS Database Detail Page. [Online]. Available: *http://srdata.nist.gov/xps/XPSDetailPage.aspx?AllDataNo=22318#Citation.htm.* [Accessed: 20-Nov-2015].

121. NIST XPS Database Detail Page. [Online]. Available:

http://srdata.nist.gov/xps/XPSDetailPage.aspx?AllDataNo=2335. [Accessed: 18-Feb-2016].

122. NIST XPS Database Detail Page. [Online]. Available: *http://srdata.nist.gov/xps/XPSDetailPage.aspx?AllDataNo=30918.* [Accessed: 18-Feb-2016].

123. NIST XPS Database, Selected Element Search Result. [Online]. Available: $http : //srdata.nist.gov/xps/EngElmSrchQuery.aspx?EType = PE\&CSOpt = Retri_ex_dat\&Elm = Nb.$ [Accessed: 18-Feb-2016].

124. NIST XPS Database, Selected Element Search Result. [Online]. Available: $http : //srdata.nist.gov/xps/EngElmSrchQuery.aspx?EType = PE\&CSOpt = Retri_ex_dat\&Elm = Ta.$ [Accessed: 18-Feb-2016].

125. J. Wang, G. Ji, Y. Liu, M. a. Gondal, and X. Chang, Cu=O/TiO= heterostructure nanotube arrays prepared by an electrodeposition method exhibiting enhanced photocatalytic activity for CO= reduction to methanol, *Catal. Commun.*, vol. 46, pp. 17-21, 2014.

126. Y. Bai, P.-Q. Wang, J.-Y. Liu, and X.-J. Liu, Enhanced photocatalytic performance of direct Z-scheme BiOClg-C_3N_4 photocatalysts, *RSC Adv.*, vol. 4, no. 37, p. 19456, 2014.

127. A. a. Ismail and D. W. Bahnemann, One-step synthesis of mesoporous platinum/titania nanocomposites as photocatalyst with enhanced photocatalytic activity for methanol oxidation, *Green Chem.*, vol. 13, no. 2, p. 428,

2011.

128. S. Suzuki, T. Tsuneda, and K. Hirao, A theoretical investigation on photocatalytic oxidation on the TiO_2 surface., J. Chem. Phys., vol. 136, no. 2, p. 024706, Jan. 2012.

129. Y. Liu, G. Ji, M. A. Dastageer, L. Zhu, J. Wang, B. Zhang, X. Chang, and M. A. Gondal, Highly-active direct Z-scheme Si/TiO_2 photocatalyst for boosted CO_2 reduction into value-added methanol, *RSC Adv.*, vol. 4, no. 100, pp. 56961-56969, 2014.

130. E. Liu, L. Kang, F. Wu, T. Sun, X. Hu, Y. Yang, H. Liu, and J. Fan, Photocatalytic Reduction of CO_2 into Methanol over Ag/TiO_2 Nanocomposites Enhanced by Surface Plasmon Resonance, *Plasmonics,* vol. 9, no. 1, pp. 61-70, 2014.

131. C. Li, M. Y. Liu, N. G. Pschirer, M. Baumgarten, and K. Mllen, Polyphenylene-Based Materials for Organic Photovoltaics, *Chem. Rev.*, vol. 110, no. 11, pp. 6817-6855, 2010.

132. B. P. Rand, J. Genoe, P. Heremans, and J. Poortmans, Solar Cells Utilizing Small Molecular Weight Organic Semiconductors, *Prog. Photovolt Res. Appl.*, vol. 15, no. Version 45, pp. 659-676, 2007.

133. A M. Smith, S. Nie, "Semiconductor Nanocrystals: Structure, Properties, and Band Gap Engineering," *Acc. Chem. Res* vol. 43, no. 2 pp. 190-200, 2010

134. W. E. Buhro,, V. L.Colvin, "Semiconductor nanocrystals - Shape matters". *Nat. Mater.* vol. 2, 138139, 2003

135. M. Qamara, M.A. Gondala , Z.H. Yamania, b, " Removal of Rhodamine 6G induced by laser and catalyzed by Pt/WO_3 nanocomposite;" *Cat.Commun.*, Vol. 11, no. 8, Pp 768-772, 2010

136. B. D. Cullity and S. R. Stock, *Elements of X-ray diffraction*, 3rd Edition Prentice-Hall, New York (2001).

137. B. E. Warren, *X Ray Diffraction*, Dover Publications, New York, (1990).

138. R. Kelsall , Ian W. Hamley, M. Geoghegan, *Nanoscale Science and Technology*, John Wiley & Sons Ltd, Uk (2005).

139. McMullan, D. "Scanning electron microscopy". *Scanning* , vol. 17 no. 3, pp. 175-185, 2001

140. Smith KCA, Oatley, CW, "The scanning electron microscope and its fields of application". *British Journal of Applied Physics*, vol. 6, no. 11, pp. 391-399, 1955.

141. Brunauer, Stephen; Emmett, P. H.; Teller, Edward, "Adsorption of Gases in Multimolecular Layers". *Journal of the American Chemical Society*, vol. 60 no. 2, pp. 309-319, 1938

142. Rouquerol, J.; Llewellyn, P. L.; Rouquerol, F. "Is the BET equation applicable to microporous adsorbents?". Characterization of porous solids VII.

Studies in surface science and catalysis., vol. 4 no. 5 pp. 49-56, 2007

143. Plieth Walfried , *Electrochemistry for Materials Science*, Elsevier p. 420 (2008)

Vitae

PERSONAL DATA

Name: OLOORE LUQMAN EKUNDAYO

Date of Birth: July 1, 1985

Nationality: Nigerian

Permenant Address: Department of Physics and Engineering Physics,
Obafemi Awolowo University, Ile-Ife, Osun State, Nigeria

Postal Address: P.O Box 11194 Dugbe Ibadan, Nigeria

Email: *oloore02@gmail.com*

EDUCATION

2014 - 2016 Physics Department, King Fahd University of Petroleum and minerals,
Dhahran 31261, Saudi arabia

Master of Science(MSc) in Physics

Thesis: Synthesis of ordered mesoporous WO_3-based semiconductor nanocomposites with application in photoreduction of CO_2 to low carbon fuels

2005 - 2010 Department of Physics, Obafemi Awolowo University, Ile-Ife, Nigeria

Bachelor of Science (BSc) in Engineering Physics

Thesis: Calculation of energy eigenvalues of non-interracting spin-$\frac{1}{2}$ particle in three non-commuting external magnetic fields

PUBLICATIONS

PAPERS PUBLISHED IN ISI JOURNALS

3. A. O. Mehder, M. A. Gondal, M. A. Dastageer, Y. B. Habibullah, **L. E. Oloore**, M. A. Iqbal and Bilal Gondal, Direct spectral analysis and determination of high content of carcinogenic bromine in bread using UV pulsed laser induced breakdown spectroscopy, *J Environ Sci Health B*, 1-8 (2016)

2. M. A. Gondal, Y. B. Habibullah, Umair Baig, **L. E. Oloore**, Direct spectral analysis of tea samples using 266 nm UV pulsed Laser-Induced Breakdown Spectroscopy and cross-validation of LIBS results with ICP-MS. *Talanta* **152** 341-352 (2016)

1. M. A. Gondal, Y. B. Habibullah, **L. E. Oloore**, M. A. Iqbal, Determination of carcinogenic fluorine in cigarettes using pulsed UV laser induced breakdown spectroscopy, *Appl Opt.* **54**, 5560-5567 (2015).